Flexible Lipid Nanomaterials Studied by NMR Spectroscopy

Journal:	*Physical Chemistry Chemical Physics*
Manuscript ID	CP-PER-10-2018-006179.R1
Article Type:	Perspective
Date Submitted by the Author:	19-Feb-2019
Complete List of Authors:	Mallikarjunaiah, K.; Indian Institute of Science, Department of Physics Kinnun, Jacob; Indiana University Purdue University at Indianapolis, Department of Physics Petrache, Horia; Indiana University Purdue University at Indianapolis, Department of Physics Brown, Michael; University of Arizona, Department of Chemistry and Biochemistry; University of Arizona, Department of Physics

Cite this: DOI: 10.1039/c0xx00000x

www.rsc.org/xxxxxx

Perspective

Flexible Lipid Nanomaterials Studied by NMR Spectroscopy

K. J. Mallikarjunaiah,[a,b] Jacob J. Kinnun,[c] Horia I. Petrache,[c] and Michael F. Brown*[,a,d]

[a] *Department of Chemistry and Biochemistry, University of Arizona, Tucson, Arizona 85721, USA*

[b] *Department of Physics, Indian Institute of Science, Bangalore, India 560012*

[c] *Department of Physics, Indiana University Purdue University, Indianapolis, Indiana 46202, USA*

[d] *Department of Physics, University of Arizona, Tucson, Arizona 85721, USA*

* Corresponding author

Received (in XXX, XXX) Xth XXXXXXXXX 20XX, Accepted Xth XXXXXXXXX 20XX
DOI: 10.1039/b000000x

Abstract

Our review addresses how material properties emerge from atomistic-level interactions in the case of lipid membrane nanostructures. We summarize advances in solid-state nuclear magnetic resonance (NMR) spectroscopy in conjunction with alternative small-angle X-ray and neutron scattering methods for investigating lipid flexibility and dynamics. Solid-state ^{2}H NMR is advantageous in that it provides atomistically resolved information about the order parameters and mobility of phospholipids within liquid-crystalline membranes. Bilayer deformation in response to external perturbations occurs over a range of length scales and allows one to disentangle how the bulk material properties emerge from atomistic forces. Examples include structural parameters such as the area per lipid and volumetric thickness together with the moduli for elastic deformation. Membranes under osmotic stress allow one to distinguish collective undulations and quasi-elastic contributions from short-range non-collective effects. Our approach reveals how membrane elasticity involves length scales ranging from the bilayer dimensions on down to the size of the flexible lipid segments. Collective lipid interactions on the order of the bilayer thickness and less occur in the liquid-crystalline state. Emergence of lipid material properties is significant for models of lipid-protein forces acting on the mesoscopic length scale that play key roles in biomembrane functions.

Key words: area per lipid, cholesterol, ion channels, G-protein–coupled receptors, GPCRs, membrane remodeling, bilayer deformation. molecular dynamics, osmotic pressure, rafts, SANS, SAXS, solid-state NMR spectroscopy

1. Lipid Membranes as Functional Nanomaterials

Biomembranes encompass proteins, lipids, and carbohydrates, as well as cellular water, which collectively perform a formidable array of cellular functions. From a physical perspective, this synergy relies on special material properties of membranes that emerge at the nanoscale. The view of biomembranes as soft composite nanomaterials [1] is reinforced by modern-day experimental biophysical techniques [2-4] that go beyond static X-ray crystal structures of proteins and metabolites, giving new insights into pharmacology and chemical biology. In particular, X-ray and neutron scattering technologies as applied to lipid membranes have been insightfully summarized recently. [4, 5] Here we provide a complementary review based on solid-state nuclear magnetic resonance (NMR) spectroscopy, which together with scattering methods enables a comprehensive picture of membrane dynamics and function to be acquired. This gain in fundamental knowledge can boost applications not only to medicine and drug delivery, but also in the manufacturing of new nanomaterials.

The basic forces that preserve biological structure and control atomic motions in macromolecules are well known [6]. They include hydrogen bonding, electrostatic, and van der Waals interactions, together with the hydrophobic effect. The forces mentioned above are weak, because their associated energies are comparable to the thermal energy at ordinary temperatures. That is why most biological matter is "soft" near physiological temperature [1]. Strong forces like those exerted by covalent bonds are usually not broken when a protein changes conformation, or when a lipid phase transition happens. Understanding how the weak forces underlie the functional dynamics of biological macromolecules—and how the membrane properties emerge from the atomistic-level interactions—is currently the subject of intense interest by many researchers worldwide. Accordingly, our perspective is to develop insight into how the forces in molecular dynamics (MD) simulations lead to membrane structure as observed by spectroscopic and scattering methods. In a subsequent step, one can inquire how the spectroscopic and scattering observables are related to properties of the lipid membrane. These material properties are characterized by geometric (structural) parameters such as the average cross-sectional area per lipid and the bilayer thickness, along with the response to an external force, expressed by deformation moduli such as the bending rigidity and lateral compressibility [7]. More broadly, the curvature stress field of the membrane bilayer comes into play, as formulated by the monolayer spontaneous curvature and the associated moduli for bending and Gaussian curvature in terms of a language of shape [1].

Relatively Weak Interactions Underlie Characteristic Properties of Biomembranes.—Emergence of the material properties of lipid membranes is fundamental to quantitative biophysics, for example, in theoretical descriptions of protein-lipid interactions resting on a flexible surface model [8], or hydrophobic matching [9]. On the other hand, not all the relevant structural and material quantities are accessible from empirical measurements alone. Particularly significant is that accurate membrane structural parameters are needed for computer simulations of lipid bilayers [10] and biomembranes [11]. As reviewed here, experimental validation from NMR spectroscopy is provided by order parameter profiles for acyl chains due to the pressure field within the membrane. Additional knowledge is acquired from complementary methods such as X-ray or neutron scattering, which furnish density profiles of either electron or nuclear scattering lengths. For investigating lipid interactions, we aim to achieve detailed insights into the energy landscape, i.e., the multidimensional hypersurface that describes both the structure and dynamics of membranes. The journey from these observables to material parameters is far from effortless, but it has been mapped to a significant extent as reviewed here.

From a theoretical perspective, the following avenues are possible in studying lipid membranes quantitatively: the first involves either all-atom MD simulations [10, 12, 13] or coarse-grained models [14-17]. The other entails a continuum description, whereby atomistic information is relinquished in favor of a reduced number of material constants. The two approaches are highly synergistic, and together they allow us to investigate how atomistic or molecular-level forces underlie the emergence of collective properties over larger scales [18, 19]. Such a composite approach dovetails with theoretical efforts involving multi-scale simulations [20] by Marrink et al. [17], Voth et al. [16], and others. As introduced for liquid crystals, solid-state ^{2}H NMR order parameters [21] offer a practical link between the membrane force field and the mesoscopic or thermodynamic properties of lipid membranes. Important further information about the dynamics of the membrane lipids is acquired from NMR relaxation measurements [22]. By combining spectroscopic and thermodynamic approaches, we gain insight into how the lipid self-assembly leads to the emergence of membrane properties at the mesoscopic scale.

Such a material science view of biomembranes becomes especially instructive when considering what materials do: they deform in response to external forces, particularly when they are soft. Notably, solid-state ^{2}H NMR spectroscopy [23] uniquely informs the question of whether bilayers distort significantly or not under biologically relevant forces, e.g., osmotic or hydrostatic pressures. Here we focus on statistical mechanical approaches for calculating membrane structure and dynamics with spectroscopic methods [24, 25]. Using force-based procedures together with NMR technology, one can establish the response of the material at an atomistic level [26], as further described below. At the ultra-small length scale, lipid membranes are collections of atoms whose fluctuations can be traced in exquisite detail by molecular dynamics trajectories [27-30]. The significance is that MD simulations encapsulate the observables by the potentials and forces that allow molecular properties to be investigated when observational approaches are challenging [31-35]. The force fields used in dynamics trajectories integrate the data from diverse experimental techniques [36, 37]. Molecular simulations [32] contribute strongly to our current understanding of biological lipids, as shown by the pioneering work of Martin Karplus and Richard Pastor et al. [38], together with studies of lipid-protein interactions by Klaus Schulten [39] and others [16, 40, 41].

When considering the molecular interactions, first we recall that the membrane flexibility involves an unimaginable number of degrees of freedom. They span a wide range of length scales, from large domains on the order of hundreds of nanometers on down to the size of the lipid segments [42]. But at cellular length scales, lipid membranes are continuous hydrophobic barriers. Together with membrane proteins, they enable key functions such as cell signaling, energy transduction, and membrane trafficking to occur. Remarkably, these two length scales differ by 10^3–10^4 orders of magnitude. Somewhere in this huge range, material properties emerge from the proteolipid ensemble and the associated water molecules (Fig. 1). Here we show that solid-state ^{2}H NMR spectroscopy gives an unprecedented experimental access into this problem when measurements are performed at various hydration levels [26]. In our approach, we distinguish regimes where collective undulatory and quasi-elastic repulsive forces operate from those where short-range molecular protrusions can occur between the apposed bilayers. The general principle is that a continuum description of deformations is valid over nearly the entire range of relevant length scales. Particularly the emergence of quasi-elastic lipid interactions on the order of the bilayer thickness and less supports the applicability of a continuum flexible surface model (FSM) [43] to lipid-protein interactions [44]. **[FIGURE 1]**

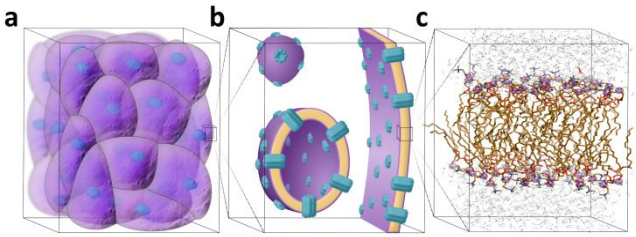

Figure 1. Hierarchy of relevant scales showing (a) biological cells at large scales, (b) lipid membranes with embedded proteins at the intermediate (meso)scale, and (c) lipid bilayer at the molecular and atomic scale. Colored spheres indicate the lipid polar head groups in contact with the aqueous medium and flexible brush-like strings depict the nonpolar chains within the bilayer core. The lipid bilayer provides a barrier to the movement of ions and polar molecules across the hydrophobic interior and serves as a fluid-like solvent for membrane proteins. **[95% of single-column width]**

Lipid Membranes are Soft Materials That are Deformed by External Forces— Our emphasis in this article is mainly on the planar, lamellar lipid phase, in which the structural properties are the bilayer thickness, molecular area at the lipid aqueous interface, and the corresponding moduli for bilayer deformation (Fig. 2). For analogous discussions of lipid polymorphism and curvature see Refs. [1, 44, 45]. Membrane Lipid-protein interactions are due to the so-called hydrophobic matching (involving bilayer thickness, area per lipid, and compressibility), as well as curvature matching (spontaneous curvature and bending rigidity) to the proteolipid interface. Conventional thinking often centers on the role of proteins, and completely neglects the lipids, carbohydrates, and associated water, which comprise the so-called soft membrane matter. But experiments yield clear evidence for significant and necessary contributions of bilayer deformation to membrane function [1, 8, 46, 47]. Such deformations are measurable upon dehydration under osmotic stress, and reveal the strength of the forces responsible for membrane structure and assembly. They include van der Waals attractions [48], as well as repulsive membrane undulations [49], hydration forces [50, 51], and protrusions of the lipid molecules [52, 53]. These interactions are pertinent to understanding general features of membrane properties, such as mechanosensitivity [54, 55], as well as activation of G-protein-coupled receptors (GPCRs) and ion channels [1, 46, 56]. Membrane

proteins carry out their functions within the stress field of the lipid bilayer, wherein conformational changes are necessarily connected with the work of bilayer deformation [8, 57]. These aspects are relevant to lipid-protein interactions and cellular membrane remodeling as discussed below. [1, 8, 58, 59] **[FIGURE 2]**

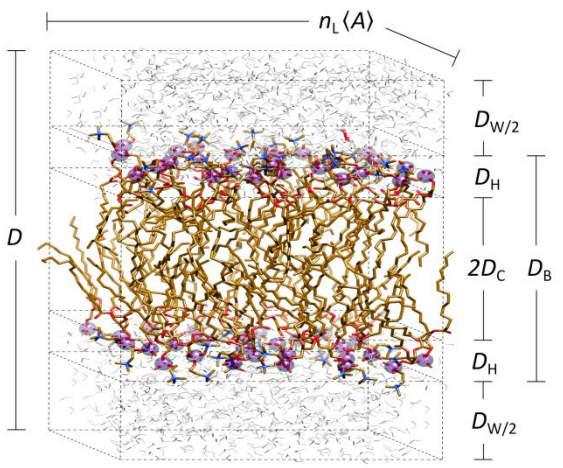

Figure 2. Solid-state ^{2}H NMR spectroscopy and small-angle X-ray scattering (SAXS) reveal structural measures of the lipid bilayer. The lamellar structure of the phospholipid membrane is shown with the pertinent structural quantities. The lamellar repeat spacing $D = D_W + D_B$ is the sum of the interlamellar water distance $D_W = 2D_{W/2}$ and the bilayer thickness $D_B = 2(D_H + D_C)$, where D_C is the hydrocarbon thickness per bilayer leaflet, and D_H is the head group thickness. For liquid-crystalline bilayers, the average cross-sectional area per lipid $\langle A\rangle$ together with the number of lipids (N_L) gives the membrane surface area. Measuring how these structural quantities change under external stress provides an experimental view of molecular forces within lipid membranes. **[90% of single-column width]**

2. Lipid Bilayers—More than Barriers?

Our understanding of lipid properties has been developed over the years through application of various measurement techniques, together with theoretical models [60-63]. Current research is generally focused on the types, rates, and amplitudes of the lipid motions [22, 64-66], as well as the energetics of the underlying phase transitions and polymorphic behavior [67]. Non-lamellar phases in which membrane curvature is visibly manifested are also of interest, due to the role of curvature forces in lipid-protein interactions [1], as well as crystallization of membrane proteins [68-70]. Research shows that proteins embedded in or spanning the membrane bilayer (integral membrane proteins) are significantly impacted by properties of the lipid matrix [8, 26, 43, 59, 71, 72]. Chemically non-specific material properties of the lipids in their crowded environments with membrane proteins can govern the cellular functions [26, 43]. Furthermore, the effects of specific lipid interactions due to hydrogen bonding, electrostatics, or van der Waals interactions can come into play [73].

As a result, we are led to address the following questions: (1) Solid-state NMR and molecular spectroscopy in general are based on quantum mechanics, and thus are inherently atomistic. How can we understand the length scale over which the atomic-level interactions captured in the MD force fields lead to the continuum material properties of the lipid nanostructures? (2) What is the relation of the atomistic observables from NMR and molecular spectroscopy to the collective properties of lipid nanomaterials? (3) Is the lipid membrane just an inert barrier and solvent of membrane proteins, or does it actively participate in cellular functions? (4) Which approach is most informative to explaining cellular function—an atomistic view or a continuum picture? These topics are addressed in membrane biophysics by experimental and theoretical research involving NMR spectroscopy within the broader context of liquid crystals and surface chemistry and physics.

2.1 Multiscale Structural Fluctuations in Fluid Lipid Membranes

Traditionally lipid bilayer structure and membrane interactions have been investigated by diffraction techniques, such as small-angle X-ray [60] and neutron [74, 75] scattering as applied to freely suspended samples. But scattering data from fluid lipid membranes are limited to a small number of diffraction orders, representing correlations at large distances [76], unless heroic methods (hydration chambers) are used to prepare and stabilize oriented lipid multilayers. Additional methods that operate at large length scales entail optical microscopy of fluorescently labeled membrane components [77, 78]. These and related techniques are often used to provide information about domain formation in large unilamellar vesicles [79-81] or substrate-supported lipid membranes [82, 83].

Membrane Lipids are Studied by Integrating Spectroscopy With Scattering Techniques —To expand the range of accessible length scales [19], in lipid biophysics the spectroscopic and scattering techniques can be further integrated. Measurements as

a function of hydration and temperature can identify regimes of membrane deformation spanning 2D undulatory motions and quasi-elastic 3D fluctuations involving short-range perturbations. Solid-state ^{2}H NMR spectroscopy is especially informative, as it gives information on orientational order at an atomistic level that is complementary to the positional order afforded by X-ray and neutron scattering methods. Because solid-state ^{2}H NMR yields knowledge of both average structure and dynamics, it can fill the gap between molecular structures and the stress fields of lipid nanostructures. Generally, the length scale at which material properties such as viscoelasticity or mechanosensitivity emerge from molecular interactions falls intermediate between the atomic and macroscopic—hence it is called mesoscopic. As biological membranes include not just proteins but also the lipids, water, and carbohydrates, the snapshots from protein X-ray crystallography are insufficient for a full description. In fact, membrane proteins carry out their functions within the stress field of the lipid membranes, which are soft, liquid-crystalline assemblies with surface shaping properties [43, 84-86]. Compared to the isotropic media of soluble proteins, the bilayer pressures are highly anisotropic, which affects the energetics of conformational states of proteins within membranes, e.g., as in the case of ion channels, GPCRs, and membrane transporters [8, 43]. But how do we go about describing membrane systems at the mesoscopic level? Here we show that such a description is possible based on experimental observables from solid-state NMR spectroscopy, in which well-established concepts from surface chemistry and physics are introduced for lipid membranes.

2.2 Membranes as Liquid Crystals

From a material science perspective, lipid bilayers are liquid crystals—they are ultrathin elastic materials [87, 88] that undergo significant deformation in response to external forces. Lipid membranes share many features in common with other liquid crystals [89, 90], and their study by NMR gives quantitative measures of the physical properties [91, 92]. Especially solid-state ^{2}H NMR spectroscopy along with X-ray and neutron scattering techniques are at the forefront of membrane lipid biophysics [93]. Combining these methods overcomes the ambiguities associated with X-ray scattering methodologies used to evaluate membrane deformation [94, 95]. Physical properties, such as the effective acyl chain length and the average chain cross-sectional areas of phospholipids in the liquid-crystalline (L_α) phase are investigated using simple statistical models [24] as further discussed below.

One of our aims in this review is to explain for the general reader how statistical mechanics can be applied to calculate membrane structural properties from spectroscopic data. We highlight the utility of solid-state ^{2}H NMR spectroscopy as an measurement tool that can be integrated with X-ray [76] and neutron scattering [96, 97] and other spectroscopic techniques for studying membrane deformations and molecular fluctuations [26, 37, 98, 99]. A comprehensive view of membrane forces includes how external variables such as osmotic [26, 100] and hydrostatic [101] pressures cause structural and dynamical remodeling of the bilayer matrix [8]. With the availability of information about membrane dynamics from both experiments [22, 102] and simulations [28, 29, 103], the molecular picture can be useful as a counterpart to representing lipid bilayers in terms of a stress field [104]. On the other hand, membrane organization and lipid-protein interactions are significantly affected due to the bilayer deformation and membrane shape fluctuations, which in turn can affect key cellular functions [8, 105].

Lipid Interactions with Water Underlie Their Liquid-Crystalline Behavior. Our approach takes advantage of existing knowledge of the physics of smectic and nematic liquid crystals, in which thermodynamic properties are related to internal stresses generated by anisotropic interactions [106-113]. In Fig. 3, we show some examples of phospholipids and cholesterol that are representative of biomembrane constituents having both structural and functional roles. Upon hydration, phospholipids form multilamellar structures, with a repeat unit cell that corresponds to the lipid volumes on either side of the bilayer midplane, plus the associated water [60, 114]. In liquid-crystalline membranes, the lipid head groups (phosphate groups are shown in Fig. 2 as a filled spheres) are localized at the water interface in a region of thickness D_H on either side of the membrane. When the unit cell is centered at the bilayer midplane, see Fig. 2, there are two water regions with thicknesses denoted by $D_{W/2}$ and a hydrocarbon region of thickness D_C occupied by the acyl chains. Additional structural parameters are the bilayer thickness D_B and $\langle A \rangle$, the cross-sectional area per lipid. By osmotically stressing the membrane, one can suppress the collective lipid motions ranging from long wavelength undulations [106] to mesoscopic collective motions [18, 115], and ultimately to short-range protrusion forces as discussed by Håkan Wennerström and Jacob Israelachvili [116]. The details of how these structural and dynamical parameters are defined and calculated will be given below. **[FIGURE 3]**

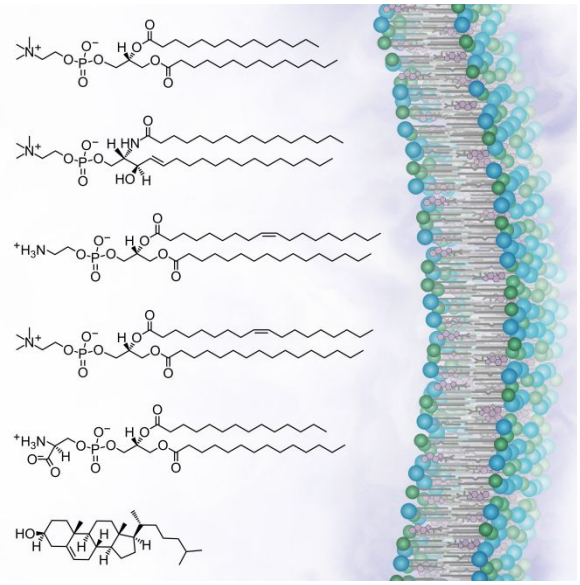

Figure 3. Biomembranes are composed of lipids, cholesterol, and proteins in a hydrated cellular environment. Examples of glycerophospholipids are shown for zwitterionic phosphocholine (PC) and phosphoethanolamine (PE) head groups, and for the anionic phosphoserine (PS) head group. Sphingomyelin (SM) is representative of a sphingophospholipid with a phosphocholine head group and an N-acylated sphingosine backbone (ceramide). The polar head groups vary in size, hydrogen bonding, and charge. Nonpolar acyl chains differ in length and degree of unsaturation, as illustrated by myristic acid (14:0), palmitic acid (16:0), and oleic acid (18:1ω-9) groups. Cholesterol exemplifies the large class of steroid compounds. Representative lipid chemical structures from top to bottom are indicated: 1,2-dimyristoyl-*sn*-glycero-3-phosphoethanoamine (DMPC); N-palmitoyl-D-sphingosine-1-phosphocholine or N-palmitoyl-sphingomyelin (PSM); 1-palmitoyl-2-oleoyl-*sn*-glycero-3-phosphoethanolamine (POPE); 1-palmitoyl-2-oleoyl-*sn*-glycero-3-phosphocholine (POPC); 1,2-dimyristoyl-*sn*-glycero-3-phosphoserine (DMPS); and cholesterol. **[85% of single-column width]**

3. Biomembranes in Surface Chemistry and Physics

The approach and results highlighted in this perspective are multifold: they investigate membrane deformation, discern forces that affect protein-related activities of cellular membranes, and foster the development of atomistic MD simulations. Our aim is to explain the use of solid-state ^{2}H NMR spectroscopy for investigating structural distortions of lipid bilayers induced by external forces. Fundamental concepts of membrane organization and function come from integrating knowledge from statistical physics and thermodynamics with observables from ^{2}H NMR spectroscopy [23] and alternative scattering techniques [3]. Experimentally, membrane lipids are studied in vitro as freely suspended bilayers, as supported samples on solid substrates (planar, cylindrical, or spherical geometry), or as unilamellar vesicles. The applications described herein tend to involve unsupported membrane bilayers in the liquid-crystalline (liquid-disordered, ld) state above the order-disorder phase transition temperature [23, 67]. Measurements of the structural deformations of membranes under various conditions of osmotic stress have been the focus of X-ray diffraction studies since the early work of Luzzati et al [117], and subsequently Rand [118] and Parsegian [119]. Because solid-state ^{2}H NMR spectroscopy has only rarely been used for osmotic stress studies [100], one of the goals of our review is to highlight the usefulness of the method. In this context, ^{2}H NMR also plays a very important role in validation of molecular simulations.

3.1. Deuterium NMR Spectroscopy and Membrane Structure

As a unique and robust experimental tool, solid-state NMR is widely used to study molecular structures, phase transitions [120], and dynamics [26, 102, 121, 122] of matter in its various states. Examples include crystalline, non-crystalline, or amorphous materials like superionic compounds [123-125], glasses [126], ceramics [127], polymers, lipid membranes [128], DNA fibers [129, 130], amyloid fibrils, and membrane proteins [102, 131]. In solid-state NMR spectroscopy, angular fluctuations are detected, which are related to positional order through the orientational distribution functions. Coming now to membranes, the lipids are often studied as freely suspended multilamellar dispersions in water, or alternatively, aligned on solid supports with planer, cylindrical, or spherical geometry. Knowing how the spectral couplings depend on the orientation of the lipid nanostructure with respect to the laboratory axes system enables analogous information to be acquired from freely suspended bilayers and aligned samples. The mobility of lipids and their physical interactions with other membrane constituents, as well as proteins and nucleic acids [64] having important roles in biology, are accessible by solid-state NMR methods at the atomistic level.

Structural and Material Properties of Lipids are Investigated With Solid-State NMR Spectroscopy—Compared to alternative diffraction methods, NMR detects both lipid membrane structure and mobility [23, 132]. It manifests solid-like and liquid-like features of the molecules. Solid state NMR has the advantage that the

anisotropic magnetic or electric couplings (dipolar, quadrupolar, chemical shift) yield segmental order parameters as model-free experimental observables. The disadvantage is that the broad spectral width requires special high-power NMR technology, and rather large amounts of sample material are needed. Motional averaging of the couplings (dipolar, quadrupolar, chemical shift) occurs on a characteristic timescale (given by the inverse anisotropy of the angular-dependent couplings, which for ^{2}H NMR is ~10^{-5} sec). However, the anisotropic electric or magnetic couplings are not completely averaged to zero, e.g., in the case of residual dipolar couplings (RDCs) or residual quadrupolar couplings (RQCs) [23]. As a result solid state NMR determines bond distances and angles as well as electronic structure and dynamics. By contrast, in solution NMR the anisotropic interactions are averaged over all space, leaving the scalar (indirect or through bond) dipolar couplings and chemical shifts that inform bonding connectivity and electronic structure in molecules. Distances are obtained through relaxation and nuclear Overhauser (NOE) measurements, and the dynamics include conformational exchange as discussed in standard texts [133].

The reader should note the term "solid-state NMR" does not mean the sample is a rigid solid —it refers to the non-zero averaged electric or magnetic couplings (dipolar, quadrupolar chemical shift). It only means that the sample is not an isotropic liquid, where complete isotropic averaging occurs. For an immobile solid, the rigid-lattice or static NMR spectrum is measured, with essentially no averaging of the electric or magnetic couplings, as in single crystals or polycrystalline samples. With a single crystal, the second-rank tensorial couplings afford information about bond distance and angles, as well as electronic structure [23]. And for a polycrystalline solids, knowing how the angular interactions transform with respect to the crystal and the laboratory frames allows equivalent information to be obtained. As an example, in solid-state ^{2}H NMR spectroscopy, deuterium (^{2}H) is substituted for hydrogen (^{1}H), and it is mainly orientational order that is measured. To obtain position-dependent molecular structure requires the introduction of structural models [24]. Alternative magic-angle spinning (MAS) ^{13}C NMR methods allow the ^{13}C–^{1}H distances to be obtained directly [22, 134, 135]. For a given lipid sample geometry, similar information is obtained for nonaligned specimens and when aligned on supports in analogy to molecular solids.

When applied to membrane lipids, solid-state ^{2}H NMR reveals information about both the orientational order, i.e., the amplitude of the segmental or molecular motions as well as their rates. The advantage of studying freely suspended, random multilamellar lipid dispersions is that angular-dependent spectral couplings are readily obtained. By introducing spectral deconvolution methods (so-called de-Pakeing) [23], we obtain the oriented subspectrum of an aligned sample, e.g., as in the case of a planar, cylindrical, or spherical supports. Accordingly in random or aligned lipid multilamellar dispersions, those motions faster than the inverse of the coupling anisotropy give an average (residual) coupling. The segmental order parameters are obtained by comparison to the static value. Additional slower motions give an inhomogeneously broadened lineshape from various orientations of the bilayer with respect to the laboratory axes defined by the external magnetic field [23]. For small unilamellar vesicles, their overall reorientation completes the averaging of the anisotropic couplings [18] leaving the scalar couplings and isotropic chemical shifts. Residual couplings or order parameters are not directly measured as with solid-state ^{2}H NMR spectroscopy; and hence only the chemical shifts, scalar couplings, and relaxation parameters are observed.

Deuterium NMR Order Parameters are Used for Calculating Biomolecular Structure and Dynamics—In solid-state ^{2}H NMR spectroscopy, evaluation of the membrane structural parameters—such as the bilayer thickness and area per lipid—rests upon the analysis of segmental order parameters (S_{CD}), which are obtained from the residual quadrupolar couplings (RQCs) of the lipids. Relatively simple statistical models are used to calculate the average area per lipid $\langle A \rangle$ and related structural quantities that are applicable to bilayer remodeling and molecular dynamics simulations. Our approach has the advantage that the ^{2}H NMR observables are directly connected to the stress field of the lipid bilayers. Besides structural studies, ^{2}H NMR spectroscopy is used to probe orientational fluctuations of the lipid molecules, which is highly complementary to X-ray and neutron scattering [96]. For example, in X-ray scattering, logarithmically varying positional correlations generate scattering peaks with long tails due to collective membrane fluctuations (e.g., undulations) [136]. Use of NMR spectroscopy thus affords a powerful means of investigating the structural and material properties of membrane lipids and biomembranes.

3.2. Solid-State NMR and Scattering Techniques for Studies of Membrane Liquid Crystals

As mentioned above, lipid membranes are often studied as freely suspended multilamellar dispersions in aqueous solutions, as supported membrane bilayers on planar [137] or spherical supports [138], within aluminum oxide nanotubes [139, 140], tethered or aspirated into micropipettes [7, 141], or as small unilamellar vesicles [115]. With solid-state NMR spectroscopy, multilamellar dispersions of the lipid membranes are investigated, or alternatively, bilayers are aligned on planar substrates [142, 143]. Likewise studies of lipid membranes on spherical supports [144] as well as bilayers contained within cylindrical nanotubes [139] are useful for various applications. Most experiments are conducted in the liquid-crystalline state (ld, liquid-disordered) above the order-disorder phase transition, with further research involving the low temperature gel phase (solid-ordered, so) [145-147] and cholesterol-containing phases (liquid-ordered, ld) [148, 149]. Here we are interested in extracting quantitative structural information from solid-state NMR measurements of unsupported multilamellar dispersions of phospholipids in the liquid-crystalline state, e.g., by focusing on the area per lipid at the aqueous interface. Additionally, we aim to integrate the results with small-angle X-ray scattering (SAXS) studies and MD simulations to achieve new insights. In the case of scattering methods (SAXS and SANS), lipid membranes are investigated as multilamellar dispersions or aligned on planar substrates, thus enabling comparisons with solid-state NMR spectroscopy.

Liquid-Crystalline Bilayers have a Well-Defined Unit Cell—The snapshot in Fig. 2 represents a portion of a membrane lipid bilayer in which the water molecules surround and partially penetrate the membrane from the lipid head groups to the level of the glycerol backbone [150, 151]. The unit cell comprises two of the opposed lipid molecules plus one-half the water layer thickness on either side of the bilayer. This unit cell view of the lipid membrane is useful for evaluating the structural information from ^{2}H NMR spectroscopy. Structurally, the unit cell dimension D is written as a sum of the average bilayer thickness, D_B and the average thickness D_W of the water region [152]. The bilayer thickness is further subdivided into the head group (D_H) and hydrocarbon (D_C) contributions,

$$D = D_\mathrm{B} + D_\mathrm{W} = 2(D_\mathrm{C} + D_\mathrm{H}) + D_\mathrm{W} \qquad (1)$$

The cross-sectional area per lipid $\langle A \rangle$ is related through the total volume V of the lipid unit cell, as given by

$$\langle A \rangle = V / D \qquad (2)$$

It is decomposed into lipid and water contributions as $V = 2V_\mathrm{L} + 2 N_\mathrm{W} V_\mathrm{W}$, where N_W denotes the number of water molecules per lipid. Practically, the decomposition serves to define the volume per lipid molecule [60] as

$$V_\mathrm{L} = \frac{V}{2} - N_\mathrm{W} V_\mathrm{W}, \qquad (3)$$

where V_W denotes the volume of a water molecule as measured in the bulk. This separation is fully consistent with measurements of lipid volumes by buoyancy methods [153], and avoids the ambiguities for volumetric assignments at the lipid-water interface [154]. Both the SAXS and NMR analyses of structural parameters consider the decomposition $V_\mathrm{L} = V_\mathrm{H} + 2V_\mathrm{C}$, where V_C and V_H are the volumes of one of the hydrocarbon chains (assumed identical for chain-symmetric lipids) and the lipid head group, respectively (see Fig. 2). Hence, we are left with the hydrocarbon thickness D_C, which is related to the hydrocarbon chain volume V_C through:

$$D_\mathrm{C} = 2\, V_\mathrm{C} / \langle A \rangle \qquad (4)$$

Although the hydrocarbon region of lipid bilayers can deform, its volume remains practically constant, except under extreme external pressures [24].

Solid-State NMR Spectroscopy and Diffraction Methods are Complementary Biophysical Technologies—To provide an illustration, the solid-state ^{2}H NMR spectrum and SAXS electron density profile are compared in Fig. 4 for a representative lipid membrane in the liquid-crystalline (liquid-disordered, ld) state [155]. The major distinction is that the ^{2}H NMR spectrum in Fig. 4(a) reports on the individual sites of deuteration along the lipid acyl chain, while the electron density profile in Fig. 4(b) entails lower spatial resolution. It is important to recognize that solid-state NMR methods such as ^{2}H NMR [23] or ^{13}C separated local field NMR methods [134, 156] inform the *orientational* order of the individual segments, whereas SAXS and SANS measure the *positional* order at lower resolution, corresponding to dimensions on the order of the bilayer thickness or the interlamellar spacing. Solid-state ^{2}H NMR gives us the orientational order parameters of the flexible lipid segments as model-free experimental observables [18, 26]. Studies using solid-state NMR spectroscopy and X-ray scattering have uncovered significant deformation of lipid membranes due to interbilayer forces associated with changes in hydration. **[FIGURE 4]**

In the solid-state ^{2}H NMR spectrum of the fully hydrated dispersion of 1,2-diperdeuteriomyristoyl-*sn*-glycero-3-phosphocholine (with perdeuterated acyl groups) in Fig. 4(a), the

number of carbons in the acyl chain is n_C = 14 where i = 2–13 corresponds to the various methylene segments, and i = 14 designates the terminal methyl group. For the DMPC-d_{54} bilayer, we can calculate the residual quadrupolar couplings (RQCs) for the various carbon-deuterium segments along the acyl chain [157] directly from the experimental spectrum. The RQCs (hence order parameters) are connected with the average bilayer structure in terms of the amplitude of the orientational fluctuations of the lipid segments (details are provided in the next section). Estimates of physical properties such as the effective acyl chain length and average chain cross-sectional areas of phospholipids in the liquid-crystalline (L_α) phase can then be made in terms of simple statistical models [24]. **[FIGURE 4]**

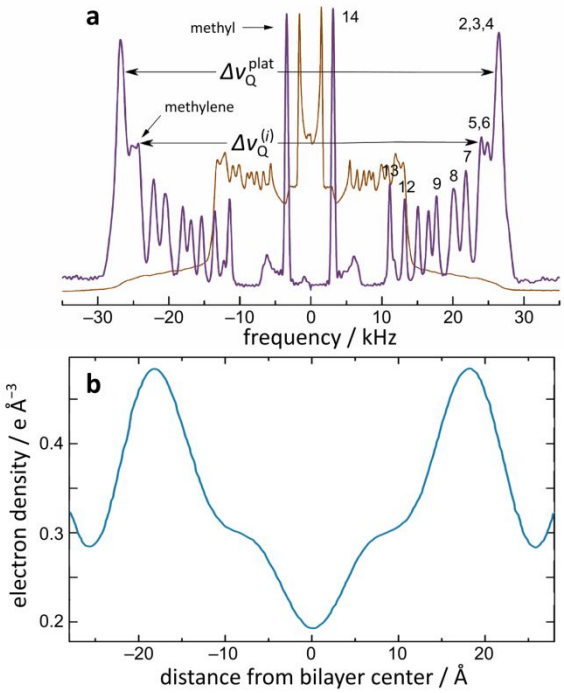

Figure 4. Structures of lipid bilayers in the liquid-crystalline state (liquid-disordered, ld) are investigated by solid-state ^{2}H NMR spectroscopy and small-angle X-ray scattering (SAXS). (a) Representative solid-state ^{2}H NMR spectrum for multilamellar fully hydrated DMPC-d_{54} (with perdeuterated acyl groups) in the liquid-crystalline state (30 ºC) recorded at 46.07 MHz (7.01 T). The thin line represents the powder-type spectrum, and the thick line is the deconvoluted (de-Paked) spectrum due to the parallel (θ = 0) orientation of the bilayer normal to the $\mathbf{B}_0$ magnetic field. Spectral peaks correspond to various acyl chain segments as indicated by superscripts i = 2…14 (cf. text). Residual quadrupolar couplings are designated by $\Delta\nu_Q^{(i)}$ and yield absolute order parameters $|S_{CD}^{(i)}|$ for the C–^{2}H bonds of the acyl chain segments. (b) Electron density profile (absolute units of e/A^3) for fully hydrated DMPC lipid bilayer obtained at 30 ºC from small-angle X-ray scattering (SAXS) studies [158]. The two peaks correspond to the electron-rich phosphodiester head groups and the dip in the bilayer center is due to the methyl groups. The distance between the two maxima (head group-to-head group spacing) is denoted by D_{HH}. **[85% of single-column width]**

The results of solid-state NMR spectroscopy in Fig. 4 versus alternative structural methods such as X-ray or neutron small-angle scattering [5, 159] illustrate some of the pros and cons of the different biophysical methods. For the comparative example of bilayer electron density in Fig. 4(b), the SAXS data are limited to a small number of diffraction orders, because of fluctuations in the fully hydrated fluid phase bilayers. Molecular disorder gives ensemble electron density profiles with broad features, where the prominent peaks arise from the electron-rich phosphate groups, and enable the head group-to-head group distance (D_{HH}) to be ascertained. The smaller electron density between the head group peaks characterizes the hydrocarbon core of the bilayers, wherein the dip in the center is due to the low electron density of the terminal methyl groups of the fatty acyl chains. The electron density profile characterizes the bilayer structure, and gives us a direct measure of its thickness in terms of the D_{HH} distance corresponding to the head–head separation. Small-angle X-ray scattering only establishes the locations of the phosphate groups; so to obtain the z-coordinates of the other segments, neutron diffraction studies of selectively deuterated lipids or heavy water are needed [2, 160]. But the transverse description of the bilayer organization is still lacking in terms of the area per lipid $\langle A \rangle$. One approach to obtaining the value of $\langle A \rangle$ involves a gravimetric X-ray method, often referred to as the Luzzati method [161]. Knowing the lipid molecular volume from dilatometry measurements [162] together with the lamellar repeat spacing (D) (Fig. 2) and the gravimetric number of water molecules per lipid, enables the average area per lipid at the aqueous interface to be determined. We shall return to this point later.

3.3. Combination of Deuterium NMR Spectroscopy with Small-Angle X-Ray Scattering

Small-angle X-ray and neutron scattering methods are often considered as the gold standard for obtaining structural information on membrane nanostructures [2, 3]. For lipid bilayers, scattering technologies are typically used for multilamellar lipid systems that produce sharp scattering peaks [136]. In small-angle X-ray scattering (SAXS) measurements, the interlamellar repeat

spacing D can be measured from the Bragg scattering peak intensity as a function of incident angle. If sufficient diffraction orders are available, then the electron density profile can be constructed (Fig. 4). Although electron density profile calculations are limited by Fourier truncation, one can estimate the various thicknesses as defined above (Fig. 2). The average area per lipid can then be calculated from the volume per lipid molecule using the Luzzati method. Extensive studies of lipid bilayers [72, 76, 163-167] have utilized the average area per lipid molecule $\langle A \rangle$ at the bilayer surface with water as a key structural parameter, to which the thickness is related by volumetric considerations [24, 168]. Still, it is experimentally quite challenging to measure the area per lipid. Often one has to rely on the length of the unit cell (designated as the interbilayer distance *D*) and its decomposition into water, lipid head group, and acyl chain regions (Fig. 2).

Positional and Orientational Order Characterize Membrane Structural Properties—Alternatively, the order parameters measured in solid-state ^{2}H NMR spectroscopy give complementary structural information on the distribution of the lipid segment orientations with respect to the bilayer normal [24, 26]. Solid-state ^{2}H NMR provides knowledge of bond orientations and their fluctuations at a site-resolved atomistic level [18], while scattering techniques give distances and positional fluctuations [166]. Precepts of statistical mechanics supply a link between the ^{2}H NMR and X-ray observables in terms of the corresponding partition functions, i.e., due to the orientation for NMR or position in the case of scattering methods [25, 101, 169]. These distributions can then be used to calculate structural parameters for investigating membrane properties. In effect, we deal with 1D quasi-crystalline order along the bilayer normal (*z*-direction), because the membrane lipids are in a disordered 2D liquid state in the transverse plane (*x*-*y* direction). Establishing the 1D order is relatively straightforward. Yet establishing the 2D distribution—and in particular the mean area per lipid $\langle A \rangle$ in the transverse direction—is less so [24, 159]. Such an approach allows one to quantify the bilayer deformations due to applied external forces, or from the presence of integral proteins, peptides, or cholesterol.

Though ^{2}H NMR does not measure positional correlations, structural parameters for anisotropic mesophases such as lipid bilayers can be calculated from the experimental orientational order parameters of C–^{2}H bonds of the deuterium-labeled acyl chains. These order parameters are denoted by $S_{\mathrm{CD}}^{(i)}$ where the superscript i labels the methylene chain segments from the carbonyl groups to methyl group ends. Membrane structural parameters are calculated by considering the acyl chain travel (projection) along the bilayer normal [24, 170]. Accordingly, the chain travel (or flux) is described statistically by a distribution function $p(D_i)$ of segmental projections D_i along the bilayer normal [24]. This orientational distribution corresponds to an alignment field (mean torque) experienced by the carbon segments. The first-order mean-torque model is described in detail below. Estimates of physical properties, like the effective acyl chain length and average chain cross-sectional areas of phospholipids in the liquid-crystalline (L_α) phase, can then be made using simple statistical models [24].

On the other hand, the application of solid-state NMR spectroscopy to obtain bilayer structural properties [157] is challenging, because the measured order parameters represent the second moment of the orientational distribution. But it is the first moment that is needed for calculating the average acyl chain length and the area per lipid. Consequently, we must assume a functional form for the distribution function, and use the measured moments to characterize the potential, or equivalently the orientational probability. Furthermore, the orientational potential is expected to have odd parity (due to the lipids within a monolayer), whereas the spectroscopic observables have even parity [142]. Various approaches to this problem have considered either a continuum mean-torque potential or a discrete diamond-lattice angular distribution. In either case, the measured S_{CD} order parameters are used to calculate the average projected chain length along the normal to the bilayer surface as the sum of the average acyl segmental projections [171]. Complications due to back-folding of the acyl groups are avoided by using the part of the chain closest to the aqueous interface to obtain the area per lipid [24].

3.4. Configurational Statistics of Acyl Chains in Membrane Liquid Crystals

It may be helpful to the reader at this point to consider two complementary approaches to evaluating chain conformations, as discussed by Petrache et al. [24]. The first is a discrete rotational isomeric (diamond-lattice) model, and the second is a continuous mean-torque model. Because the lipid membranes are highly dynamic, with many internal degrees of freedom, using spectroscopic or scattering methods we measure time- or ensemble-averaged quantities. Figure 5 shows that for the case of liquid-crystalline lipid bilayers, the projections of the carbon-

deuterium bond segments along the bilayer normal allow us to quantify the chain travel (flux) away from the water-lipid interface, i.e., towards the center of the bilayer. Both the lipid head groups and the fluctuations of the acyl chains affect the mean cross-sectional area per lipid. The angular deviations of the methylene segments from the bilayer normal, defined as $\beta_{PD}^{(i)}(t)$ in Fig. 5, are necessarily related to the area per lipid. Take note that the hydrocarbon thickness D_C is not the same as the average acyl chain length, when using segmental projections for calculations of volumetric parameters [24] (see below). **[FIGURE 5]**

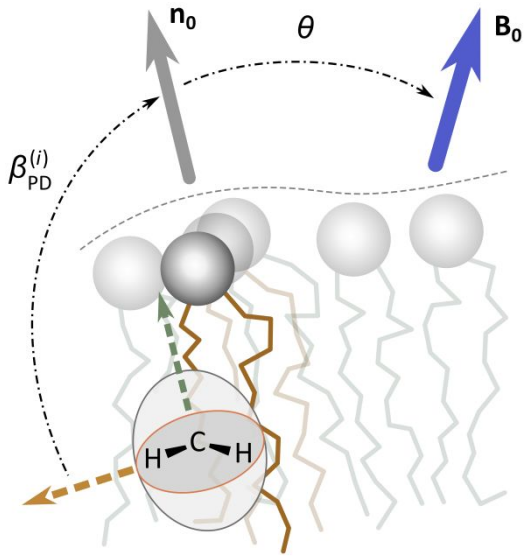

Figure 5. Solid-state ^{2}H NMR spectroscopy measures the angular fluctuations of carbon–deuterium bonds in terms of orientational order parameters. Lipid polar head groups are shown by open spheres and irregular lines depict the nonpolar chains, Segmental order parameters are formulated as a time-ensemble average of the C–^{2}H orientations with respect to the bilayer normal ($\mathbf{n}_0$) and the direction of the magnetic field ($\mathbf{B}_0$). The $S_{CD}^{(i)}$ order parameter of each bond corresponds to the Legendre function $(1/2)\langle 3\cos^2\beta_{PD}^{(i)} - 1\rangle$ where the time-dependent angle $\beta_{PD}^{(i)}(t)$ is between the *i*th carbon-deuterium bond and the bilayer normal. For a given three-carbon segment of a polyethylene chain, the internal frame (I) is perpendicular to the H–C–H plane and the angle to the long molecular axis is $\equiv \beta_{IM}$ (not shown). The observables (S_{CD}) from solid-state ^{2}H NMR spectroscopy are related to the average bilayer structural properties. **[80% of single-column width]**

To relate the lipid area to the configurational statistics of the acyl chains, we need to assume a distribution function, as introduced below. For a given acyl segment (index *i*), as first shown by Jansson et al. [172] the appropriate average is $\langle A\rangle \propto \langle 1/D_i\rangle$, where D_i is the instantaneous travel (projection) along the bilayer normal (called the director) of a statistical segment having D_M as its length. (Angular brackets indicate a time or ensemble average, in accord with the ergodic principle.) From the C–^{2}H bond order parameters (S_{CD}), together with the chain volume V_C we can calculate the average value $\langle 1/D_i\rangle$ by employing appropriate statistical models. For instance, a mean-torque model [24] can be employed, as explained in the next section. Figure 5 teaches us how the experimental solid-state ^{2}H NMR order parameters $S_{CD}^{(i)}$ are related to the bilayer structure and dynamics averaged over the various degrees of freedom. The segmental order parameters measure the orientational fluctuations of the C–^{2}H bonds, i.e., about the average orientation to the bilayer normal. The statistical amplitude is described by the time-averaged second-order Legendre polynomial, $P_2(\cos\beta)$, where β is the angle between different axis of rotations, and is separated into the time-dependent $\beta_{PD}^{(i)}(t)$ part, and β_{DL}, the time-independent part. Here $\beta_{PD}^{(i)}(t)$ is the angle between the *i*th carbon-deuterium bond (principal axis, P) and the bilayer normal (director axis, D), and $\beta_{DL} \equiv \theta$ is the angle between the bilayer normal and direction of the external magnetic field $\mathbf{B}_0$ (the laboratory axis, L) (Fig. 5). Motions with respect to bilayer normal occur on the NMR time scale, while changes at larger scales are typically much slower.

Segmental Order Parameters are Derived From Residual Quadrupolar Couplings—Because the quadrupolar coupling depends on the C–^{2}H bond orientation with respect to the magnetic field axis, in solid-state ^{2}H NMR spectroscopy we measure a frequency splitting $\Delta\nu_Q^{(i)}$ that is proportional to the $S_{CD}^{(i)}$ orientational order parameter [132]. The mathematical relationship is [157]

$$\Delta\nu_Q^{(i)} = \frac{3}{2}\chi_Q S_{CD}^{(i)} P_2(\cos\beta_{DL}) \qquad ,(5)$$

where the superscript (*i*) labels individual carbon segments (as described above), and χ_Q = 167 kHz is the static quadrupolar coupling constant [23]. Due to the angular fluctuations, the lipid segment orientations sample a solid angle Ω that is formulated using the three Euler angles $\Omega \equiv (\alpha, \beta, \gamma)$. For liquid-crystal samples, the rapid motions of the phospholipid molecules have axial symmetry about the average bilayer normal (director), and the colatitude β_{PL} describes the average lipid segment orientation within the laboratory frame (L).

As a result, the overall C–^{2}H bond orientation (principal axis, P) with respect to the laboratory (L) frame is described by the angle

β_{PL} which can be split into a part that depends on time and one that is independent of time. The former is described by the angle $\beta_{PD}(t)$ for the temporal fluctuations versus the membrane director (D) frame, and the time-independent part is given by β_{DL}, due to the static orientation of the director with respect to the laboratory frame (given by the main external $\mathbf{B_0}$ magnetic field). The order parameter $S_{CD}^{(i)}$ is thus defined with respect to the bilayer director as an ensemble average over the angular conformations. Referring to Fig. 5, the segmental order parameters are represented by the averaged second-order Legendre polynomial $\langle P_2(\cos\beta_{PD}^{(i)};t)\rangle$ or alternatively the second-rank Wigner rotation matrix elements $\langle D_{00}^{(2)}(\Omega_{PD}^{(i)};t)\rangle$ leading to:

$$S_{CD}^{(i)} = \frac{1}{2}\langle 3\cos^2\beta_{PD}^{(i)}(t) - 1\rangle \qquad .(6)$$

Here $\beta_{PD}^{(i)}(t)$ is the time-dependent angle between the *i*th carbon-deuterium bond (principal axis, P) and the bilayer normal (director, D). The angular brackets indicate a time or ensemble average over those fluctuations with rates in excess of the (quadrupolar) interaction strength in frequency units (Fig. 5). Based on geometrical considerations, the segmental order parameters are negative for polymethylene chains [21]. Lastly, the dependence on bilayer orientation is described by an additional second-order Legendre polynomial $P_2(\cos\beta_{DL}) = (3\cos^2\beta_{DL} - 1)/2$, where $\beta_{DL} \equiv \theta$ is the angle of the bilayer normal (director axis) to the main magnetic field for each chain segment.

Multiple Coordinate Frame Transformations are Treated Using the Closure Property of the Rotation Group—The above decomposition is not limited to just two consecutive frame transformations, however. Using the closure property of the rotation group [23], we can readily expand the transformation matrix elements into a sum over an arbitrary number of coordinate frames. Alternatively, the summation is collapsed to just those frames of interest. We can thus expand the matrix elements corresponding to the β_{PL} angle into a sequence of coordinate transformations by the closure relation from quantum mechanics and group theory [173]. The intermediate frame (I) for a polymethylene chain considers a virtual bond vector (*z*-axis) normal to the H–C–H plane of a methylene group [171, 172, 174] in terms of a liquid-crystal picture [175]. Alternatively, we adopt a polymer physics view of the two individual carbon atoms directly bonded to a methylene group (see below). The local *z*-axis of a three-carbon segment (virtual bond) is considered with respect to the average long-axis orientation of the lipid molecule (the M-frame) within the bilayer. For our purposes, the two approaches are equivalent.

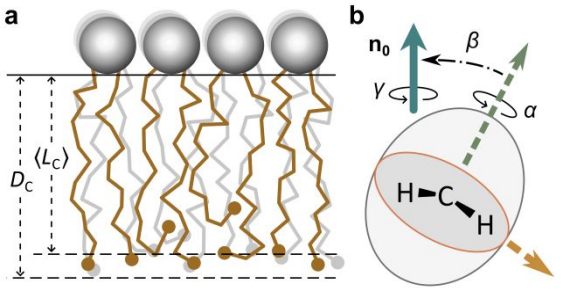

Figure 6. Structural properties for membrane liquid crystals are related to the acyl chain projection onto the bilayer normal and depend on packing of the lipid segments. (a) Schematic representation of methylene chain travel away from the lipid head group–water interface [176]. Methyl groups at ends of the chains are designated by the filled spheres. Note the acyl chains are more disordered in the bilayer center compared to the lipid head groups. (b) The orientation of C–H bonds and projection of carbon segments onto the bilayer normal, $\mathbf{n_0}$, (with finite upturn folding of methylene segments) are related to the average thickness of the membrane. Average projection of the chains corresponds to the experimental order parameters in terms of the orientational distribution function. The spatial orientational of an acyl segment is represented by three Euler angles indicated by $\Omega \equiv (\alpha,\beta,\gamma)$, where $\beta \equiv \beta_{IM}$ for the *i*th segment. **[95% of single-column width]**

Applying the above formulas to bilayers in the liquid-crystalline state, if we assume the added frames have definite orientations or are averaged by the overall motions, then β_{IM} is the relevant angle of interest. (At times we suppress the subscript IM to simplify the notation.) Denoting the segment index by *i,* the distribution of the angles $\beta \equiv \beta_{IM}^{(i)}$ for the various acyl segments is related to the statistical travel of the chains away from the lipid/water interface, i.e., corresponding to the bilayer normal (director). Figure 6 illustrates the chain flux along the reference axis (See below). Additionally, the angle β_{MD} represents the (instantaneous) tilt of the lipid molecule with respect to the local bilayer normal, which appears when treating the dynamics due to collective order fluctuations. The influences of undulations on the order parameter are assumed to be small [88] and are not explicitly considered here. **[FIGURE 6]**

4. Equilibrium Properties of Lipid Bilayers Investigated by Solid-State NMR Spectroscopy

Because of the large number of degrees of freedom, it is challenging to calculate structural parameters explicitly for lipid

bilayer systems. Therefore, for membrane lipids (either multilamellar dispersions, or aligned on solid supports) in the liquid-crystalline state we use statistical models to simplify the problem. We consider an orientational distribution function [172, 177], here designated by $f(\beta)$, where β is a generalized Euler angle (see above). Typically, the Euler angles [178] describe rotations in three dimensions, where successive rotations obey the closure property [173] as mentioned above. The orientational distribution can then be treated in a discrete (lattice) approximation. Alternatively, a continuum approach (potential of mean force) can be introduced, with only a single Euler angle, as in the case of liquid-crystalline bilayers with axial symmetry about the lamellar normal.

One can thus relate the experimental observables to the configurational properties of the acyl chains, which correspond to the average structure of the system [60]. The approach is applicable to polymers, liquid crystals, and biological lipids. With an appropriate choice of the distribution function, we can tackle the problem of calculating the average projected acyl chain length $\langle L_C \rangle$ or the average cross-sectional area per lipid $\langle A \rangle$ from the spectroscopic observables. For example, the average projection of an individual chain segment is given by finding the average of $\cos\beta_i$ representing the statistical methylene travel along the bilayer normal. The result of this statistical average depends on the chosen distribution function in the model [172]. When we add up the cumulative travel of the individual segments, we obtain the total methylene travel (flux), giving the average projected chain length. Calculation of the area per lipid is more complicated, however, because it requires finding the average of $1/\cos\beta_i$ as first pointed out in Ref. [172]. Further implications are discussed in the upcoming sections.

4.1. The Orientational Distribution Function

In general, the ensemble average of any angular-dependent property denoted by $A(\beta)$ can be written and calculated using an orientational distribution function $f(\beta)$ [24],

$$\langle A(\beta) \rangle = \frac{\int_{-1}^{1} A(\beta) f(\beta) d\cos\beta}{\int_{-1}^{1} f(\beta) d\cos\beta} \qquad .(7)$$

At this level, β is a generalized Euler angle, which is specified later when particular models are introduced. The orientational distribution function $f(\beta)$ can be expanded in a complete set of orthogonal polynomials, e.g., the Legendre polynomials $P_j(\cos\beta)$, as

$$f(\beta) = \sum_{j=0}^{\infty} c_j P_j(\cos\beta) \qquad ,(8)$$

where c_j are numerical coefficients. Here we recall that the Legendre polynomials $P_j(\cos\beta)$ obey the orthogonality relation

$$\int_{-1}^{+1} P_j(x)\, P_k(x) dx = \frac{2\delta_{jk}}{2j+1} \qquad ,(9)$$

where $x \equiv \cos\beta$ and δ_{ik} is the familiar Kronecker delta function [179].

Next, in the usual way, we left multiply the distribution function by a different Legendre polynomial. We then can integrate over the full angular range, and employ the orthogonality of the complete basis set. Using Eqs. (8) and (9) allows us to readily solve for the expansion coefficients:

$$c_j = \left(\frac{2j+1}{2}\right) \langle P_j(\cos\beta) \rangle \qquad .(10)$$

Notably $\langle P_j(\cos\beta) \rangle$ corresponds to the moments of the $f(\beta)$ distribution, i.e., the orientational order parameters:

$$\langle P_j(\cos\beta) \rangle = \frac{\int_{-1}^{1} P_j(\cos\beta)\, f(\beta) d\cos\beta}{\int_{-1}^{1} f(\beta) d\cos\beta} \qquad .(11)$$

Inserting Eq. (10) back into Eq. (8), we then obtain our distribution function in terms of the Legendre polynomials, and their corresponding moments:

$$f(\beta) = \sum_{j=0}^{\infty} \left(\frac{2j+1}{2}\right) \langle P_j(\cos\beta) \rangle\, P_j(\cos\beta) \qquad .(12)$$

Obviously the knowledge of all the moments is needed to completely specify the distribution function [177]. But the order parameter measured by ^{2}H NMR spectroscopy is only related to the second moment $\langle P_2(\cos\beta) \rangle$ of the orientational distribution function $f(\beta)$. Moreover $f(\beta)$ is a function of both even- and odd-rank order parameters, including of particular interest the odd-rank term $\langle P_1(\cos\beta) \rangle$, which is related to the acyl chain travel (segmental projection) on the bilayer normal. One therefore needs to use a model for the segmental conformations to reconstruct $\langle P_1(\cos\beta) \rangle$ from the given $\langle P_2(\cos\beta) \rangle$ value. In other words, we need to assume a functional form for the orientational distribution function $f(\beta)$. For lucid discussions of orientational distribution functions in liquid crystals, see the work of Jack Freed et al. and Claudio Zannoni et al. [180]

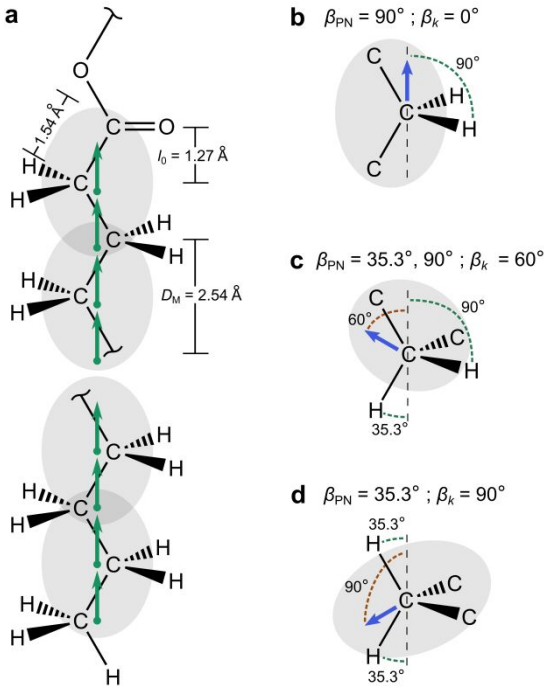

Figure 7. Geometric models for acyl segment orientations determine average lipid structure for liquid-crystalline bilayers using statistical methods. (a) The all-*trans* reference state has its long axis parallel to the average bilayer normal. Projections of carbon–carbon bonds onto the long axis are of length l_0 = 1.27 Å (indicated by arrows) [174, 181]. Virtual bonds are taken as joining the carbons to either side of a given carbon position in the chain with length $D_M = 2.54$ Å (cf. text). (b)–(d) Diamond-lattice model is based on three discrete orientations of a chain methylene group (chain upturns are neglected). The C–^{2}H bond (principal axis of electric field gradient tensor) orientation to the molecular axis is designated as β_{PD} and β_k denotes the *k*th virtual bond (vector) orientation for a given segment. (Collective fluctuations of the local director axis [18] are not included and thus the molecular frame M and director frame D are equivalent.) The average chain travel is the sum of average virtual bond (vector) projections corresponding to the three diamond-lattice orientations. Both diamond-lattice and continuous mean-torque models as applied to solid-state ^{2}H NMR experiments reveal average structural properties of membrane bilayers. **[90% of single-column width]**

Structural Properties of Bilayer Lipids are Calculated from the Orientational Distribution Function—With the preceding framework in hand, we are now equipped to analyze the configurational statistics of the various segments of the flexible membrane lipids. For a methylene group, the relevant Euler angle $\beta = \beta_{IM}$ is between the normal to the plane of the H–C–H atoms of the internal frame (I) and the average (long-axis) molecular frame (M) (Fig. 5). This definition naturally lends itself to a liquid-crystalline picture for the individual segments of the bilayer [175]. Alternately, for an individual segment *i* we can consider the three carbon atoms from C_{i-1} to C_{i+1} in terms of a virtual bond of length 2.54 Å as in the case of methylene groups [24]. The virtual bonds (statistical segments) correspond to a freely jointed chain, or to other models used in polymer physics. The two alternate definitions are illustrated in Fig. 7—each has its own merits and limitations [24]. Because for our purposes these two options are equivalent, we shall utilize three-carbon segments of the polymethylene chain [24]. The $C_{i-1}-C_{i+1}$ carbon segments are considered with respect to the reference all-*trans* long chain axis (Fig. 7). In what follows, we retain the segment index *i*, but at times we suppress the subscript IM to simplify the notation. **[FIGURE 7]**

The average segment projection onto the bilayer normal can then be written in terms of the first moment as

$$\langle D_i \rangle / D_M = \langle \cos \beta_i \rangle \qquad ,(13)$$

where D_i is the length of the virtual bond between carbon atoms $i+1$ and $i-1$ projected onto the bilayer normal, and D_M is the maximum projection of 2.54 Å (see Fig. 7). Take note that the segment index *i* includes carbon atoms $i+1$ and $i-1$. The sum of all of the three-carbon segment projections for a given acyl chain configuration gives us the total projected length L_C or travel of the hydrocarbon chain. Upon averaging over all the orientations, the averaged projected length becomes

$$\langle L_C \rangle = \frac{1}{2} \sum_{i=m}^{n_c-1} \langle D_i \rangle + \langle D_{n_c-1} \rangle \qquad ,(14)$$

where n_c is the number of carbons per chain. The factor of $1/2$ arises because the virtual bonds (defined above) connect every other carbon atoms, while the sum is taken over all methylene carbons from $i = m = 2$ to $i = n_c - 1$, for simplicity. The additional term $\langle D_{n_c-1} \rangle$ accounts for the extent of the terminal methyl group. This formula enables one to directly calculate the average hydrocarbon chain length projected onto the bilayer normal [24].

Configurational Statistics of Acyl Chains Explain Their Travel Away From the Aqueous Interface—Coming back to Fig. 6, the concept is illustrated of the methylene chain travel (or flux) away from the head groups located near the water interface. The statistical chain travel along the bilayer normal depends on the angular fluctuations of the individual acyl chain segments, which

are effectively tethered to the bilayer aqueous interface via the lipid head groups. In Fig. 6(a), the angular fluctuations of the lipid segments (electric field tensor of C–^{2}H bond) are described by the three Euler angles $\Omega = (\alpha, \beta, \gamma)$. For the overall rotation to the bilayer aqueous interface (as a rule we write Ω for the solid angle), the Euler angles correspond (in sequence) to rotation about the normal to the H–C–H plane of a methylene segment, the rotation of the segmental frame to the frame whose z-axis is the bilayer normal, and lastly rotation about the bilayer normal (director). We can thus connect the angular-dependent ^{2}H NMR observables to the spatial projection (or travel) of the acyl chains along the bilayer normal (director axis). In Fig. 6, the distribution is represented by the projections along the hydrocarbon chain L_C. The methyl groups are broadly distributed along the bilayer normal direction, indicating the individual chains terminate at various distances from the water interface, due to the statistical distribution of *gauche* isomers. Note also that $\langle L_C \rangle$ and D_C are not equal, because the volumetric thickness is calculated from the area per lipid, and not from the acyl projections [24].

4.2. Area per Lipid Molecule at the Aqueous Interface in Membrane Bilayers

Given the above statistical model, we are able to calculate the average cross-sectional area per lipid $\langle A \rangle$ at the bilayer interface with water, e.g., in the case of unsupported multilamellar lipid dispersions. One of the most fundamental properties of a lipid bilayer—and one of the most important ways to establish whether the system has achieved equilibrium in molecular simulations (both atomistic and coarse-grained)—is the area per lipid at the aqueous interface [24, 182]. When the area per lipid molecule at the interface with water reaches a stable value, most other structural properties do not change, and the system has converged [183]. Knowledge of the area per lipid thus plays a central role in validating MD simulations of lipid bilayers. It is also needed for quantifying membrane deformations, as well as for understanding the effects of additives such as cholesterol or membrane-active peptides [184, 185].

For a chain segment confined by its neighbors, its degrees of freedom are limited by the volume within it can move. By working out the average travel of a methylene chain segment, we can deduce the average area $\langle A \rangle$ per lipid molecule, which for a symmetric (like chain) lipid is twice the area $\langle A_C \rangle$ per chain [24]. Assuming the average shape of the hydrocarbon chain can be approximated by a geometrical prism (as obtained from a statistical average of Voronoi tessellations or equivalently in this case, seen as Wigner-Seitz cells [186-189]), the cross-sectional area for a statistical segment comprising two methylene groups reads:

$$A_C^{(i)} = \left\langle \frac{2V_{CH_2}}{D_i} \right\rangle = \frac{2V_{CH_2}}{D_M} \left\langle \frac{1}{\cos \beta_i} \right\rangle \qquad (15)$$

Here V_{CH_2} is the thermodynamic volume of an individual methylene group fluctuating in the confinement of its neighbors [154, 190, 191]. The factor of two appears because the virtual bond length accounts for two CH_2 groups.

Now, in computing the average interfacial (cross-sectional) area per chain $\langle A_C^{(i)} \rangle$, the value of the area factor $q_i = \langle 1/\cos \beta_i \rangle$ is needed [172]. Expanding the function about $x \equiv \cos \beta = 1$ (where $f(\beta)$ is assumed to have a maximum), and truncation of the Taylor series gives [24]:

$$q_i = \langle 1/\cos \beta_i \rangle \approx 3 - 3\langle \cos \beta_i \rangle + \langle \cos^2 \beta_i \rangle \qquad (16)$$

It is assumed that upturning (or back-folding) of a methylene segment is statistically negligible. Such an approximation is needed because $\langle 1/\cos \beta_i \rangle$ has a singularity at $\beta_i = \pi/2$. Obviously this approximation does not work for highly mobile methylene segments, and rather, the approach is most applicable to methylene segments near the lipid head group (so-called plateau region of the order parameter profile) [157]. For the plateau region, we suppress the index (i), so that the average cross-sectional area of a lipid chain in terms of q is denoted by:

$$\langle A_C \rangle = \frac{2V_{CH_2}}{D_M} q \qquad (17)$$

The reader should note that in the limit of an all-*trans* chain rotating about the bilayer normal with axial symmetry, $\langle \cos^2 \beta \rangle = \langle \cos \beta \rangle = 1$, giving $q = 1$. Hence the limiting area per chain is $2V_{CH_2}/D_M$ in keeping with Eq. (15). For a mixture of chains, the area factor q is the weighted sum, and the calculated value of $\langle A \rangle$ is the number-weighted average over the components, according to the theory of moments [147].

Next, with the area per chain given in Eq. (17), and knowing the volume V_C, the thickness of an individual monolayer is calculated as

$$D_C = \frac{n_C D_M}{2q} \qquad (18)$$

where n_C is the number of carbons (e.g., $n_C = 16$ for DPPC). Note

that because the volume of the terminal methyl group is practically twice the volume of a methylene group [154], we have $n_C \cong V_C / V_{CH_2}$. And again recall the volumetric thickness D_C is not the same as the average projected chain length $\langle L_C \rangle$ as shown by Fig. 6 [24]. The next step is to work out the average projection of the segments $\langle \cos \beta_i \rangle$ and the area factor q. Using Eq. (5), we can calculate $\langle P_2(\cos \beta_i) \rangle$ and thus $\langle \cos^2 \beta_i \rangle$ whereas we need to know $\langle P_1(\cos \beta_i) \rangle = \langle \cos \beta_i \rangle$. Hence, we must return to the problem of constructing $\langle P_1(\cos \beta_i) \rangle$ from the observed value of $\langle P_2(\cos \beta_i) \rangle$ by considering the orientational distribution function.

5. Modeling the Configurational Statistics of Lipid Chains in Membrane Liquid Crystals

Because of the large number of degrees of freedom, from experimental measurements it is challenging to calculate structural parameters analytically for a membrane lipid bilayer. Hence we are naturally led to the language of distribution functions for the case of multilamellar lipid dispersions, either as freely suspended bilayers or aligned on solid substrates. As a general rule, the orientational distribution function for flexible molecules is characterized by its moments (see above). Consequently we shall introduce simple statistical models to reduce the parameter space for the ensemble-averaged properties. In this section, our aim is to establish the utility of the models in terms of their statistical approximations. Our basic strategy is to reconstruct the first moment of the segmental or molecular orientational distribution $\langle P_1(\cos \beta_i) \rangle$ from a given value of the second moment $\langle P_2(\cos \beta_i) \rangle$. That will allow us to express the average membrane structure [159] in terms of the orientational distribution function [24].

Referring to the above discussion, two alternate formulations are possible. The liquid crystal view considers virtual bond vectors of length l_0 =1.27 Å perpendicular to the methylene H–C–H plane [174]. Alternatively, with a polymer physics view, the virtual bonds of length D_M=2.54 Å join carbon atoms C_{i-1} and C_{i+1} representing the extent of three-carbon segments of the chain [24]. We recall the latter picture (Fig. 7) is analogous to a freely jointed chain used in polymer physics [24]. For anisotropic mesophases of flexible molecules, the transformations are from the principal axis system P to the internal frame I, and then from the I-frame to the average molecular frame M congruent with the bilayer normal ($\beta_{IM} = \beta_{ID}$).

5.1. Lattice Models for Orientational Distributions of] Lipid Acyl Segments—Polymer Physics Viewpoint

Introduction of a diamond-lattice model approximates the carbon–deuterium bond orientations by a tetrahedral lattice (hence diamond-lattice model). This model reduces the continuous parameter space to a more tractable discrete set. For highly mobile lipids, it is analytically solvable by neglecting back-folded orientations (which are statistically less significant). A schematic depiction is provided in Fig. 7 of the tetrahedral orientations. For the diamond-lattice model, the appropriate Euler angle is $\boldsymbol{\beta} = \boldsymbol{\beta}_{IM}$ where the segment index is suppressed for clarity. Assuming discrete segmental orientations, in Eq. (12) the various moments of the segmental distribution are given by:

$$\langle P_j(\cos\beta) \rangle = \sum_k p_k \, P_j \, (\cos\beta_k) \qquad .(19)$$

The probabilities p_k are normalized, and hence they sum to unity (k denotes the lattice orientations and is not to be confused with the segment index i which is suppressed; more explicitly, $\beta_k \equiv \beta_{IM}^{(k)}$). Next, we can insert Eq. (19) into Eq. (12) to yield the following segmental distribution function:

$$f(\beta) = \sum_{j=0}^{\infty} \left(\frac{2j+1}{2} \right) \sum_k p_k P_j(\cos\beta_k) \, P_j(\cos\beta) \qquad .(20)$$

Applying the orthogonality relation of Eq. (9), we then obtain for the diamond-lattice model a sum of Dirac delta functions,

$$f(\beta) = \sum_k p_k \delta(\beta - \beta_k) \qquad ,(21)$$

for the discrete distribution.

Lipid Chain Travel on a Diamond Lattice Involves a Statistical Distribution of Segment Orientations—Obviously, for the diamond-lattice model there is a set of discrete orientations that have a finite probability. As discussed by Jansson et al. [155], the possible orientations are $\beta_k =$ 0°, 60°, and 90° plus the back-folding (upturn) angles, 120° and 180°. If the back-folding orientations are neglected [171, 174], then for each segment the order parameter is given by Eq. (6), and the orientational distribution function, Eq. (21), becomes (see Fig. 6):

$$S_{CD}^{(i)} = \langle P_2(\cos \beta_i) \rangle = \frac{\sum_k \int_{-1}^{1} P_2(\cos \beta_i) \, p_k \, \delta(\beta - \beta_k) \, d\cos\beta}{\sum_k \int_{-1}^{1} p_k \, \delta(\beta - \beta_k) \, d\cos\beta} \qquad .(22)$$

In what follows, to simplify the notation the index i is suppressed on the right. Solving Eq. (22) using the discrete diamond-lattice orientations, we obtain the order parameter for the individual acyl

segments:

$$S_{\mathrm{CD}}^{(i)} = p_0 P_2(\cos 90°) + \frac{p_{60}}{2}[P_2(\cos 35.3°) + P_2(\cos 90°)] + p_{90} P_2(\cos 35.3°) \quad .(23)$$

(The probabilities p_0, p_{60}, and p_{90} depend on the segment index i which is suppressed.)

Inserting the corresponding numerical values for the Legendre polynomials, we find that:

$$S_{\mathrm{CD}}^{(i)} = \frac{1}{2}(-p_0 + p_{90}) \quad .(24)$$

Here we have again used Eq. (9) for the orthogonality of the Legendre polynomials. From Eq. (13), the projected length of a three-carbon segment $\langle D_i \rangle$ becomes:

$$\frac{\langle D_i \rangle}{D_{\mathrm{M}}} = \langle \cos \beta_i \rangle = p_0 P_1(\cos 0°) + p_{60} P_1(\cos 60°) + p_{90} P_1(\quad .(25)$$

Lastly, inserting the numerical values for the Legendre polynomials yields the result that:

$$\frac{\langle D_i \rangle}{D_{\mathrm{M}}} = p_0 + \frac{p_{60}}{2} \quad .(26)$$

The above formula allows the segmental projection onto the reference all-*trans* state (taken as congruent with the average bilayer director) to be calculated in terms of the rotamer probabilities.

Projected Chain Length and Lipid Area Manifest the Chain Travel on the Lattice—Considering the entire chain, we calculate its projected length in terms of the segment travel (flux) along the bilayer normal. Recognizing the probabilities of the rotational isomeric states sum to unity, and neglecting back folding, by summing Eqs. (24) and (26) the projected length in terms of the segmental order parameter can be worked out:

$$S_{\mathrm{CD}}^{(i)} + \frac{\langle D_i \rangle}{D_{\mathrm{M}}} = \frac{p_0}{2} + \frac{p_{60}}{2} + \frac{p_{90}}{2} = \frac{1}{2} \quad .(27)$$

It follows that for a three-carbon segment, the average distance projection along the bilayer normal reads:

$$\frac{\langle D_i \rangle}{D_{\mathrm{M}}} = \langle \cos \beta_i \rangle = \frac{1}{2}\left(1 - 2S_{\mathrm{CD}}^{(i)}\right) \quad .(28)$$

The above formula corresponds to the first moment of the orientational distribution function. Here D_i is the distance between carbon atoms $i + 1$ and $i - 1$ projected onto the bilayer normal, and D_{M} is the maximum projection of 2.54 Å (as shown in Fig. 7). Note that in the limit of an all-*trans* chain, $S_{\mathrm{CD}}^{(i)} = -1/2$ giving $\langle D_i \rangle = D_{\mathrm{M}}$ as expected.

Based on our analysis, the average chain length along the bilayer normal is the sum of the average projections of the individual segments. By using Eq. (14), and knowing the order parameters along the acyl chain, we can calculate the methylene contributions to the projected length:

$$\frac{\langle L_{\mathrm{C}} \rangle}{D_{\mathrm{M}}} = \frac{1}{2} \sum_{i=m}^{n_{\mathrm{C}}-1} \frac{1}{2}\left(1 - 2S_{\mathrm{CD}}^{(i)}\right) \quad .(29)$$

Here $m = 2$ is the first methylene carbon of the chain, and n_{C} is the ending carbon (due to the terminal methyl group). Note that the methyl segment requires a special treatment, as the virtual bond cannot be defined as for the methylene groups. The three-fold rotational symmetry projects the residual quadrupolar coupling along the carbon–carbon bond [192], leading to $S_{\mathrm{CD}}^{(n_{\mathrm{C}})} P_2(\cos 109.5°) = S_{\mathrm{CD}_3}$ which corresponds to $S_{\mathrm{CD}}^{(n_{\mathrm{C}})} = -3S_{\mathrm{CD}_3}$. Accounting for the methyl group symmetry, the projected acyl length is thus found to be: [174]

$$\frac{\langle L_{\mathrm{C}} \rangle}{D_{\mathrm{M}}} = \frac{1}{2}\left[\frac{n_{\mathrm{C}} - m + 1}{2} + \sum_{i=m}^{n_{\mathrm{C}}-1} \left|S_{\mathrm{CD}}^{(i)}\right| + \left|3S_{\mathrm{CD}}^{(n_{\mathrm{C}})}\right|\right] \quad .(30)$$

The sum is taken over all the carbons from $m = 2$ to $n_{\mathrm{C}} - 1$, and the order parameters have a negative sign. In the limit of an all-*trans* rotating chain, $S_{\mathrm{CD}}^{(i)} = -1/2$ and $S_{\mathrm{CD}}^{(n_{\mathrm{C}})} = (-1/3)(+1/2) = (-1/6)$ giving $\langle L_{\mathrm{C}} \rangle = (n_{\mathrm{C}} - 1)(D_{\mathrm{M}}/2)$ for the projected acyl length. As pointed out by Nagle et al [193], the assumption of no upturns of the methylene segments can fail for segments close to the acyl end, where disorder is larger and Eq. (28) does not hold.

More realistic calculations of membrane thickness (rather than acyl chain length) directly work out the area, Eq. (17), and then introduce the volumetric acyl thickness using Eq. (18). Only the largest order parameter is required, avoiding some of the ambiguities due to the no-upturns approximation [24]. Studies of various lipid bilayers indicate the order parameter $S_{\mathrm{CD}}^{(i)}$ shows a plateau value as a function of the chain position (i), which is designated by $S_{\mathrm{CD}}^{\mathrm{plat}}$ due to the acyl segments close to the aqueous interface [194]. Combining Eqs. (6) and (28) with Eqs. (16) and (17), we obtain the diamond-lattice result for the area per chain:

$$\langle A_{\mathrm{C}} \rangle = \frac{2V_{\mathrm{CH_2}}}{D_{\mathrm{M}}}\left(\frac{11}{6} + \frac{5}{3}S_{\mathrm{CD}}^{\mathrm{plat}}\right) \quad .(31)$$

Here the area factor q for the plateau segments is the quantity within the parentheses, and S_{CD}^{plat} designates the largest (plateau) value of the order parameter [194]. Using Eq. (18) together with Eq. (31), the volumetric thickness thus reads:

$$D_C = \frac{n_C D_M}{2}\left(\frac{11}{6} + \frac{5}{3}S_{CD}^{plat}\right)^{-1} \quad .(32)$$

Nagle and co-workers [193] have concluded that the diamond-lattice result is not accurate for calculating $\langle \cos \beta_i \rangle$ for highly mobile carbon segments. Calculating the area factor with a different formula, $q = 1/\langle \cos \beta \rangle$, corrects some of the problems with the diamond-lattice model. However, the validity of the geometrical average has been questioned [24, 172].

5.2. Continuum Model Using Potential of Mean Force—Liquid-Crystal Viewpoint

Alternatively, instead of sampling the discrete orientations of the lipid acyl segments, the mean-torque model of Petrache et al. [24] assumes the segment orientations obey a continuous distribution. The assumption of a continuous orientational potential is equivalent to applying an average torque on a methylene segment, hence the designation mean-torque model [24]. This approach is more akin to a liquid crystal view of the membrane, wherein the various segments of the flexible lipid molecules are subject to a orienting potential, as in the case of nematic or smectic liquid crystals [175]. The advantage is the model does not assume specific orientations of the methylene segments.

For the case of liquid-crystalline membranes, in Fig. 8 the transformations considered by the mean-torque model are illustrated in more detail. The orientation of a C–^{2}H bond is considered as the principal axis system (P), which is then projected onto a sequence of intermediate frames, until we reach the laboratory frame (L) (due to closure). As with the diamond-lattice, we are primarily interested in the projection of the intermediate axis (I) of a three-carbon segment onto the molecular axis (M). Fluctuations about the director axis (D) are neglected; and so the molecular and director frames are taken as equivalent. Again, we suppress the segment index to simplify the notation. **[FIGURE 8]**

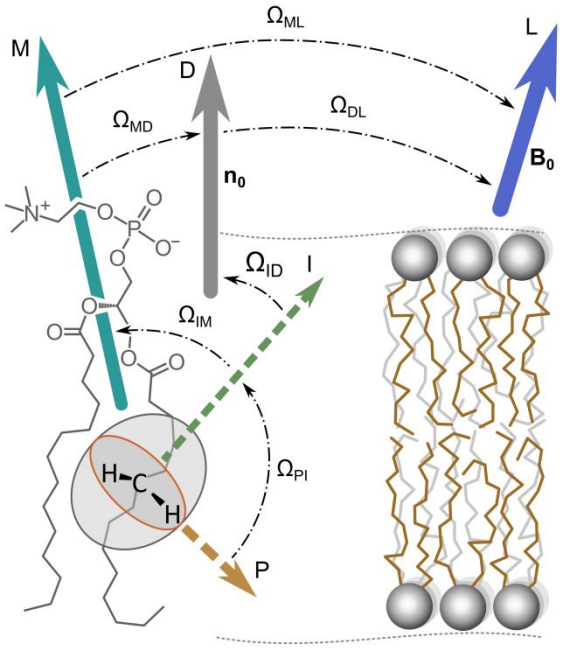

FIGURE 8. Lipid bilayer properties depend on the molecular orientation and mobility of carbon segments as investigated by NMR spectroscopy. Experimental observables depend on orientation of the molecular segment and can be decomposed into the series of coordinate frames. Use of the closure property of the rotation group simplifies the coordinate transformations. The frame of the C–^{2}H bond is the principal axis system (P) for the segmental order parameter, and the main external magnetic field $\mathbf{B_0}$ defines the laboratory frame (L). Designations for the Euler angles Ω are: P, principal axis system for ^{2}H nucleus (z-axis parallel to C–^{2}H bond); I, intermediate frame for methylene group motion (z-axis perpendicular to ^{2}H–C–^{2}H plane); M, molecular coordinate system; D, director frame (z-axis is bilayer normal); and L, laboratory system (z-axis along main external magnetic field $\mathbf{B_0}$). Treatment of the segmental orientation with respect to the laboratory axis system uses a set of intermediate frames that facilitates description of the bilayer properties. **[85% of single-column width]**

Mean-Torque Potential Corresponds to Moments of Orientational Distribution Function—We begin with the distribution function for a given orientational potential, as in the diamond-lattice model. The orientational distribution of each methylene segment is written in terms of the Boltzmann factor,

$$f(\beta) = \frac{1}{Z}\exp\left(-\frac{U(\cos\beta)}{k_B T}\right) \quad ,(33)$$

where the partition function reads:

$$Z = \int_{-1}^{+1} \exp\left(-\frac{U(\cos\beta)}{k_B T}\right) d\cos\beta \quad .(34)$$

In the above formula, $U(x)$ is the orientational potential for an

individual carbon segment, and $x \equiv \cos\beta$. To simplify the notation, for the mean-torque model, $\beta = \beta_{\mathrm{ID}}$ where the suffix and superscripts (i) for the segment index are suppressed. For the statistical treatment of the methylene segments, it is assumed the orientational order can be described by $U(x)$, which is called the potential of mean torque. In a first-order approximation, the potential is given by

$$U(\cos\beta) = \sum_j U_j P_j(\cos\beta) \approx U_1 \cos\beta \qquad (35)$$

where U_1 is the first-order mean-torque parameter. Obtaining these parameters for each chain segment gives us the desired information about the stress profile of the bilayer.

According to the mean-torque model, the first and second moments of the orientational distribution are obtained by integrating Eq. (11) with use of Eqs. (33)–(35) for the distribution function:

$$\langle P_j(\cos\beta)\rangle = \frac{1}{Z}\int_{-1}^{+1} P_j(\cos\beta)\exp\left(-\frac{U(\cos\beta)}{k_{\mathrm{B}}T}\right)d\cos\beta \qquad (36)$$

With the linear approximation of the potential, this integral can be put in closed form, yielding

$$\langle P_1(\cos\beta)\rangle = \langle\cos\beta\rangle = \coth\left(\frac{U_1}{k_{\mathrm{B}}T}\right) + \frac{k_{\mathrm{B}}T}{U_1} \qquad (37)$$

and

$$\langle P_2(\cos\beta)\rangle = 1 + 3\left(\frac{k_{\mathrm{B}}T}{U_1}\right)^2 + 3\frac{k_{\mathrm{B}}T}{U_1}\coth\left(\frac{U_1}{k_{\mathrm{B}}T}\right) \qquad (38)$$

The second moment of the distribution, Eq. (38), is measured directly from solid-state ^{2}H NMR experiments for the segmental order parameter $\langle P_2(\cos\beta_{PD})\rangle = S_{\mathrm{CD}}^{(i)}$ as given by Eq. (6), where the segment index i has now been reintroduced. Taking the factor of $P_2(\cos\beta_{\mathrm{Pl}}) = P_2(\cos 90°) = -1/2$ for the methylene segments into consideration then gives $\langle\cos^2\beta_i\rangle = \left(1 - 4S_{\mathrm{CD}}^{(i)}\right)/3$ for the second moment.

Next, Eq. (38) can be numerically solved to find the first mean-torque parameter U_1 corresponding to an individual segment in the chain. If U_1 is known, then the average projection, Eq. (37), can be found, and the chain length $\langle L_{\mathrm{C}}\rangle$ can be worked out. An analytical solution for $\langle\cos\beta_i\rangle$ is obtained when the segment confinement exceeds the thermal energy, which is expected for highly ordered segments in the plateau region. We can use the approximation $\coth(U_1/k_BT) \approx 1$, which holds very well for $U_1 > 2k_BT$ and so we obtain:

$$\langle P_1(\cos\beta_i)\rangle = \langle\cos\beta_i\rangle = \langle D_i\rangle/D_{\mathrm{M}} \cong (1/2)\left(1 + \sqrt{\left(-8S_{\mathrm{CD}}^{(i)} - 1\right)/3}\right) \qquad (39)$$

As mentioned above, the above approximation assumes there are no upturns for segments with a sufficiently strong orienting potential. This relation is valid only for order parameters in the interval $-1/8 < S_{\mathrm{CD}}^{(i)} < -1/2$, where we recall that the order parameter is negative. The above relation was found by Petrache et al. [193] to be a more accurate way of calculating $\langle\cos\beta_i\rangle$ when compared to the diamond-lattice model.

Projected Chain Length and Area Per Lipid Depend on Chain Flux Along the Bilayer Normal—Using Eq. (14) together with Eq. (39), and knowing the order parameters along the acyl chain, we are now able to work out the average projected acyl length as the sum of the average segment projections:

$$\frac{\langle L_{\mathrm{C}}\rangle}{D_{\mathrm{M}}} = \frac{1}{2}\sum_{i=m}^{n_{\mathrm{C}}-1}\left(1 + \sqrt{\frac{-8S_{\mathrm{CD}}^{(i)} - 1}{3}}\right) \qquad (40)$$

For highly mobile lipids, the order parameter for the terminal methyl groups is very low (albeit negative), which can generate an imaginary result. In these situations, Eq. (38) should be solved numerically. Here again, we have to correct for the terminal methyl group, as we did with Eq. (30). The result is:

$$\frac{\langle L_{\mathrm{C}}\rangle}{D_{\mathrm{M}}} = \frac{n_{\mathrm{C}} - m + 1}{2} + \sum_{i=m}^{n_{\mathrm{C}}-1}\sqrt{\frac{-8S_{\mathrm{CD}}^{(i)} - 1}{3}} + \sqrt{\frac{-24S_{\mathrm{CD}}^{(n_C)} - 1}{3}} \qquad (41)$$

To avoid over-parameterizing the problem, the mean-torque model treats the orientational potential as a single degree of freedom. However, this simplification may not be accurate for more highly mobile segments near the ends of the lipid chains, which can have more complicated distribution functions. Still, we can avoid some of the difficulty by focusing on the plateau region of the order parameter profile, using Eq. (39) and Eq. (38) to calculate the area factor q analytically.

In this way, combining Eq. (6) and Eq. (39) with Eq. (16) and Eq. (17), we obtain the mean-torque expression for the average area per chain, which reads:

$$\langle A_{\mathrm{C}}\rangle \cong \frac{2V_{\mathrm{CH_2}}}{D_{\mathrm{M}}}\left(\frac{11}{6} - \frac{1}{2}\sqrt{3\left(-8S_{\mathrm{CD}}^{\mathrm{plat}} - 1\right)} - \frac{4}{3}S_{\mathrm{CD}}^{\mathrm{plat}}\right) \qquad (42)$$

As before, the area factor q is contained in the parentheses, and the order parameter values are negative numbers. The calculations of the area per lipid in this perspective utilize this model. This method of calculating the average cross-sectional chain area, using

the mean-torque model, agrees with the results of other experimental approaches [193]. Lastly, by using Eq. (18) with (42), the volumetric thickness is found to be:

$$D_C = \frac{n_C D_M}{2}\left(\frac{11}{6} - \frac{1}{2}\sqrt{3\left(-8S_{CD}^{plat} - 1\right)} - \frac{4}{3}S_{CD}^{plat}\right)^{-1} \quad (43)$$

In the above calculations only the plateau region of the order parameter profile is used, as noted above.

6. Equilibrium Thermodynamics of Membrane Deformation

Let us next turn our attention to how the structural parameters obtained from solid-state ^{2}H NMR spectroscopy of multilamellar lipid dispersions are used to gain insight into the forces governing membrane organization. Bilayer remodeling and deformation, e.g., in response to external stresses and perturbations, are of great biophysical interest [59]. Experimental methods to investigate molecular interactions in phospholipid assemblies include the osmotic stress method [50], use of surface forces apparatus [195], and micropipette aspiration techniques- [7, 196, 197]. Because solid-state ^{2}H NMR spectroscopy yields atom-specific knowledge of liquid-crystalline phospholipids, see Fig. 4(a), it can transform our understanding of how the material properties emerge from atomistic-level interactions based on the intermolecular forces [198-200].

The question then becomes: How can the atomistic approach of solid-state ^{2}H NMR spectroscopy be combined with force-based methods to explain the interactions in lipid bilayers? Here we are interested in the distance ranges and magnitudes, and whether and how bilayer deformation occurs in response to osmotic or hydrostatic pressure [26]. Indeed, significant bilayer structural changes have been observed to occur with osmotic pressures in the biological range (up to ~100 atm). That raises the interesting possibility that osmotic stress-induced bilayer deformation may influence or govern the actions of membrane proteins, such as ion channels or G-protein-coupled receptors (GPCRs) [201-203], e.g., through chemically nonspecific lipid-protein interactions [43]. Membrane protein-surface shaping properties of lipids can give a potential mechanism for altering the activities of membrane proteins within cells and tissues.

6.1. Osmotic Stress as a Force-Based Method for Investigating Emergent Membrane Properties

Application of osmotic pressure to multilamellar lipid dispersions affords a direct connection to the equilibrium thermodynamics of membrane interactions. By introducing the mathematical formalisms of thermodynamics, we can establish how the energetics of membrane interactions and structural deformation are related to bilayer forces. The idea of balancing the free energy of the multilamellar lipid phase with the osmotic stress due to external factors is central to our approach. Transferring water from the lipid phase into the stressing polymer solution (osmolyte phase) reduces the free energy of the system, maximizing the entropy of the osmolyte. Alternatively, gravimetric control of water in the multilamellar lipid phase is possible. In both cases, deformation of the multilamellar phase occurs in two ways: (*i*) the interlamellar repeat spacing decreases, and (*ii*) the membrane thickness increases as a result of water removal from the headgroup region [26, 71].

Osmotic Stress Measurements Provide the Link Between Structure and Interactions—Introduction of osmotic pressure is a practical way to control the hydration of biological specimens, allowing for systematic study of the forces acting upon biological materials, as introduced by Adrian Parsegian and Peter Rand [204-206]. Understanding how molecular assemblies deform under osmotic stress gives us insight to the hierarchy of intermembrane forces [111]. It is important to note that osmotic stress is not just an experimental trick to play with molecular forces. Biological environments at the cellular level can be highly crowded, exerting an appreciable osmotic pressure on biological structures (Fig. 1) [207]. Intra and intercellular osmotic pressures occur due to the competition of various molecular species for available water, and due to their selective partitioning across lipid membranes. For proteins embedded within the thylakoid membranes of chloroplasts, or retinal rod disks, one must wonder if their response to osmotic pressure could be governed by structural deformation of the lipids. Osmotic pressures can exert significant effects on the activities of mechanosensitive ion channels [208], as well as GPCRs such as rhodopsin [209]. Dehydration also affects biomembrane structural integrity, as seen for sarcoplasmic reticulum membranes containing the calcium transport protein (Ca^{2+}-ATPase) [210], and in the case of anhydrobiasis [211, 212]. Experimental work measuring this deformation has yielded mixed results in the past [71, 200, 213-216]. Our understanding of quantitative membrane area deformation due to osmotic stress is thus far from complete.

The osmotic stress method is based on the principle that the (reversible) work of removing water from a lipid bilayer phase

matches the free energy of deforming the multilamellar lattice (including changes in bilayer separation and structural deformation of bilayers) [217]. Transferring water from the lipid phase to another phase with lower chemical potential (e.g., a polymer osmolyte phase in thermodynamic equilibrium with the lipid phase) balances the free energy (work) of bilayer interaction (separation) and of structural deformation [50, 118, 200, 218]. At equilibrium, the chemical potentials of water in the two phases are equal. Referring now to Fig. 9(a), the lipid phase is separated from the osmolyte phase either by a semi-permeable membrane, or by a virtual (imaginary) Gibbs dividing surface that bisects the system into thermodynamically distinct lipid and osmolyte phases. Because of an unfavorable loss of entropy, the high molar mass polymer is not admitted to the multilamellar lipid phase [119]. **[FIGURE 9]**

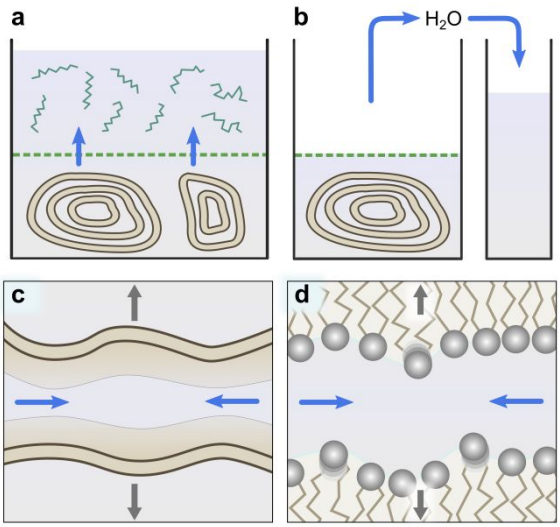

FIGURE 9. Illustration of methods to apply pressure to a lipid membrane system and forces acting at different interbilayer separations. Two techniques allow control of water activity for lipid membranes in the liquid-crystalline state: (a) osmotic removal of water from multilamellar lipid membranes due to a stressing polymer solution; and (b) direct dehydration of membrane lipids by gravimetric removal of water. In each case, the dashed line (red) symbolizes the thermodynamic Gibbs dividing surface between the two phases. Various forces affect the osmotic coefficient including: (c) intermediate-range interactions whereby steric repulsions due to thermal undulations enable water uptake; and (d) short-range interactions where molecular protrusions and/or hydration forces cause steric repulsion. The osmotic coefficient of water is related to its chemical potential thereby allowing the bilayer work to be measured quantitatively. Undulatory forces together with short-range protrusive forces affect the stability of bilayer membrane assembly at different pressure regimes, which are probed with solid-state NMR spectroscopy. **[85% of single-column width]**

For lipid membranes that are freely suspended as multilamellar dispersions, the stressing polymer solution (osmolyte phase) does reversible work on the lipid phase by removing water, giving rise to the external osmotic pressure. In the osmolyte phase, the added (osmotic) pressure increases the chemical potential of water in the stressing polymer solution, so that it equals the solvent chemical potential in the lipid phase. Deformation of the lipids occurs by changing the water volume, with temperature and pressure held constant. We can then consider the thermodynamic relation $\left(\partial\mu_{\rm W}/\partial P\right)_T = \overline{V}_{\rm W}$ where $\overline{V}_{\rm W}$ is the partial molar volume of water in the osmolyte phase. Upon integration, assuming the partial molar volume of water is constant, for the osmolyte phase we obtain that $\mu_{\rm W} = \Pi\overline{V}_{\rm W}$ where Π is the osmotic pressure. Here we use the symbol P to denote a generic pressure, and Π to designate the osmotic pressure. The reference for both the osmolyte and lipid phases is bulk water with $\mu_{\rm W}^*$ as its chemical potential. In what follows, the osmotic pressure Π is set either by a polymer solution in large excess, or by gravimetric removal of water. See Figs. 9(a) and 9(b) for a cartoon illustration.

6.2. Work Content and Helmholtz Free Energy

In terms of equilibrium thermodynamics, for the multilamellar lipid phase, the total differential of the Helmholtz free energy (F) reads [219]

$$dF = -P\,dV - S\,dT + \sum_k \mu_k dn_k \qquad , (44)$$

where F is an extensive thermodynamic state variable. Here S is the entropy, T is the temperature, and the chemical potentials are defined by $\mu_k = \left(\partial F/\partial n_k\right)_{T,\,V,\,n_{j\neq k}}$, where n_k represents the number of moles of the kth component. The first two terms on the right correspond to a closed system, where $\left(\partial F/\partial V\right)_{T,\,n_k} = -P$ and $\left(\partial F/\partial T\right)_{V,\,n_k} = -S$. The summation includes the change due to the mass transfer of dn_k moles of the kth component with chemical potential μ_k for an open system.

Reversible Work Corresponds to Deforming the Membrane Unit Cell—The volume of the lipid phase is measured by the size of the unit cell (Fig. 2), and can change in two different ways: either by compression/expansion at a constant number of waters ($N_{\rm W}$) under changing external pressure, or by changing $N_{\rm W}$

(removal or addition of water molecules) at constant pressure. In the osmotic stress method, for the range of pressures used, we assume that both the lipids and water are practically incompressible—hence the partial lipid and water volumes remain unchanged. We consider changes in free energy as only due to changes in N_W and neglect compressibility effects. The reversible work does not involve compression for either the lipid or water (compressibility $\kappa \approx 0$). That is to say, only a mass transfer of water is involved, with the osmotic pressure held constant. Changes in either Gibbs or Helmholtz free energies holding their natural variables (T and P, or T and V, respectively) constant are the same. They both depend on the chemical potential μ_W of the aqueous solvent (formulated in terms of either Gibbs or Helmholtz free energies), together with the moles of water transferred across the thermodynamic dividing surface.

Removal or Addition of Water Yields Structural Remodeling of the Lipid Bilayer—Now for a given composition, if we hold the volume of the lipid phase and the temperature constant ($dV = dT = 0$), then the total differential of the free energy, Eq. (44), is simplified accordingly. Identifying F as the Helmholtz free energy per lipid molecule, and n_W as the moles of associated waters, the total differential becomes:

$$dF = \mu_W \, dn_W \qquad (45)$$

Conservation of energy (first law of thermodynamics) implies that the reversible work $\mu_W \, dn_W$ done on the lipid phase is equal yet opposite to the work $-\mu_W \, dn_W$ done by the osmolyte phase. Substituting $\mu_W = \Pi \overline{V}_W$ for the osmolyte phase, we find that:

$$dF = -\Pi dV_W \qquad (46)$$

Here we have formulated the water volume per lipid as

$$V_W = \overline{V}_W \, n_W = \upsilon_W \, N_W \qquad (47)$$

where $\upsilon_W = \overline{V}_W / N_A$ is the (partial) molecular volume of water, N_A is the Avogadro constant, and N_W is the number of waters per lipid molecule in the unit cell. Typically, it is assumed that the partial molar volume $\overline{V}_W \approx$ the water molar volume $\overline{V}_W^*$ and that it remains ≈ constant. Because the volumetric reduction of the lipid phase occurs in the same direction as the external osmotic pressure, the reversible work is positive.

According to Eq. (46), the reversible work (Helmholtz free energy) of deforming the lipid phase—due to changing the bilayer separation plus any structural deformation of the membrane—corresponds to the directly measured work of removal of water. The positive work originates because the sign of dn_W is negative for the movement of water from the lipid phase to the osmolyte phase. The transfer of water can be accomplished either osmotically, or by gravimetric control. As noted above, the mass transfer of water from the lipid bilayer occurs by equilibration of the lipid phase with a stressing polymer solution. Alternatively, for gravimetric removal of water, [26, 71] the interface between the lipid phase and air plays the role of a thermodynamic dividing surface, corresponding to the semi-permeable membrane of an osmometer.

6.3. Free Energy of Lipid Membrane Deformation

What is more, by introducing the area per lipid $\langle A \rangle$ and the water thickness $D_{W/2}$ as lattice variables [24] (see Fig. 2), the total differential of the Helmholtz free energy can be written as:

$$dF = \left(\frac{\partial F}{\partial \langle A \rangle}\right)_{D_{W/2}} d\langle A \rangle + \left(\frac{\partial F}{\partial D_{W/2}}\right)_{\langle A \rangle} dD_{W/2} \qquad (48)$$

For the lipid phase, the free energy depends only on the area per lipid $\langle A \rangle$ and $D_{W/2}$, which is the interlamellar water distance. We can thus express the water volume for a geometrical prism (Fig. 2), giving $V_W = \langle A \rangle D_{W/2}$ as the result. Upon differentiation, and combining with Eq. (46), we then find that:

$$dF = -\Pi D_{W/2} \, d\langle A \rangle - \Pi \langle A \rangle \, dD_{W/2} \qquad (49)$$

Here we recall that the osmotic pressure $\Pi \approx$ constant, due to a large excess of the stressing polymer solution, or stemming from gravimetric removal of water.

Total Differential of the Free Energy Includes Both Area and Thickness Deformation—From the above total differential, we obtain the following thermodynamic relations [71, 118]:

$$\left(\frac{\partial F}{\partial \langle A \rangle}\right)_{D_{W/2}} = -\Pi D_{W/2} = \gamma \qquad (50)$$

and

$$\left(\frac{\partial F}{\partial D_{W/2}}\right)_{\langle A \rangle} = -\Pi \langle A \rangle = -F_R \qquad (51)$$

The first result, Eq. (50), tells us that the change in free energy with respect to the interfacial area $\langle A \rangle$ per lipid [24] corresponds to the surface tension γ acting on a lipid molecule in a bilayer. The second formula, Eq. (51), teaches us the change in free energy per lipid molecule with a change in the bilayer separation gives the force acting on a lipid perpendicular to the bilayer surface (along

the bilayer normal). Note that as the bilayer separation decreases ($dD_{W/2}$ negative), the reduction in the area per lipid ($d\langle A\rangle$ negative) is unfavorable (dF positive). Work is thereby done by the stressing polymer solution on the lipid phase.

Energetics of Bilayer Remodeling are Divided Between Area and Separation Work—Our next question is: How much of this work goes into the bilayer separation, and how much goes into bilayer deformation? We now split the effect of osmotic pressure into the influences of separation forces, and the surface tension (which equals zero for a bilayer at equilibrium with excess water). Here we use the definition of the surface tension [220] to obtain $\gamma = -\Pi D_{W/2}$ in Eq. (50). Clearly the surface tension for a lipid bilayer is a function of the area per lipid molecule. Because γ corresponds to a negative pressure, it costs work to condense the bilayer, thus giving an increase in free energy. If we define the repulsive pressure as $P_R = F_R/\langle A\rangle$, then $\Pi = P_R$ in accord with Eq. (51). The osmotic pressure Π is a positive quantity, due to the repulsive force in Eq. (51), which implies there is a tendency for the multilamellar lipids to expand indefinitely. Still, at some point the swelling due to repulsion is counterbalanced by the long-range attractive force, [24] which is attributed to van der Waals interactions.

We can then calculate the fraction of work that goes into reducing the bilayer separation and the area deformation. The ratio of separation work to area work (x) is defined as [71]:

$$x = \frac{\text{separation work}}{\text{area work}} = \frac{\left(\frac{\partial F}{\partial D_{W/2}}\right)_{\langle A\rangle} dD_{W/2}}{\left(\frac{\partial F}{\partial \langle A\rangle}\right)_{D_{W/2}} d\langle A\rangle} \qquad .(52)$$

Eqs. (50) and (51) can be used to simplify Eq. (52), yielding:

$$x = \frac{-\Pi\langle A\rangle\, dD_{W/2}}{-\Pi D_{W/2}\, d\langle A\rangle} = \frac{d\ln D_{W/2}}{d\ln\langle A\rangle} \qquad .(53)$$

In terms of the fraction of area work (θ), the above result corresponds to the relation:

$$\theta = 1/(1+x) \qquad .(54)$$

The area work allows us to calculate the percentage of energy that goes into deforming the lipid membrane, as opposed to reducing the interbilayer distance. Note that Eqs. (47) and (48) do not contain the fraction of area work, because the partial derivatives yield separate contributions from $\langle A\rangle$ and $D_{W/2}$ as the two lattice variables.

7. Flexibility and Elasticity of Membrane Bilayers Under Hydration Stress

We can now ask the question: How are the membrane structural properties accessed through the various alternative biophysical techniques? In this section, we give emphasis to the study of membrane deformation due to osmotic stress, using different experimental tools. The results of solid-state ^{2}H NMR spectroscopy are compared to previous X-ray scattering studies with the Luzzati method [76, 158, 221], as well as the electron density profile approach [214]. While small-angle scattering (both X-ray and neutron) are the methods of choice for determining membrane structure along the bilayer normal (such as head-to-head distance and bilayer thickness), the errors in lateral parameters such as the area per lipid can be quite large. This is because the scattering methods are highly sensitive to large-scale membrane undulations. [222, 223] More accurate results are obtained using analytical methods that combine MD simulations and/or use special sample geometries in controlled humidity chambers, which provide measurements of material parameters such as the bending rigidity. In contrast, solid-state NMR yields accurate and detailed measurements of individual order parameters for each carbon segment in the sample, giving a larger set of data for structural determination. Additionally, the membrane bending rigidity is accessible by supplementing order parameter data with relaxation measurements [42].

It is noteworthy that solid-state NMR studies of membrane lipids enable deformation to be probed at a site-resolved or atomistically specific level (Fig. 4), allowing the emergence of bilayer material properties to be investigated. Such parameters can be important for the energetics of membrane lipid-protein interactions, as described by a flexible surface model (FSM) [8, 43, 224]. In terms of equilibrium properties, the mean-torque description of lipid forces can be applied with osmotic stress methods that quantify bilayer elasticity and deformation [225]. Using our approach, the statistical mechanics of chain conformations describe the lipid confinement within the bilayer geometry. In experiments that connect to atomistic-level interactions, bilayer deformation occurs in response to external forces underlying the osmotic or hydrostatic pressure. Lipid membranes are nearly volumetrically incompressible materials [162], yet they undergo a significant diminution of the area per lipid (up to 20%) when exposed to osmotic pressures in the range of 0–200 atm [26]. This

reduction is compensated by an opposite increase in volumetric thickness, yielding a pronounced anisotropic deformation, as described by Young's modulus and the Poisson ratio (e.g., the thickness can increase by as much as the projected length of 3–4 methylene segments) [26]. Furthermore, the intermolecular interactions are significantly anharmonic—lipid bilayers can sustain lateral compression to a far greater degree than expansion (the lysis limit is only ≈ 3–5%).

7.1. Dehydration and Osmotic Pressure Methods for Determining Membrane Properties

Because the activities of membrane proteins underlie many key cellular functions, the lipid bilayer matrix often tends to be overlooked or neglected. In spite of that, recent insights point to an important role of the soft membrane matter, including both lipids and water [1, 47]. Establishing the proper initial values and boundary conditions is essential to validating molecular simulation outcomes. Here the area per lipid gives a quantitative measure for connecting the average membrane structure to protein-mediated functions of biomembranes. It is tied to elasticity parameters like the area elastic modulus K_A, and the area per lipid [24, 159], which are central to molecular simulations of biomembranes [226, 227] and lipid bilayers [24, 32, 35, 60, 72, 228, 229]. (Analogous curvature elasticity parameters are the Helfrich spontaneous curvature H_0 and the associated bending rigidity K_C). If we adopt the area per lipid $\langle A \rangle$ at the bilayer interface with water [24] as a structural measure [26], the question then becomes: Do membrane lipid bilayers deform appreciably [71, 100, 158] or not [214] in response to osmotic pressures in the biological range?

This question might appear as a simple, until one realizes that lipid structural parameters are rather difficult to obtain from experimental data [60]. Indeed X-ray [230] and neutron scattering [2] are often viewed as cornerstones for accessing positional correlations at the molecular and atomic levels. For lipid bilayers in the fluid state, however, the scattering peaks are broadened, or even suppressed by pronounced membrane shape fluctuations [25]. As John Nagle et al. [25, 76, 214, 231] have insightfully discussed, a loss of resolution in the reconstructed electron density profiles occurs. Under certain conditions [231], the reconstructed electron densities appear insensitive to applied osmotic stress. However, detailed consideration of structural data entails fluctuation corrections indicative of strong deformation over the whole range of osmotic pressures [232]. In addition, a scattering method (due to Luzzati [161]) that does not use electron densities—and instead relies on accurate (gravimetric) measurement of water content [233]—has shown a limited range of deformation at high osmotic pressures. Yet the question of sample inhomogeneity has bedeviled this particular method [100]. Consequently knowledge of how lipid bilayer remodeling occurs in response to external stresses is still rudimentary.

Lipid Bilayer Deformation Under Osmotic Stress Entails a Gibbs Dividing Surface—In fact, the extent to which lipid bilayers deform under external stress [71, 100, 111, 158] has long been controversial. As water is removed from the interlamellar space, how much of the work goes into reducing the membrane separation, and how much goes into lipid bilayer deformation? The question has persisted since the early work of Luzzati [155], and more recently Parsegian and Rand [50]. Partly in consequence, two schools of thought currently exist regarding the bilayer deformations induced when multilamellar lipid vesicles are subjected to osmotic stress. Either the bilayer deforms or it does not—that is the question. What is more, for proteolipid membranes, the lipid bilayer structural adaptations can change the hydrophobic matching at the intramembranous protein surface; there is ample free energy to alter the protein conformational equilibria [43, 234]. The question of bilayer deformation then becomes relevant to lipid-protein interactions, wherein an energetic penalty is incurred by hydrophobic mismatch between the lipid bilayer and the hydrophobic protein surface [19, 43, 234-237].

Let us now come back to the situation in Fig. 9(a), where a dividing surface—either virtual or real, as indicated by the dashed line—separates a polymer solution in equilibrium with the multilamellar lipid phase. Such an arrangement can be achieved by introducing a semi-permeable barrier, such as a dialysis membrane. Alternatively, as first recognized by Parsegian and Rand, [218] one can simply choose a polymer of sufficient size, which is excluded from the space between the lipid membranes by the unfavorable entropy loss. Because the osmolyte and lipid components are isolated and do not mix, there is a virtual dividing barrier (Gibbs dividing surface) that bisects the thermodynamic phases, as shown in Fig. 9(a). One can thus approximate the ternary system as two binary systems that interact solely through the osmotic pressure. The first binary system is the lipid-water system, and the second is the osmolyte-water system. The two binary systems compete for water, defined as the common reference phase—hence we consider the osmotic pressure of each system separately. At equilibrium, their osmotic pressures become

equivalent.

7.2. Deuterium NMR Spectroscopy as a Secondary Osmometer for Lipid Bilayers

Surprisingly large changes occur in the solid-state ^{2}H NMR spectra and derived order profiles for lipid membranes in the liquid-crystalline state [26] due to applied pressure, as shown in Fig. 10. At left the ^{2}H NMR spectra are shown for freely suspended multilamellar dispersions of the representative phospholipid DMPC-d_{54} in the liquid-crystalline state under different conditions of pressure, and at right the matching order parameter profiles are plotted. In Fig. 10(a), at the left, the deconvoluted (so-called de-Paked) ^{2}H NMR spectra are for gravimetrically prepared DMPC-d_{54} samples, where the water-to-lipid mass ratio is varied in a controlled way. Inspection of the spectral peak positions demonstrates that removal of water stresses the membrane, as shown by an increase in the residual quadrupolar splittings (RQCs) of the acyl chain resonances. Correspondingly striking changes in the ^{2}H NMR spectra are seen when the water activity is controlled by exposure to stressing polymer solutions containing polyethyleneglycol (PEG) of molar mass M_r 1500 (PEG 1500). As first shown by Mallikarjunaiah et al. [26], one can use the NMR instrument as a secondary osmometer to establish the equivalence of the osmotic pressure results with gravimetric dehydration pressure data [101, 238]. Next Fig. 10(b) at the left shows the de-Paked ^{2}H NMR spectra of the liquid-crystalline DMPC-d_{54} samples with various PEG 1500 mass ratios. Clearly, there is an striking increase in the RQCs as the concentration of osmolyte, or equivalently osmotic pressure, changes from 0% PEG 1500 ($N_W >$ 30) to 87.6% PEG 1500 ($N_W \approx 1.3$). Additional comparison to the results of applying hydrostatic pressure is provided in Fig. 10(c), which yields much smaller changes in the RQCs and the derived order profiles. The influences of hydrostatic pressure on bilayer deformation are discussed in further detail below. **[FIGURE 10]**

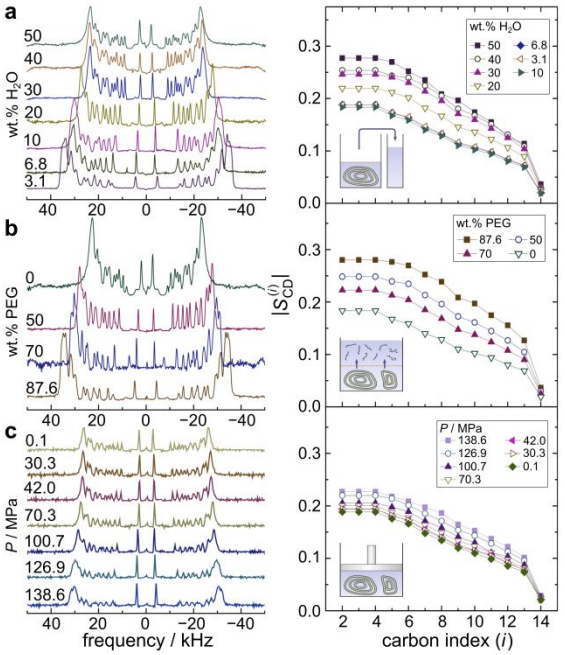

Figure 10. Solid-state ^{2}H NMR spectroscopy and derived order profiles reveal striking changes in lipid membrane structure in the liquid-crystalline (ld) state due to applied external pressure: (a) gravimetric water control, (b) osmotic stress caused by polyethylene glycol (PEG) solutions, and (c) hydrostatic pressure. Bilayer deformation under the three methods of applying pressure establishes the anisotropic response of the material. Examples are shown of deconvoluted (de-Paked) ^{2}H NMR spectra (left) for unoriented multilamellar dispersions of DMPC-d_{54} in the liquid-crystalline state at 45 °C (for $\theta = 0°$ orientation of bilayer normal to external magnetic field direction) and corresponding segmental bond order parameter profiles (right). Numerical labels indicate (a) the weight percentage of water, (b) the concentration of osmolyte PEG 1500 (polyethyleneglycol with molar mass M_r=1500), and (c) the values of bulk hydrostatic pressure applied to the bilayer membrane system. Figure adapted from Ref [26] with permission. Variation of segmental carbon-deuterium bond order parameters is due to removal of water from the interlamellar space. Note that more pronounced changes are observed in case of osmotic and dehydration pressures as compared to hydrostatic pressure. **[100% of single-column width]**

In Figs. 10(a) and 10(b), at the right, the segmental order parameter profiles are directly compared for DMPC-d_{54} as a function of gravimetric dehydration or osmotic stress. For phospholipids in the liquid-crystalline (liquid-disordered, ld) state, the segmental order parameters decrease from the upper acyl chain plateau position (C2–C4 carbons) to the terminus at the C14 carbon [239]. The orientational constraint implicit in the segmental order parameter characterizes how the polar head groups effectively tether the lipids to the aqueous interface. The plateau

is due to the ~constant packing of the lipid chains, where their extension (travel) away from the aqueous interface is favored by correlations among various rotational isomeric states (e.g., *trans*, *gauche*$^+$, *gauche*$^-$). Towards the central region of the bilayer, there is a drop in the segmental order parameters due to the effects of chain terminations; see Fig. 6(a) for a cartoon depiction. Because the chain ends are statistically distributed, greater disorder of the surrounding groups fills in the free volume that would otherwise be present in the bilayer core. Consequently, the hydrocarbon density is maintained close to liquid hydrocarbon [115]. Formulated as a potential of mean force, the orientational potential energy is greatest for the top part of the chains, near the aqueous interface. The hydrocarbon interior of the membrane experiences the weakest ordering potential of the liquid-crystalline membrane.

Dehydration Pressure and Osmotic Pressure Have an Underlying Thermodynamic Correspondence—Based on the solid-state ^{2}H NMR order parameters shown at the right of Figs. 10(a) and 10(b), our findings demonstrate both theoretically and experimentally that significant bilayer deformation occurs with osmotic pressures in the range ≈10–100 atm (1–10 MPa)—values well within the biological range [26]. The data clearly prove-that significant changes in dynamical structure occur as a function of osmotic stress [26]. For DMPC-d_{54} in Figs. 10(a) and 10(b) the results [26] indicate that ^{2}H NMR spectroscopy can establish the connection between the dehydration pressure and osmotic pressure. Comparison of the segmental order profiles for DMPC-d_{54} with PEG 1500 as the osmolyte to the values when it is gravimetrically dehydrated proves the two approaches correspond thermodynamically, as shown by Figs. 9(a)–(b). Removal of H_2O by either mechanism leads to an analogous variation of the segmental order parameters [26].

Further evaluation of the structural properties of lipid bilayers under osmotic stress is afforded by using the mean-torque model. With the above formalism, the average cross-sectional area per lipid $\langle A \rangle$, bilayer thickness $D_B = 2D_C + 2D_H$, and water spacing D_W can be determined [26]. The cross-sectional area per lipid decreases from the fully hydrated value of 60.2 Å^2 ($N_W \approx 20$) to 50.2 Å^2 ($N_W \approx 1.5$) at 30 °C as the effective osmotic pressure is increased, i.e., for both the gravimetrically dehydrated and osmolyte samples. Overall, the area deformation is $\Delta\langle A \rangle = 10$ Å^2, and represents a 17% contraction within the plane of the lipid membrane. (We note the absolute area compression is greater than the area increase near the lysis limit, confirming the bilayer deformation is significantly anharmonic.) Likewise, there is a substantial change in the corresponding bilayer thickness. The volumetric bilayer thickness D_B varies between 43.6 Å ($N_W \approx 20$) to 48.8 Å ($N_W \approx 1.5$), assuming a head group layer thickness of $D_H = 9$ Å. As a result, the bilayer deformation is $\Delta D_B = 5.2$ Å, giving a 20% extension of the hydrocarbon thickness $2D_C$ with clear implications for hydrophobic matching to membrane proteins. A corresponding reduction of the interlamellar water from $N_W = 20$ to $N_W = 1.5$ changes D_W from 20.1 Å to 1.8 Å, respectively. For the fully hydrated reference state, the D spacing is 63.7 Å, so the structural change represents a 20% contraction in lamellar thickness. Hence appreciable structural remodeling of lipid bilayers can occur due to osmotic stress.

Bilayer Deformation is Induced by Either Osmotic or Hydrostatic Pressure—Use of NMR spectroscopy as a secondary osmometer gives a basis for comparison to the effects of hydrostatic pressure on bilayer deformation, as studied by Morrow et al. [101], see Fig. 10(c). While the physical mode of action of the two stressors is clearly different, their effects on membrane structure are comparable. Osmotic stress relies on differences in water affinities between lipids and osmolytes. Therefore, one can remove water from the lipid phase with an appropriate concentration of osmolyte. Yet the action of hydrostatic pressure in deforming the bilayer is less obvious. As measured by ^{2}H NMR, comparable bilayer deformations occur at much larger values of the hydrostatic pressure than for osmotic pressure. That is because osmotic removal of water is more efficient than when it is caused by material anisotropy [101]. Because lipid membranes are highly anisotropic [24], they deform unequally along the membrane normal and in the membrane plane, even under the action of isotropic hydrostatic pressure. Besides Young's modulus the Poisson ratio is involved (see below). (An isotropic and homogeneous material will compress uniformly under bulk hydrostatic pressure, while for an anisotropic material the deformation is characterized both by Young's modulus and the Poisson ratio.) Consequently, hydrostatic pressure can either pull water away from the lipid head groups (similar to an osmotic effect), or push water deeper into the membrane (opposite to an osmotic effect). The membrane thickness increases under the action of hydrostatic pressure (the acyl chains become more ordered), which suggests that lipid hydration is reduced. Other scenarios are possible, because at high pressure one has to consider all changes in molecular volumes

(including water), as White et al. [240-242] have discussed.

In the way shown above, the NMR order parameters can connect the influences of osmotic pressure to an equivalent dehydration state [26]. We have proposed that there is a unified interpretation of all three pressure-based methods of lipid bilayer structural perturbation [26]. Here the ^{2}H NMR order parameters give us the key to unlocking the effects of pressure on lipid membranes. We recall that a larger value of S_{CD} indicates a greater bilayer thickness, with a corresponding area reduction, and conversely. It is often said there is no a priori relation between the effects of osmotic pressure [26, 100] and hydrostatic pressure [101] (the former pertains to an open system, the latter to a closed system). However, solid-state ^{2}H NMR shows that osmotic pressure amounts to an equivalent hydrostatic pressure in terms of changes in hydration. Calibrating the order parameters versus the osmotic pressure of the stressing polymer solutions, we are able to use ^{2}H NMR spectroscopy to establish the correspondence of the pressure-based measurements, as shown by Mallikarjunaiah et al [26]. We are thus able to establish how the deformation by either osmotic or hydrostatic pressure amounts to different hydration states of the membrane lipid bilayer.

7.3. Universality of Hydrostatic and Osmotic Pressure in Membrane Deformation— Poisson Ratio

The effects of osmotic and dehydration pressures come into greater synergy through matching the experimental order parameters [225]. Both types of perturbation yield approximately the same order parameters over the entire pressure range. Nevertheless, the influence of hydrostatic pressure is clearly different. Significant bilayer deformation occurs only at high values (≈100–1000 atm), see Fig. 10(c). From the order parameters, we can establish the connection of hydrostatic pressure to osmotic pressure for systems where the number of waters per lipid is known. Let us next consider a model membrane composed of a single lipid type under the action of an external physical field, such as osmotic or hydrostatic pressure. Experimentally, it is observed that the area per lipid molecule at the aqueous interface changes. In the case of osmotic pressure, the presence of a Gibbs dividing surface (Fig. 9) implies the pressure field acing on the lipids is anisotropic. It affects hydration, and thereby the interactions between lipid head groups (plus the acyl chain segments close to the lipid-water interface).

But how do we explain the changes in the area per lipid due to hydrostatic pressure? Here the deformation along a particular direction in space occurs under the influence of an *isotropic* external field. The answer must rely on *material anisotropy* [243]. By their nature, in membrane liquid crystals the lipid interactions are anisotropic, because of the chemical composition and geometry. Differences in compressibility along the bilayer normal and in the membrane plane are generally described by the Poisson ratio. Three-dimensional bulk compressibility is insufficient to describe lipid membranes, as it fails to account for differential changes in the area per lipid and bilayer thickness. Material anisotropy explains why the area per lipid is expected to change, not only under osmotic pressure, but also under isotropic hydrostatic pressure. This viewpoint is informative in theoretical studies of lipid-protein interactions, and also in setting up and testing atomistic MD simulations.

Pressure-Based Methods for Investigating Lipid Deformation are Unified by the Poisson Ratio—Accordingly, for the case of multilamellar lipid dispersions in the liquid-crystalline state, Fig. 11 teaches us how their deformation using force-based approaches can be explained using the Poisson ratio [244]. Plots of the segmental C–^{2}H order parameters for the plateau acyl chain segments of the DMPC-d_{54} bilayer in the liquid-crystalline (L_α) state are shown for the three different ways of applying external pressure (Fig. 11). Values of the ^{2}H NMR plateau order parameters are graphed versus hydrostatic pressure, as well as osmotic and dehydration pressures. The inset shows the order parameters as a function of the actual pressure values. But most striking, Fig. 11 shows that by using the order parameters for the plateau acyl chain segments S_{CD}^{plat} to scale the pressures, we can collapse all the results to a universal curve. The results are nearly superimposable—irrespective of whether the structural changes involve gravimetric dehydration, osmotic pressure, or hydrostatic pressure [26]. A common set of elastic constants (Young's modulus and the Poisson ratio) explains the bilayer deformation (strain) induced by an external force (stress) in all three cases [26]. In this way, solid-state ^{2}H NMR spectroscopy unifies the structural results for the various pressure-based measures of bilayer deformation. **[FIGURE 11]**

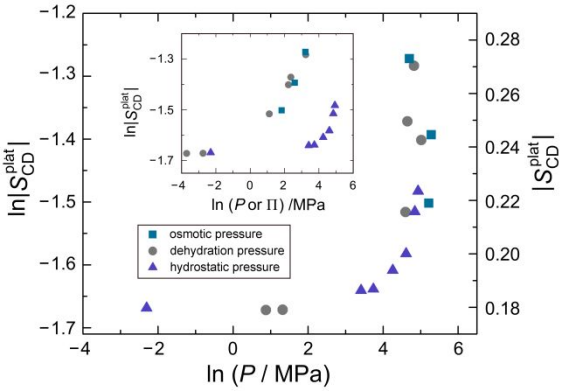

Figure 11. Carbon-deuterium bond S_{CD} order parameters from solid-state ^{2}H NMR spectroscopy compare various pressure-based measures of lipid bilayer deformation. Data are for freely suspended multilamellar dispersions DMPC-d_{54} lipids in the liquid-crystalline (L_α) state at 45 ºC. The ^{2}H NMR order parameter (plateau) $|S_{CD}^{plat}|$ values are plotted against pressure P applied in three different ways: (triangles) hydrostatic pressure, (squares) osmotic pressure, and (circles) dehydration pressure. Experimental order parameters are used to establish the correspondence (see Refs [26] for details). Inset: comparison of the same data showing order parameters versus osmotic or dehydration pressure (Π) or bulk hydrostatic pressure (P). Using ^{2}H NMR spectroscopy as a secondary osmometer various pressure-based measurements collapse to a universal curve. Data are from Ref [26]. **[85% of single-column width]**

7.4. Bilayer Deformation Induced by Osmotic Stress

Clearly, the aqueous solvent is expected to behave nonideally in both the multilamellar lipid phase and the osmolyte stressing polymer solution (Fig. 9). According to classical thermodynamics [245], deviations from ideality are expressed in terms of an activity coefficient for the aqueous solvent. For the two phases in thermodynamic equilibrium, the common reference state is pure water, with μ_W^* as the chemical potential. In a binary solution with water as the solvent, the chemical potential μ_W is related to its activity a_W by $\mu_W = \mu_W^* + RT\ln a_W$. In addition, the solvent activity is related to its vapor pressure by $a_W = \gamma_W X_W$, where γ_W is the activity coefficient and $X_W = P_W/P_W^*$ is given by Raoult's law. On the other hand, experimental measurements of the solvent vapor pressure P_W for multilamellar lipids are fraught with difficulty [60, 76, 119]. For lipid dispersions under osmotic stress, we require very accurate vapor pressure measurements, [71] with the complication of a vapor pressure paradox [100, 232, 246, 247] that has bedeviled investigators. Evidently, it is challenging to apply vapor pressure osmometry to directly measure the aqueous solvent activity of both the osmolyte phase and the multilamellar lipid phase over the full range of interest.

Nonideal Solvent Water Corresponds to Attractive and Repulsive Interactions in Polymer Solutions—For an ideal solution, it is well known the osmotic pressure is given by the van't Hoff equation,

$$\Pi = RT\,(n/V) \qquad ,(55)$$

where (n/V) is the molar concentration of the polymer solute. By introducing a virial expansion of the solvent chemical potential expressed using the solute concentration, the case of a nonideal solution can also be treated, such that Raoult's law is preserved at infinite dilution. The resulting virial equation of state for the osmotic pressure is given by

$$\Pi = RT\left[\left(\frac{n}{V}\right) + B'\left(\frac{n}{V}\right)^2 + \ldots\right] \qquad ,(56)$$

in which the leading term represents an ideal solution, and B' is the second virial coefficient. The solute activity coefficient is absorbed into the virial coefficients that describe the nonideality.

Moreover, for various stressing polymer solutions, Parsegian et al. have discovered the osmotic pressure Π obeys the following universal equation of state [248]:

$$\Pi = \frac{RT}{M_m \bar{v}_P N^{9/5}}\left[\left(\frac{C}{C_N^*}\right) + \alpha\left(\frac{C}{C_N^*}\right)^{9/4}\right] \qquad .(57)$$

Here C is the polymer mass concentration (typically in grams per mL), M_m is the molar mass per monomer, $\bar{v}_P$ is the partial specific volume of the polymer, N is the number of monomers in a polymer chain, and $C_N^* \equiv 1/\bar{v}_P N^{4/5}$ is related to the N-dependent scaled polymer concentration [248]. The first term on the right corresponds to the asymptotic van't Hoff limit, Eq. (55), appropriate to the dilute regime. The second term represents the asymptotic des Cloizeaux limit [249] for the osmotic pressure in the semi-dilute regime, where the polymer chains interpenetrate [250]. Lastly α is an adjustable parameter for the crossover between the two limits [249]. According to the above scaling law, Eq. (57), the osmotic pressure of a polymer solution depends on the monomer concentration, but not the chain length or polymer concentration (i.e., it is independent of the molar mass of the polymer) [250]. In principle, the above analytical formula [248] allows us to extrapolate the osmotic pressure beyond the experimentally accessible range, or to interpolate between observed values. For applying the osmotic stress technique [118] the measured osmotic pressures are used when available, rather than theoretically calculated pressures.

By utilizing experimental osmotic pressure data [50], the nonideality of the stressing polymer solution is included, without explicitly introducing the activity coefficient of the polymer solute [245]. The water activity can then be related to the polymer solute activity by the Gibbs-Duhem equation. Explicit treatment of the nonideality of the stressing polymer solution (osmolyte phase) is thus effectively bypassed [119].

Accordingly, Mallikarjunaiah et al [26] have used ^{2}H NMR spectroscopy as a secondary osmometer that enables one to relate the experimental osmotic pressure Π of the polymer solution to the gravimetrically determined number (N_W) of water molecules per lipid. The idea of using ^{2}H NMR spectroscopy allows the bilayer deformation to be probed directly. We can then divide the work of bilayer deformation into the work of moving the bilayers apart, and the work of changing the average cross-sectional area. When the osmolyte and lipid solutions are in equilibrium, the water vapor pressure of the two phases becomes equal, and the chemical potential of the aqueous solvent in the two phases is the same. However, the interactions giving rise to the nonideal behavior are different in each case.

Behavior of Solvent Water in Multilamellar Lipid Dispersions Involves Intermolecular Forces—Let us now ask the question: How does one treat the nonideality of water in the lipid phase? On account of the repulsive and attractive forces, the water is expected to be highly nonideal—that much is certain. For the lipid phase, the ^{2}H NMR order parameters allow us to relate the osmotic pressure exerted by the stressing polymer solution to the numbers of waters of hydration. One can then connect the osmotic pressure Π to the activity of water in the lipid phase in equilibrium with the stressing polymer solution (Fig. 9). Clearly, the chemical potential of water μ_W in the lipid phase is not the same as the chemical potential μ_W^* of pure water. For the lipid phase, the nonideality of the solvent water is attributed to the intermolecular forces (including hydration forces, together with the repulsive forces acting between the lipid molecules in the bilayer). Solid-state ^{2}H NMR spectroscopy thus joins X-ray diffraction, micropipette deformation, and the surface forces apparatus as an experimental means of investigating bilayer membrane forces [225]. Because the solid-state ^{2}H NMR method is inherently atomistic, i.e., we observe atom-specific segmental order parameters, it acts as a bridge between the microscopic and macroscopic scales giving added significance.

The excess free energy of the multilamellar lipids can be traced back to the deviation of the aqueous solvent from Raoult's law. Knowing the water activity of the lipid phase yields a connection to the osmotic pressure Π of the stressing polymer solution. It allows one to investigate the types and magnitudes of the bilayer forces that govern the lipid self-assembly, as well as interactions with membrane proteins and peptides. Nonideality of the aqueous solvent is of considerable interest [251, 252]. The next question is: How do we connect the nonideality of water in the lipid phase to the nonideality of the polymer osmolyte solution? The answer is that the osmotic coefficient is a measure of the nonideal behavior of water in the lipid phase, as compared to water in the stressing osmolyte phase. Introduction of an osmotic coefficient ϕ describes systems where measurement of the solvent vapor pressure may be challenging, e.g., as in the case of lipid bilayers [26]. By equating the solvent chemical potential μ_w of the two phases in equilibrium, for a multilamellar lipid dispersion, we can relate the nonideality of the aqueous solvent to the bilayer forces. Repulsive interlamellar forces can be investigated, as well as those acting between the lipid molecules in the bilayer.

Osmotic Coefficient Relates Nonideality of Water in Lipid Phases to the Stressing Polymer Solutions—In this regard, we have proposed the following equation of state [26] to describe how the osmotic pressure acting upon the multilamellar lipids is related to the number of water molecules:

$$\Pi = \phi\left(\frac{k_BT}{\upsilon_W}\right)\frac{1}{n_W} = \phi\left(\frac{k_BT}{\upsilon_W}\right)\frac{1}{n_W} \qquad (58)$$

Here $\upsilon_W = V_W/N_A$ is the (partial) water molecular volume (so that $\upsilon_W n_W = V_W N_W$, where N_W is the number of water molecules). With the above equation of state, ϕ is the osmotic coefficient [245], defined in terms of the solvent (water) mole fraction X_w by:

$$\phi = (\mu_W - \mu_W^*)/k_BT \ln X_W \qquad (59)$$

The chemical potentials μ_W^* and μ_W refer to the pure water and the aqueous solvent in the solution, and X_W is the solvent (water) mole fraction in the binary mixture containing either the stressing polymer or the lipids. According to Eq. (59), the limits of the osmotic coefficient are $\phi = 0$, corresponding to pure water ($\mu_W = \mu_W^*$) and $\phi = 1$, representing ideal solvent water. Because $\mu_W = \mu_W^* + k_BT\ln(\gamma_W X_W)$ for the solvent in a Raoult's law solution, the osmotic coefficient ϕ is related to the activity coefficient γ_W through the equation $\gamma_W = X_W^{\phi-1}$. Significantly,

the above equation of state, Eq. (58), has been tested empirically, [26] and the applied osmotic pressure Π is found to scale with $1/N_W \sim 1/n_W$ for the lipid systems studied (see below).

In Eq. (58), the osmotic coefficient ϕ is a measure of the nonideality of the aqueous solvent, where $\phi = 1$ represents the limit for ideal osmolytes, with purely colligative behavior. According to Eqs. (47) and (51), we can solve for the osmotic coefficient, and then rewrite Eq. (58) to read:

$$\phi = \frac{\Pi \upsilon_W n_W}{k_B T} = \frac{P_R V_W}{k_B T} = \frac{F_R D_{W/2}}{k_B T} \qquad (60)$$

We now can see that the osmotic coefficient is just the ratio of the separation work to the thermal energy. For completely disassociated molecules, the kinetic energy corresponds to their translational motions. Unless a restoring pressure is applied, the molecules tend to move apart, e.g., to counter the repulsion (e.g., due to the osmotic pressure). Hence the ratio given by the osmotic coefficient is unity. Nonideal interactions due to attractive forces between the solute molecules and the aqueous solvent—for either a polymer solution or multilamellar lipids—lower the osmotic coefficient. Conversely, repulsive forces between the solute and water give a larger osmotic coefficient. We discuss these repulsive forces in further detail below.

Membrane Lipids are Structurally Remodeled by Applying External Pressure—Biological membranes and lipid bilayers in the liquid-crystalline state are known to be laterally compressible [71, 76, 204, 253] materials. Removal of water from the lipid head groups by osmotic stress increases the acyl chain ordering, and reduces the cross-sectional area per lipid; increasing temperature exerts the opposite effect [254]. Previous SAXS studies of osmotic stress together with the Luzzati method [117] have been carried out by Parsegian and Rand [50, 71], as well as Petrache and Nagle et al [114, 166, 221]. These authors have concluded that lipid bilayers deform appreciably with osmotic pressures in the range of 0.5 to 3.0 MPa (5 to 27 atm). Yet, McIntosh et al [111] have concluded from the lipid bilayer electron density profiles that essentially negligible deformation occurs due to osmotic stress. It appears that an alternative method is needed to further distinguish these proposals [26]. Solid-state ^{2}H NMR spectroscopy is unparalleled in this context, because of the highly detailed structural information that it delivers about the hydrocarbon region of phospholipid liquid crystals [8, 42, 157] (Fig. 4).

The next step is to obtain the area compressibility of the lipid film. Here we recall that the surface tension is defined in terms of the Helmholtz free energy as [220]

$$\left(\frac{\partial F}{\partial \langle A \rangle}\right)_{T,\, V,\, n_k} = \gamma \qquad (61)$$

or alternatively $\left(\partial G/\partial \langle A \rangle\right)_{T,P,\, n_k}$ in terms of the Gibbs free energy, where all symbols have their usual meanings. In the absence of osmotic pressure, the lipid bilayer is flaccid—it is not under tension. Hence the area per lipid is at the equilibrium value [24]. We can then write the volume of water associated with the lipid head groups using Eq. (47), which allows us to recast the expression for the surface tension γ in Eq. (50). Substituting the relation $D_{W/2} = \overline{V}_W N_W/\langle A \rangle$ into Eq. (50) thus gives

$$\gamma = -\left(\frac{\overline{V}_W N_W}{\langle A \rangle}\right)\Pi \qquad (62)$$

where $\overline{V}_W$ is the partial molecular volume of water at the bilayer aqueous interface, and Π is the osmotic pressure.

It follows that for a lipid surface film, the area compressibility is defined as [255]

$$C_A \equiv \frac{1}{K_A} \equiv \frac{1}{\langle A \rangle}\left(\frac{\partial \langle A \rangle}{\partial \gamma}\right)_T = \left(\frac{-1}{\overline{V}_W N_W}\right)\left(\frac{\partial \langle A \rangle}{\partial \Pi}\right)_T \qquad (63)$$

where K_A is the area compressibility modulus. Because the osmotic pressure is equal in magnitude on both sides of the interface, this relation applies equally to bilayers. Integrating the above equation over the applied pressure range, we can recast our expression for the interfacial molecular area as a function of osmotic pressure, which reads:

$$\langle A \rangle = -\left(\frac{\overline{V}_W N_W}{K_A}\right)_T \Pi + \langle A \rangle_0 \qquad (64)$$

Here $\langle A \rangle$ and $\langle A \rangle_0$ represent the average interfacial area per lipid [24] at zero osmotic pressure (full hydration) at temperature *T*. Often we can assume that $\overline{V}_W^* = \overline{V}_W$ i.e., the partial molar volume is approximately equal to the molar volume of pure water.

8. Elastic Deformations of Flexible Lipids by External Forces

The above results imply that solid-state ^{2}H NMR spectroscopy is able to characterize the material anisotropy by measuring the area per lipid $\langle A \rangle$ as a function of the applied

pressure (either 2D osmotic or 3D hydrostatic). Significantly, for multilamellar lipids both the 2D bulk compressibility modulus ($K_\perp$) and the area compressibility modulus (K_A) are accessible from hydrostatic or osmotic pressure measurements. As mentioned above, the anisotropic susceptibility of a material to external stress or pressure is quantitatively described by the Poisson ratio [244], which is the ratio between deformations in the membrane plane and deformation along the membrane normal [256-260]. The various moduli describe the shape deformation of a unit cell of the membrane material. For phospholipids, the area elastic modulus can be evaluated from atomistic NMR observables, giving a direct comparison to the results of macroscopic bilayer deformation [7, 261].

8.1. Quantifying Bilayer Deformation at the Atomistic Level by Solid-State NMR Spectroscopy

Accordingly, equilibrium mechanics [243] informs us that the 3D bulk compressibility κ for a deformable material can be divided into its longitudinal ($\kappa_\parallel$) and transverse ($\kappa_\parallel$) components by:

$$\kappa = \kappa_\parallel + \kappa_\perp = -\frac{1}{D_C}\left(\frac{\partial D_C}{\partial P}\right)_T - \frac{1}{\langle A\rangle}\left(\frac{\partial \langle A\rangle}{\partial P}\right)_T \quad ,(65)$$

where P is the bulk hydrostatic pressure. In the above formula, we identify the transverse (area) compressibility as:

$$\kappa_\perp \equiv \frac{1}{K_\perp} = -\frac{1}{\langle A\rangle}\left(\frac{\partial \langle A\rangle}{\partial P}\right)_T = -\left(\frac{\partial \ln\langle A\rangle}{\partial P}\right)_T \quad ,(66)$$

wherein κ is a 2D compressibility (elastic stretch) induced by the 3D bulk pressure. The 2D compressibility is related to the 1D compressibility (extension) $K_\parallel$ via the Poisson ratio (see above). Yet, the application of hydrostatic pressure does not directly remove interlamellar water [101] in contrast to osmotic stress [26, 100]. Hence the two approaches are not directly comparable [26, 218]. It follows that the two area compressibilities $\kappa_\perp$ ($\equiv 1/K_\perp$) and C_A ($\equiv 1/K_A$) differ, because the former does not directly involve the work of removal of water. The chemical potential μ_W is ≈ constant, while the latter is due to removing water from the lipid polar interface.

Biophysical Properties of Membrane Lipids Emerge from Atomistic-Level Interactions—Using solid-state NMR of freely suspended lipid dispersions, the area elastic modulus (K_A) is then obtained over a substantial range of osmotic pressures. Values of the moduli of compressibility [100, 225] or bending rigidity [42, 262] as obtained from the atomistic ^{2}H NMR observables are comparable with those acquired from micro- or nano-mechanics-based methods. Another important aspect is that we can calculate the area elastic modulus K_A over a substantial range of bilayer deformation, obtaining results that agree well with previous estimates [100, 158, 163]. The convincing agreement with the bulk values shows how quasi-elastic behavior of the membrane lipids develops over strikingly short length scales. The results indicate that collective bilayer properties formulated in terms of elasticity begin to emerge on the order of the bilayer thickness, or even less [18].

In Fig. 12 we summarize the remarkable changes in cross-sectional area per lipid that occur for the DMPC bilayer when osmotic pressure [225] is varied. From these data for freely suspended lipid dispersions at temperatures above the order-disorder phase transition temperature, the elastic area compressibility modulus (K_A) value is calculated as 142 ± 30 mJ m^{-2} using the initial slope of the plot. This value is in close agreement with the results obtained independently by Klaus Gawrisch et al. (136 ± 15 mJ m^{-2}) using solid-state ^{2}H NMR spectroscopy, and by Petrache et al. (108 ± 35 mJ m^{-2}) from SAXS measurements [100, 166]. Our experiments cover a much greater range of osmotic pressures, [26] however, and enable the theory to be more accurately tested. By comparing the results from ^{2}H NMR spectroscopy with the material properties obtained from SAXS studies, we are able to investigate how the Hookian elastic behavior begins to emerge from atomistic-level interactions. **[FIGURE 12]**

8.2. Forces Affecting Structure and Dynamics of Lipid Membranes

As set forth above, the language of distribution functions is well suited to membrane lipids in the fluid state, either as freely suspended multilamellar dispersions or as aligned systems on solid supports. The presence of water in fully hydrated bilayers affects the interaction energies, and allows collective fluctuations of the lipids to emerge. For membrane lipids, one expects a continuum of bilayer disturbances, as first discussed [18]. They range from long wavelength 2D undulations and 3D fluctuations down to short length scales, on the order of the segmental dimensions of the flexible lipid molecules [107, 263]. The description of membrane lipids entails broad statistical distributions that include both local disorder, as well as collective fluctuations [24, 60, 264]. Lateral compression by osmotic stress reduces larger length-scale 2D bilayer undulations, together with shorter wavelength 3D quasi-

elastic collective deformations. Additionally, molecular protrusions into the aqueous interlamellar space contribute to the local roughness of the bilayer surface. One must thus investigate various regimes of interbilayer forces. The interactions include entropic repulsions due to undulation forces operate, which dominate the interlamellar pressure at large distances, as well as short-range entropic protrusion forces and hydration forces at shorter distances (below 20 Å).

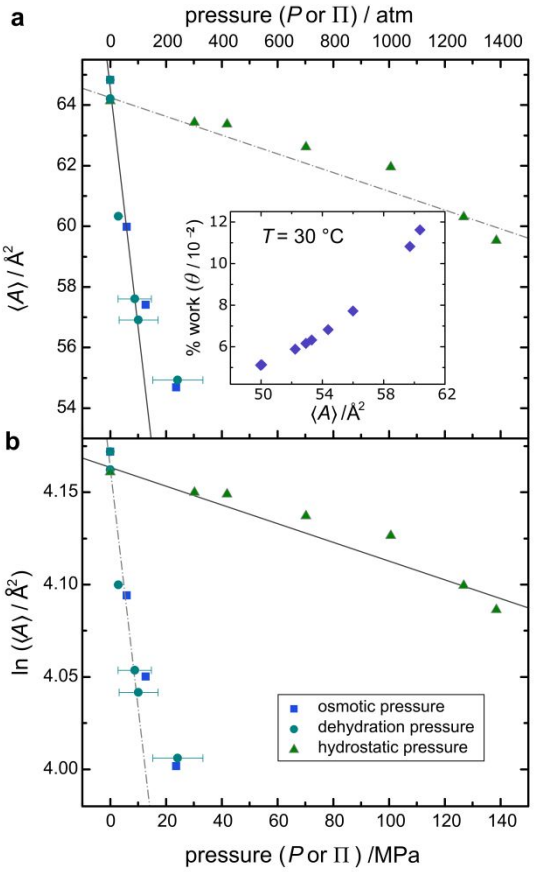

Figure 12. Structural deformation of lipid membranes above the order-disorder phase transition temperature is revealed by the anisotropic response to external pressure. Variation of the cross-sectional area per lipid $\langle A \rangle$ is shown as a function of pressure for multilamellar dispersions of DMPC-d_{54} in the liquid-crystalline phase at 45 °C. The average area per lipid $\langle A \rangle$ is obtained by applying the mean-torque model to solid-state ^{2}H NMR data (cf. text). (a) Plot of $\langle A \rangle$ versus osmotic (squares) or dehydration (circles) pressure. The elastic area compressibility modulus K_A can be calculated from the slope. Analogous plots of $\langle A \rangle$ versus hydrostatic pressure (triangles) yields $K_\perp$ as the 2D bulk compressibility modulus. Inset: Percentage of the area work due to application of osmotic pressure as in Eq. (53) for DMPC-d_{54} (30 °C) obtained with solid-state ^{2}H NMR spectroscopy [225]. (b) Corresponding semi-logarithmic plots of $\langle A \rangle$ versus osmotic (Π) or bulk pressure (P). Data are from Refs [26]. Note the 2D compressibility $\kappa_\perp$ ($\equiv 1/K_\perp$) obtained from hydrostatic pressure data does not directly entail removal of water and differs from the 2D compressibility κ_A ($\equiv 1/K_A$) obtained from osmotic pressure data. Anisotropic deformation of a material under isotropic external stress is described by the Poisson ratio (cf. text). **[90% of single-column width]**

Our strategy is thus to capture information on lipid forces by an experimental parameter (the osmotic coefficient ϕ) that is connected with the non-ideality of the aqueous multilamellar dispersion. According to Eq. (60), the osmotic coefficient quantifies the correspondence of the separation work to the thermal energy. In the liquid-crystalline state, this non-ideality manifests the repulsive and attractive forces acting between the multilamellar lipids, due to their collective fluctuations spanning a broad range of time scales [18]. Measurements of the osmotic coefficient inform us about the types of molecular motions occurring over a range of length scales, giving a new biophysical approach to investigating membrane deformations. Such a combined thermodynamic and structural approach helps to more fully understand the lipid influences on biomembrane functions.

Membrane Lipid Fluctuations Underlie the Non-ideality Described by the Osmotic Coefficient—Empirically, we can determine ϕ by relating the osmotic pressure to the number of waters per lipid in the unit cell using the order parameter profiles of freely suspended multilamellar lipid dispersions [26]. According to Eq. (58), a plot of the osmotic pressure versus $1/N_W$ should yield a linear dependence, as shown in the inset to Fig. 13 for a representative membrane lipid. This plot allows us to obtain the osmotic coefficient ϕ as an experimental observable. The osmotic coefficient arises from non-ideality of the lipid membrane system and depends on physical interactions in the system. Theoretical models have considered various forces to describe the lipid interactions. Those based on the electronic charge distribution include the long-range attractive van der Waals force, and the electric double-layer forces (which are important for charged lipids) [265-267]. Such long-range attractive interactions condense the system, whereas the repulsive interactions of a shorter length range affect the local structure (related to the repulsive pressure by $P_R = F_R/\langle A \rangle$). Here we consider a generalized treatment of the forces among the neutral lipids in biomembranes. **[FIGURE 13]**

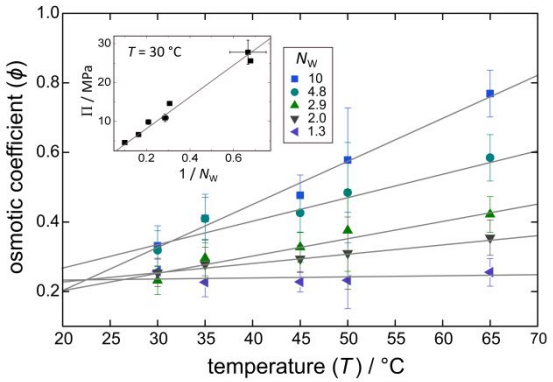

Figure 13. Forces acting on liquid-crystalline membrane bilayers at different separations are captured by the osmotic coefficient (ϕ). Variation of the osmotic coefficient [26] versus temperatures is shown for DMPC-d_{54} multilamellar dispersions in the liquid-crystalline (liquid-disordered, ld) state containing various amounts of water. Values of the water to lipid molar ratio (n_w=$n_{w/L}$=$N_{W/L}$=N_W) are indicated in the figure. The linear temperature dependence of the osmotic coefficient at higher values of $N_{W/L}$ suggests entropic undulation forces as the source of the nonideality [108]. As $N_{W/L}$ decreases the temperature dependence becomes weaker and the data converge around 20 °C, near the melting temperature of fully hydrated DMPC-d_{54} (T_m = 20 °C). The inset shows the osmotic coefficient ϕ versus 1/ $N_{W/L}$ for the multilamellar lipid phase using Eq. (58) [26]. Solid-state ^{2}H NMR spectroscopy gives the variation of the osmotic coefficient (ϕ) at different water content and reveals different regimes of intermembrane forces. **[90% of single-column width]**

Clearly an important question is the length scale over which the continuum mesoscopic properties such as membrane elasticity [42, 262, 268] begin to emerge. In the above treatment of the area elastic modulus, the effects of membrane undulations have been neglected [7, 106, 269]. Their contribution to the projected area that might affect the calculation of membrane lateral compressibility is estimated to be typically small [106], and is primarily manifested at small applied tensions. At larger tensions, the wrinkling of the membrane due to large-wavelength undulations is effectively stretched out. Previous work involving NMR relaxation dispersion studies [18] has indicated the membrane lipids undergo collective order-director fluctuations (ODF) over a broad range of time and distance scales [115]. At shorter lengths, down to the nm scale and below, 3D quasi-elastic fluctuations can occur on the order of the bilayer thickness [42], with a cutoff on the order of the segmental dimensions of the flexible lipid molecules [115]. Additionally, the lipids can undergo 2D collective undulation motions spanning the physical membrane dimensions up to μm distances [18, 115, 135]. Such collective excitations [18, 115] are also manifested in atomistic MD simulations [88, 270]. Non-equilibrium molecular dynamics simulations by Voth et al. [271] are consistent with the above inferences. Molecular models are used to predict material properties in agreement with linear response theory. By considering equilibrium states of the membrane lipids under osmotic stress, one arrives at a similar picture in accord with the fluctuation-dissipation theorem. The properties as studied with solid-state ^{2}H NMR spectroscopy are derived from atomistic-level observables [18], and report on their emergence from the molecular forces and potentials.

8.3. Membrane Fluctuations and Water Uptake Due to Entropic Forces

Lipid membrane systems can be osmotically active because of the significant occurrence of collective lipid motions, such as undulations and order-director fluctuations, together with molecular protrusions. It follows that osmotic stress can be used to explore the associated repulsive forces in terms of the osmotic coefficient ϕ of the membrane lipid dispersion. Information is acquired about the water-mediated membrane interactions in the liquid-crystalline (liquid-disordered, ld) state, including the interlamellar forces as well as the repulsive forces acting among the lipid molecules. The fluctuations can range from collective 2D undulations, at distances greater than the bilayer thickness, to 3D collective deformations at smaller distances. A cutoff at about the segmental dimensions corresponds to short-range protrusion forces between the membrane surfaces at close apposition. Entropic forces due to spatial confinement of the fluctuations give rise to repulsions acting over the various length scales, which balance the long-range attractions, and affect the mesoscale interactions and structure of the system. How can we further distinguish the different regimes of the membrane lipid interactions?

Collective Modes and Order-Director Fluctuations (ODF) Affect Membrane Hydration—At relatively large distance scales (nm–μm), we can model the membrane as a flexible surface, where the collective motions represent wave-like undulations. The undulatory disturbances yield repulsive steric interactions between the various lamellae. Following Helfrich et al. [106, 108] the repulsive pressure (P_U) is given by:

$$P_U = \frac{3\pi(k_B T)^2}{128\, K_C D^3} \qquad (67)$$

By introducing Eqs. (58) and (60), the osmotic coefficient can then

be written as

$$\phi_{\mathrm{U}} = \frac{3\pi\, V_{\mathrm{W}}\, k_{\mathrm{B}}T}{128 K_{\mathrm{C}} D^3} \qquad .(68)$$

where D is the lamellar repeat spacing, and K_{C} is the modulus of bending rigidity for a single monolayer [272]. The squared dependence on the temperature is the result of handling the interaction as two thin entropic surfaces [272, 273]. Still, this approximation can fail when the membranes interact at short distances, which includes the length scales observed by NMR spectroscopy (e.g., when the water spacing is similar to the hydrocarbon thickness) [128, 274].

At low repeat spacings, the undulations depend on D_{W} instead of D as might be expected (there is an extra multiplicative numerical constant) [106, 108]. For the DMPC bilayer, the modulus of bending rigidity has been found [204] to be ≈ 0.6 x 10^{-19} J. Accordingly, we find that the theoretical osmotic coefficient ϕ_{U} due to 2D undulations contributes just a few percent of the measured value in Fig. 13. Because the undulations are weak, it is likely they are suppressed under dehydration. Other models for undulations exist [275] and yield stronger repulsive forces at larger ranges. Collective fluctuations at shorter ranges can occur, but with a different dimensionality and number of degrees of freedom. Quasi-elastic 3D fluctuations could possibly explain the variation in the temperature dependence of the osmotic coefficient at higher and lower hydrations. At a smaller intermembrane distances (below 20 Å), interactions on the order of the bilayer thickness come into play [18], and can yield repulsive steric interactions between the adjacent membranes (which have a similar temperature dependence as undulations). Such quasi-coherent motions of the flexible lipids have been formulated as a continuum of elastic 3D order-director fluctuations (ODF) [18]. Although purely undulation forces are too weak to explain the experimental osmotic coefficients, collective motions with a different dimensionality [18] may also contribute.

Short-Range Forces are Implicated in the Bilayer Hydration

For even shorter distances, the so-called hydration force has traditionally been considered, which yields an exponential distance decay: [71, 213, 214, 251]

$$P_{\mathrm{H}} = C \exp\left(-D_{\mathrm{W}}/\lambda_0\right) \qquad .(69)$$

Using Eq. (60), the corresponding osmotic coefficient can be written as

$$\phi_{\mathrm{H}} = \frac{C\, V_{\mathrm{W}}}{k_{\mathrm{B}}T} \exp\left(-D_{\mathrm{W}}/\lambda_0\right) \qquad ,(70)$$

where C is a constant and λ_0 is the characteristic decay length. By fitting a decaying exponential to experimental data using Eq. (69), we can work out the repulsive force (analogous to Fig. 13). For the DMPC-d_{54} bilayer, the decay length is found to be $\lambda_0 =$ 3.1 Å, which is close to the size of a water molecule [274]. Still, a larger decay constant of $\lambda_0 = 13.5$ Å is found at 65° C. The inconsistency has sparked debate about whether the repulsive force is due to the ordering of the water molecules, or yet another type of force. An alternative is an entropic-based force that is based on higher-dimensional order-director fluctuations, or protrusions of the lipid molecules [112]. Although an exponentially decaying force fits the available data, the length scale only matches the water dimensions near room temperature.

Difficulties with the hydration force bring us back to the idea that the repulsive force comes largely from entropic confinement, e.g., due to a distribution of membrane fluctuations [18, 115]. As Israelachvili and Wennerström have proposed [274], the entropic-based force acts at short distances, and originates in protrusions of the flexible lipid molecules [276] from the average membrane plane. The repulsive steric interactions give a pressure that can be calculated for low water spacings [274] as:

$$P_{\mathrm{P}} = \frac{2\rho k_{\mathrm{B}}T}{D_{\mathrm{W}}} \qquad .(71)$$

From Eq. (60), the osmotic coefficient corresponding to the protrusion force [53] then reads

$$\phi_{\mathrm{P}} = \frac{2\rho V_{\mathrm{W}}}{D_{\mathrm{W}}} = 2\rho \langle A \rangle \qquad ,(72)$$

where ρ is the number density of protruding molecules per unit area. For larger water spacing, the protrusion pressure reduces to an exponential decay [277]. As we dehydrate the membrane system (smaller N_{W}), Fig. 13 shows the osmotic coefficient becomes ~invariant as a function of the temperature. At 30 °C and assuming an osmotic pressure of 27.7 MPa, we obtain an osmotic coefficient of 0.258 and an average area per lipid of 48.1 Å^2. The density of protruding molecules is ρ = 0.268 molecules/nm^2, or roughly 1.3 protrusions per 10 lipids at any given instant. This value is ≈order of magnitude less than the rough estimate of ρ = 2 molecules/nm^2 [274]. Experiments with polymerizable lipids [278] under osmotic stress may also be relevant in this context.

9. Flexible Lipids in Cellular Membrane Function

With very few exceptions, lipid molecules work collectively in large groups rather than individually. In this collective action, molecular identity is often lost, and the synergistic material properties become relevant. The collective action of lipids has long been of interest—not only from a biological perspective, but also in soft-material science. For membrane lipids, solid-state ^{2}H NMR spectroscopy provides us with an unexpected answer to the question of how structure is related to function: material properties emerge at length scales comparable to the bilayer thickness or less [18, 115]. From spectral analysis and force-based membrane deformation, we arrive at the same conclusions as obtained from analysis of the lipid nuclear spin relaxation times at equilibrium [18, 115]. Simplified models yield the lipid properties in the context of linear response theory—in either case the process entails the same material constants [42, 262]. As a result, based on solid-state ^{2}H NMR spectroscopy, we are now able to answer the questions about lipid properties set forth in the Introduction.

(1) For the distance scale over which the atomic-level many-body interactions yield the continuum material properties, it is on the order of the bilayer thickness or smaller. Measurements of deformation by external stress show the material properties are detected at the atomistic level of the flexible phospholipid segments. This finding is both surprising and encouraging for the applicability of all-atom MD simulations to the analysis and interpretation of experimental data in terms of molecular force fields.

(2) The connection of the atomistic observables from NMR spectroscopy to material properties of lipids is obtained canonically from statistical mechanics laws. The orientational distribution function (i.e., the partition function) is formulated by a lattice model as in polymer physics, or alternatively by a mean-torque model used for liquid crystals. The relation to fundamental theories allows for investigating the nanomaterial deformations using spectroscopic data under the application of an external force.

(3) Lipid nanostructures show striking parallels to other liquid-crystalline states of matter [90, 279-281]. Besides average structural parameters, fluctuations of the lipids are described by order-director fluctuations (ODF), as first proposed from nuclear spin relaxation studies [18]. The continuum of quasi-elastic bilayer disturbances supports application of the fluctuation-dissipation theorem (FDT) to lipid membranes based on statistical physics.

(4) At the mesoscopic length scale, both a discrete and a continuum view are applicable. Yet for molecularly specific models, putting aside undersampling and ergodicity, the connection of force fields to macroscopic properties is less transparent than in analytical theories. Further insights are made possible by the confluence of experimental and numerical approaches, in which lipid membranes are regarded as materials with characteristic emerging properties.

9.1. Soft Membranes, Nanotechnology, and Lipid-Protein Interactions

Besides proteins, the cellular lipids and water—the soft matter of cellular biomembranes—are clearly important [8, 71]. Insights about the membrane interactions are obtained from combining spectroscopic and thermodynamic approaches. The connection to measurable properties such as the elasticity of thin membrane films can then be established (e.g., in terms of $\langle A \rangle$, D_C, and K_A for planar bilayers, and H_0, Gaussian curvature, and K_C for curved nanostructures such as hexagonal and cubic phases) [282, 283]. By introducing experimental observables from solid-state ^{2}H NMR spectroscopy, we have found that bilayers deform appreciably under osmotic stress. Typical lipid membranes undergo area reductions corresponding to increases in volumetric bilayer thickness of ≈ 20% for osmotic pressures in the range of 0–200 atmospheres. The interfacial area deformation is significantly anharmonic—the absolute area compression is substantially greater than for expansion beyond the lysis value of ≈ 3% at full hydration [26]. It is much easier for a bilayer to become thicker than thinner. The values of the moduli of compressibility (and bending rigidity) from the atomistic solid-state ^{2}H NMR observables match those obtained by treating the membrane as a continuum, as in micro- or nano-mechanics-based methods [7, 141, 284], like micropipette deformation [141, 261] or vesicle shape fluctuations [285]. Collective bilayer properties emerge over very short length scales, on the order of the bilayer thickness and even less [18, 115].

At a fundamental level, the dependence of bilayer repulsive forces on temperature illuminates their role in membrane deformation [272, 274]. At large interlamellar spacings (≈20 Å) undulations (2D) are operative; while at intermediate separations, collective fluctuations (3D) on the order of the bilayer thickness occur (≈10 Å) [18]. In the limit of small spacings (≈3 Å), protrusion forces [274] or hydration forces [231] occur as the bilayers are brought into close apposition. Notably the local microviscosity of the bilayer core matches that of liquid hydrocarbon, as first proposed

based on NMR relaxation studies [18, 115]. Emergence of quasi-elastic collective fluctuations on the order of the bilayer thickness and less [18] has immediate relevance to protein-lipid interactions over such length scales. [18, 286, 287]. Lipid bilayers exhibit collective excitations ranging from long-wavelength undulation modes on down to shorter wavelengths less than the bilayer thickness, together with short-range protrusions of the flexible molecular segments [18]. Applicability of a continuum flexible surface model (FSM) to lipid-protein interactions is supported at the mesoscopic length scale, i.e., on the order of the bilayer thickness and less [8].

Attractive and Repulsive Forces in Biomembranes Involve Lateral Pressures and Curvature Stress Fields—Membrane structure and assembly entail an intricate balance of attractive and repulsive forces that are challenging to formulate explicitly [48, 288]. One approach is to consider the atomistic-level forces acting on the lipid and protein constituents by a lateral pressure profile [43, 289, 290] as a function of depth within the bilayer [291, 292], as discussed above. The integral moments of the pressure profiles yield the continuum properties of lateral tension, bending rigidity, and monolayer and bilayer spontaneous curvature [59]. Yet the lateral pressure profile is not experimentally observable—it is invisible. One must rely on computer simulations, as in the classical work of Klaus Schulten et al. [155]. An alternative is to consider the elastic properties in terms of the monolayer spontaneous curvature and the associated bending rigidity, e.g., as formulated by the Helfrich Hamiltonian [62, 293-296]. A continuum approach based on differential geometry [44] then informs the properties of biomembranes, falling between the atomic or molecular dimensions and the overall membrane size. The flexible surface model [8, 43] describes how the curvature free energy affects membrane protein activity [202, 297, 298], as for ion channels and G-protein–coupled receptors (GPCRs).

9.2. Membrane Proteins as Sensors of Bilayer Stress

When considering how lipid interactions affect protein functions [8, 59, 104], one naturally deals with the mesoscopic length scale, i.e., falling between the bulk bilayer dimensions [7, 141, 204, 299] and the atomistic or molecular length scale of the phospholipids [300, 301]. Protein-lipid interactions are at the forefront of current biophysical thinking [8, 73, 201-203, 302-309], yet they often are omitted in popular descriptions like the fluid-mosaic model [310]. In spite of that, the ability of lipid bilayers to transduce physical deformations into useful biological work remains as a challenging scientific question [8, 24, 26, 43, 59, 60, 62, 63, 72, 85]. How can we gain added knowledge of the forces underlying the lipid interactions with proteins, [8, 43, 73] peptides [184, 311, 312], and cholesterol [1, 225, 313-315]? As set forth here, the understanding of how biomembranes carry out their functions involves lipid bilayers as materials endowed with characteristic physical properties. [8, 273, 316]. Examples of cellular functions that involve lipid-protein interactions include membrane trafficking and shape transformations, and receptor-based signaling, as in the case of viruses like influenza, dengue, HIV, Ebola, and other pathogens. Both lipids and proteins are major constituents of cellular membranes, and it is necessary to recognize the effects of the lipid bilayer [59, 202, 310] as shown experimentally [43, 73, 202, 277, 317-319].

Water and Lipids (Soft Matter) Plays Key Roles in Membrane Deformation—Another example is that dehydration stress can cause deformation of the area per lipid and hydrophobic thickness, which can yield significant restructuring of the proteolipid membrane. In fluid membranes, the bilayer remodeling amounts to changing the thickness by roughly four methylene carbon segments—large enough for changes in protein activity to occur by hydrophobic matching [43, 84, 202, 320-323]. Altering the lipid hydrophobic thickness by 4 Å pays an energy cost of about 0.3 *RT* per mole of lipids, assuming an average value of 1.5 *RT* for the free energy of transfer of methylene groups from hydrocarbon to water, e.g., see Tanford. [324, 325]. Bilayer deformations can thus shift the conformational equilibria of membrane proteins, such as ion channels [55] and G-protein–coupled receptors (GPCRs) [8] involving only a few *RT* per mole of protein molecules [1, 8, 31, 326, 327]. Considering rhodopsin [85, 328] or ion channels [303, 305] as other examples, such a description may offer a way to unify the diverse lipid influences on membrane protein functions [7, 8, 43, 85, 325, 329]. In the area of nanotechnology, the fundamental principles of lipid structure and dynamics can guide applications in industry, including surfactants [330-332], surface functionalization of paints and coatings, drug delivery, and medicine. Understanding how the physical properties of liquid crystal nanostructures emerge from chemical composition in manufacturing likewise aids the development of biocompatible materials. Tailored antimicrobial coatings [333] and controlled drug delivery benefit from the insights gained from lipid nanostructures, as well as interactions of lipids with nucleic acids in lipoplexes and nucleolipids for templated self-assembly [334]. Just as inorganic materials have revolutionized modern electronics, it is not only conceivable but in fact likely that organic or lipid-based lamellar and non-lamellar structures will become materials of choice in ~~for~~ future technologies.

9.3. Unraveling the Secrets of Soft Membrane Matter: Where Do We Go from Here?

Recognizing the enormous variety of lipids and proteins, attempting to understand cellular membranes at the molecular level can deter even the most experienced investigators. Biomembranes are at the forefront of physical biology, inasmuch as they are involved with energy transduction, cellular transport, signal transduction, and sensory functions. As a result, the collective role of lipid constituents is receiving increased attention in membrane biophysics [59, 335, 336]. The current review is focused on experimental developments in solid-state NMR spectroscopy that study the material properties of lipids over multiple length scales. Knowledge of material parameters (lipid packing density, membrane compressibility and deformations, orientational freedom, diffusion of lipids) is vital for understanding protein-lipid and DNA-lipid interactions, as well the quantitative biophysics of cell membranes in general. Our perspective combines the viewpoints on nano- and microscopic structure of lipid membranes, overviews the advances and possible descriptions on the mesoscopic level, as well as presents the thermodynamic properties and methods. Structural, dynamical, and functional roles of membrane lipids are central to understanding how soft matter (lipids and water) affects the essential processes of life itself [152, 174, 337]. Yet explaining the lipid effects is not always so obvious as for membrane proteins —it frequently requires modeling of the lipid assembly by computer simulations at large scale [338], with constant revision of force fields [10] Alternatively, the protein modes of action are often considered physically as local events, in which chemical specificity plays a major role: e.g., in structure-based drug design involving membrane receptors, ion channels, or transporters of metabolites. Going forward, understanding functional lipid-protein interactions will require bringing together both of these pictures. It will be interesting to see if the lipid bilayer deformations observed with solid-state NMR are involved in raft-like mixtures [313, 314, 339], as well as membrane peptide [134, 340] and protein interactions. The combined experimental and theoretical approach offers the key to explaining the physics and chemistry of cellular membranes—topics certain to capture the imagination of current and future investigators.

Acknowledgements:
This work was supported by the U.S. National Science Foundation, the U.S. National Institutes of Health, and the Indiana University-Purdue University Indianapolis Signature Center for Membrane Biosciences. We thank J. Nagle, A. Parsegian, and S. Tristram-Nagle for discussions.

Notes and references

[a] *Department of Chemistry and Biochemistry, University of Arizona, Tucson, Arizona 85721, USA. Fax: +1-520-621-8407; Tel: +1-520-621-2537; E-mail: kjmarjun@gmail.com*
[b] *Department of Physics (UG), Indian Institute of Science, Bengaluru, Karnataka-560012, India. Fax: +91-80-2293-2231; Tel: +91-984-420-5070; E-mail: kjmarjun@iisc.ac.in*
[c] *Department of Physics, Indiana University-Purdue University, Indianapolis, Indiana 46202, USA. Fax: +1-317-274-2392; Tel: +1-317-278-6521; E-mail: jkinnun@umail.iu.edu, hpetrach@iupui.edu*
[d] *Department of Physics, University of Arizona, Tucson, Arizona, USA. Fax: +1-520-621-8407; Tel: +1- 520-621-2163; E-mail: mfbrown@u.arizona.edu*
* Corresponding author

References

1. M. F. Brown, *Annu. Rev. Biophys.*, 2017, **46**, 379-410.
2. D. Marquardt, M. D. Frontzek, Y. Zhao, B. C. Chakoumakos and J. Katsaras, *J. Appl. Crystallogr.*, 2018, **51**, 235-241.
3. J. F. Nagle, *Phys. Rev. E*, 2017, **96**, 103.
4. N. Kucerka, F. A. Heberle, J. J. Pan and J. Katsaras, *Membranes*, 2015, **5**, 454-472.
5. P. Heftberger, B. Kollmitzer, F. A. Heberle, J. J. Pan, M. Rappolt, H. Amenitsch, N. Kucerka, J. Katsaras and G. Pabst, *J. Appl. Crystallogr.*, 2014, **47**, 173-180.
6. J. N. Israelachvili, *Intermolecular and Surface Forces, 3rd Ed.*, Academic Press, San Diego, 2011.
7. E. Evans and D. Needham, *J. Phys. Chem.*, 1987, **91**, 4219–4228.
8. M. F. Brown, *Biochemistry*, 2012, **51**, 9782–9795.
9. P. A. Gurnev, T. C. Roark, H. I. Petrache, A. J. Sodt and S. M. Bezrukov, *Angew. Chem.*, 2017, **56**, 3506-3509.
10. A. N. Leonard, A. C. Simmonett, F. C. Pickard, J. Huang, R. M. Venable, J. B. Klauda, B. R. Brooks and R. W. Pastor, *J. Chem. Theory Comput.*, 2018, **14**, 948-958.
11. C. G. Mayne, M. J. Arcario, P. Mahinthichaichan, J. L. Baylon, J. V. Vermaas, L. Navidpour, P. C. Wen, S. Thangapandian and E. Tajkhorshid, *Biochim. Biophys. Acta*, 2016, **1858**, 2290-2304.
12. R. M. Venable, F. L. H. Brown and R. W. Pastor, *Chem. Phys. Lipids*, 2015, **192**, 60-74.
13. Y. F. Qi, J. M. Lee, A. Singharoy, R. McGreevy, K. Schulten and W. Im, *J. Phys. Chem. B*, 2017, **121**, 3718-3723.
14. S. J. Marrink, A. H. de Vries and A. E. Mark, *J. Phys. Chem. B*, 2004, **108**, 750-760.
15. A. Srivastava and G. A. Voth, *J. Chem. Theory Comput.*, 2013, **9**, 750-765.
16. A. Davtyan, M. Simunovic and G. A. Voth, *J. Chem. Phys.*, 2017, **147**.
17. P. C. Hsu, B. M. H. Bruininks, D. Jefferies, P. C. T. de Souza, J. Lee, D. S. Patel, S. J. Marrink, Y. F. Qi, S. Khalid and W. Im, *J. Comput. Chem.*, 2017, **38**, 2354-2363.
18. M. F. Brown, *J. Chem. Phys.*, 1982, **77**, 1576–1599.

19. M. Bloom, E. Evans and O. G. Mouritsen, *Q. Rev. Biophys.*, 1991, **24**, 293-397.
20. G. S. Ayton and G. A. Voth, *Semin. Cell Dev. Biol.*, 2010, **21**, 357-362.
21. J. Seelig, *Q. Rev. Biophys.*, 1977, **10**, 353-418.
22. A. Leftin and M. F. Brown, *Biochim. Biophys. Acta*, 2011, **1808**, 818–839.
23. T. R. Molugu, S. Lee and M. F. Brown, *Chem. Rev.* , 2017, **117**, 12087-12132.
24. H. I. Petrache, S. W. Dodd and M. F. Brown, *Biophys. J.*, 2000, **79**, 3172–3192.
25. H. I. Petrache and M. F. Brown, in *Methods in Molecular Biology*, ed. A. M. Dopico, Humana press, Totowa, 2007, vol. 400, pp. 341–353.
26. K. J. Mallikarjunaiah, A. Leftin, J. J. Kinnun, M. J. Justice, A. L. Rogozea, H. I. Petrache and M. F. Brown, *Biophys. J.*, 2011, **100**, 98–107.
27. M. Chavent, A. L. Duncan and M. S. P. Sansom, *Curr. Opin. Struct. Biol.*, 2016, **40**, 8-16.
28. A. H. Beaven, A. M. Maer, A. J. Sodt, H. Rui, R. W. Pastor, O. S. Andersen and W. Im, *Biophys. J.*, 2017, **112**, 1185-1197.
29. X. L. Leng, J. J. Kinnun, A. T. Cavazos, S. W. Canner, S. R. Shaikh, S. E. Feller and S. R. Wassall, *Biochim. Biophys. Acta*, 2018, **1860**, 1125-1134.
30. L. A. Salas-Estrada, N. Leioatts, T. D. Romo and A. Grossfield, *Biophys. J.*, 2018, **114**, 355-367.
31. H. Heller, K. Schaefer and K. Schulten, *J. Phys. Chem.*, 1993, **97**, 8343–8360.
32. S. E. Feller, Y. H. Zhang, R. W. Pastor and B. R. Brooks, *J. Chem. Phys.*, 1995, **103**, 4613–4621.
33. G. S. Ayton, J. L. McWhirter and G. A. Voth, *J. Chem. Phys.*, 2006, **124**, 064906.
34. E. Schneck, F. Sedlmeier and R. R. Netz, *Proc. Natl. Acad. Sci. U. S. A.*, 2012, **109**, 14405–14409.
35. A. S. Reddy, D. T. Warshaviak and M. Chachisvilis, *Biochim. Biophys. Acta*, 2012, **1818**, 2271–2281.
36. B. R. Brooks, R. E. Bruccoleri, B. D. Olafson, S. Swaminathan and M. Karplus, *J. Comp. Chem.*, 1983, **4**, 187–217.
37. R. Henderson, *Quart. Rev. Biophys.*, 1995, **28**, 171–193.
38. A. J. Sodt and R. W. Pastor, *J. Chem. Phys.*, 2012, **137**, 234101.
39. H. Yu and K. Schulten, *PLoS Comput. Biol.*, 2013, **9**, 1002892.
40. S. J. Marrink, H. J. Risselada, S. Yefimov, D. P. Tieleman and A. H. de Vries, *J. Phys. Chem. B*, 2007, **111**, 7812–7824.
41. F. B. Naughton, A. C. Kalli and M. S. P. Sansom, *J. Mol. Biol.*, 2018, **430**, 372-388.
42. M. F. Brown, R. L. Thurmond, S. W. Dodd, D. Otten and K. Beyer, *J. Am. Chem. Soc.*, 2002, **124**, 8471–8484.
43. M. F. Brown, *Chem. Phys. Lipids*, 1994, **73**, 159-180.
44. S. T. Hyde, S. Andersson, K. Larsson, Z. Blum, T. Landh, S. Lidin and B. W. Ninham, *The Language of Shape. The Role of Curvature in Condensed Matter: Physics, Chemistry and Biology*, Elsevier, Amsterdam, 1997.
45. F. L. H. Brown, in *Annu. Rev. Phys. Chem.*, 2008, vol. 59, pp. 685-712.
46. W. E. Teague Jr., O. Soubias, H. Petrache, N. Fuller, K. G. Hines, R. P. Rand and K. Gawrisch, *Faraday Discuss.*, 2013, **161**, 383–395.
47. O. Soubias, W. E. Teague Jr., K. G. Hines and K. Gawrisch, *Biophys. J.*, 2015, **108**, 1125–1132.
48. V. A. Parsegian, *Van der Waals Forces: A Handbook for Biologists, Chemists, Engineers, and Physicists*, Cambridge University Press, 2006.
49. W. Helfrich, *Z. Naturf.*, 1975, **30c**, 841-842.
50. R. P. Rand and V. A. Parsegian, *Biochim. Biophys. Acta*, 1989, **988**, 351–376.
51. T. J. McIntosh and S. A. Simon, *Biochemistry*, 1993, **32**, 8374-8384.
52. J. N. Israelachvili and B. W. Ninham, *J. Colloid Interface Sci.*, 1977, **58**, 14-25.
53. J. N. Israelachvili and H. Wennerstrom, *Langmuir*, 1990, **6**, 873-876.
54. S. I. Sukharev, P. Blount, B. Martinac, F. R. Blattner and C. Kung, *Nature (London)*, 1994, **368**, 265-268.
55. E. Perozo, D. M. Cortes, P. Sompornpisut , A. Kloda and B. Martinac, *Nature*, 2002, **418**, 942–948.
56. M. J. Bruno, R. Rusinova, N. J. Gleason, R. E. Koeppe and O. S. Andersen, *Faraday Discuss.*, 2013, **161**, 461-480.
57. M. F. Brown, N. J. Gibson and R. L. Thurmond, *Biophys. J.*, 1996, **70**, A442.
58. M. F. Brown, *J. Chem. Phys.*, 1984, **80**, 2808-2831.
59. R. Phillips, T. Ursell, P. Wiggins and P. Sens, *Nature*, 2009, **459**, 379–385.
60. J. F. Nagle and S. Tristram-Nagle, *Biochim. Biophys. Acta*, 2000, **1469**, 159–195.
61. B. J. Peter, H. M. Kent, I. G. Mills, Y. Vallis, P. J. G. Butler, P. R. Evans and H. T. McMahon, *Science*, 2004, **303**, 495-499.
62. J. Zimmerberg and M. M. Kozlov, *Nat. Rev. Mol. Cell Biol.*, 2006, **7**, 9–19.
63. G. van Meer, D. R. Voelker and G. W. Feigenson, *Nat. Rev. Mol. Cell Biol.*, 2008, **9**, 112–124.
64. R. Metzler, J. H. Jeon and A. G. Cherstvy, *Biochim. Biophys. Acta*, 2016, **1858**, 2451-2467.
65. R. M. Venable, H. I. Ingolfsson, M. G. Lerner, B. S. Perrin, B. A. Camley, S. J. Marrink, F. L. H. Brown and R. W. Pastor, *Journal of Physical Chemistry B*, 2017, **121**, 3443-3457.
66. M. F. Brown, eds. M.-P. Nieh, F. A. Heberle and J. Katsaras, De Gruyter, Berlin, 2019.
67. D. Marsh, *Handbook of Lipid Bilayers, 2nd Ed.*, CRC Press, Boca Raton, 2013.
68. G. Lindblom and L. Rilfors, *Biochim. Biophys. Acta*, 1989, **988**, 221-256.
69. N. Johner, S. Mondal, G. Morra, M. Caffrey, H. Weinstein and G. Khelashvili, *J. Am. Chem. Soc.*, 2014, **136**, 3271-3284.
70. P. Nogly, V. Panneels, G. Nelson, C. Gati, T. Kimura, C. Milne, D. Milathianaki, M. Kubo, W. Wu, C. Conrad, J. Coe, R. Bean, Y. Zhao, P. Bath, R. Dods, R. Harimoorthy, K. R. Beyerlein, J. Rheinberger, D. James, D. DePonte, C. Li, L. Sala, G. J. Williams, M. S. Hunter, J. E. Koglin, P. Berntsen, E. Nango, S. Iwata, H. N. Chapman, P. Fromme, M. Frank, R. Abela, S. Boutet, A. Barty, T. A. White, U. Weierstall, J. Spence, R. Neutze, G. Schertler and J. Standfuss, *Nat. Commun.*, 2016, **7**, 12314.
71. V. A. Parsegian, N. Fuller and P. R. Rand, *Proc. Natl. Acad. Sci. USA*, 1979, **76**, 2750–2759.
72. J. Zimmerberg and K. Gawrisch, *Nature Chem. Biol.*, 2006, **2**, 564–567.

73. A. G. Lee, *Biochim. Biophys. Acta*, 2004, **1666**, 62-87.

74. M. C. Rheinstädter, C. Ollinger, G. Fragneto, F. Demmel and T. Salditt, *Phys. Rev. Lett.*, 2004, **93**, 108107.

75. M. Dorrell, F. Heberle, J. Katsaras and E. Lyman, *Biophys. J.*, 2017, **112**, 468A.

76. J. F. Nagle, R. T. Zhang, S. Tristram-Nagle, W. J. Sun, H. I. Petrache and R. M. Suter, *Biophys. J.*, 1996, **70**, 1419–1431.

77. D. G. Ackerman and G. W. Feigenson, in *Membrane Nanodomains*, ed. I. Parmryd, 2015, vol. 57, pp. 33-42.

78. M. C. Blosser, A. R. Honerkamp-Smith, T. Han, M. Haataja and S. L. Keller, *Biophys. J.*, 2015, **109**, 2317-2327.

79. E. Sezgin, H. J. Kaiser, T. Baumgart, P. Schwille, K. Simons and I. Levental, *Nat. Protoc.*, 2012, **7**, 1042-1051.

80. S. L. Goh, J. J. Amazon and G. W. Feigenson, *Biophys. J.*, 2013, **104**, 853-862.

81. T. M. Konyakhina and G. W. Feigenson, *Biochim. Biophys. Acta*, 2016, **1858**, 153-161.

82. Y. J. Min, N. Pesika, J. Zasadzinski and J. Israelachvili, *Langmuir*, 2010, **26**, 8684-8689.

83. R. L. Schoch, I. Barel, F. L. H. Brown and G. Haran, *J. Chem. Phys.*, 2018, **148**, 123333.

84. T. S. Wiedmann, R. D. Pates, J. M. Beach, A. Salmon and M. F. Brown, *Biochemistry*, 1988, **27**, 6469-6474.

85. O. Soubias, W. E. Teague, K. G. Hines, D. C. Mitchell and K. Gawrisch, *Biophys. J.*, 2010, **99**, 817–824.

86. X. Agirrezabala, H. Y. Liao, E. Schreiner, J. Fu, R. F. Ortiz-Meoz, K. Schulten, R. Green and J. Frank, *Proc. Natl. Acad. Sci. U. S. A.*, 2012, **109**, 6094-6099.

87. L. R. Brown, A. Braun, A. Kumar and K. Wüthrich, *Biophys. J.*, 1982, **37**, 319-328.

88. E. Lindahl and O. Edholm, *Biophys. J.*, 2000, **79**, 426-433.

89. P. G. de Gennes and J. Prost, *The Physics of Liquid Crystals, 2nd Ed.*, Oxford University Press, Oxford, 1993.

90. M. Mitov, *Soft Matter*, 2017, **13**, 4176-4209.

91. F. Volke, S. Eisenblatter, J. Galle and G. Klose, *Chem. Phys. Lipids*, 1994, **70**, 121-131.

92. F. Volke, S. Eisenblatter and G. Klose, *Biophys. J.*, 1994, **67**, 1882-1887.

93. M. F. Brown, S. Lope-Piedrafita, G. V. Martinez and H. I. Petrache, in *Modern Magnetic Resonance*, ed. G. A. Webb, Springer, Heidelberg, 2006.

94. J. F. Nagle, *Chem. Phys. Lipids*, 2017, **205**, 18-24.

95. M. M. Terzi and M. Deserno, *J. Chem. Phys.*, 2017, **147**, 084702.

96. E. Endress, H. Heller, H. Casalta, M. F. Brown and T. Bayerl, *Biochemistry*, 2002, **41**, 13078-13086.

97. E. Mamontov and X.-q. Chu, *Phys. Chem. Chem. Phys.*, 2012, **14**, 11573-11588.

98. G. Büldt, H. U. Gally, A. Seelig, J. Seelig and G. Zaccai, *Nature*, 1978, **271**, 182-184.

99. D. Krepkiy, M. Mihailescu, J. A. Freites, E. V. Schow, D. L. Worcester, K. Gawrisch, D. J. Tobias, S. H. White and K. J. Swartz, *Nature*, 2009, **462**, 473–479.

100. B. Koenig, H. Strey and K. Gawrisch, *Biophys. J.*, 1997, **73**, 1954–1966.

101. A. Brown, I. Skanes and M. R. Morrow, *Phys. Rev. E*, 2004, 011913.

102. A. V. Struts, G. F. Salgado and M. F. Brown, *Proc. Natl. Acad. Sci. U. S. A.*, 2011, **108**, 8263–8268.

103. A. Vogel, M. Roark and S. E. Feller, *Biochim. Biophys. Acta*, 2012, **1818**, 219-224.

104. O. H. S. Ollila, H. J. Risselada, M. Louhivuori, E. Lindahl, I. Vattulainen and S. J. Marrink, *Phys. Rev. Lett.*, 2009, **102**, 078101.

105. I. Levental, M. Grzybek and K. Simons, *Biochemistry*, 2010, **49**, 6305–6316.

106. W. Helfrich, *Z. Naturforsch.*, 1973, **28c**, 693-703.

107. M. F. Brown, A. J. Deese and E. A. Dratz, *Methods Enzymol.*, 1982, **81**, 709-728.

108. W. Helfrich and R.-M. Servuss, *Nuovo Cim.*, 1984, **3**, 137–151.

109. R. W. Pastor, R. M. Venable, M. Karplus and A. Szabo, *J. Chem. Phys.*, 1988, **89**, 1128-1140.

110. D. F. Evans, D. J. Mitchell and B. W. Ninham, *J. Phys. Chem.*, 1986, **90**, 2817-2825.

111. T. J. McIntosh and S. A. Simon, *Biochemistry*, 1986, **25**, 4058–4066.

112. J. N. Israelachvili and H. Wennerström, *Langmuir*, 1990, **6**, 873-876.

113. J. F. Nagle, *Biophys. J.*, 1993, **64**, 1476–1481.

114. J. F. Nagle, *Faraday Discuss.*, 2013, **161**, 11–29.

115. M. F. Brown, A. A. Ribeiro and G. D. Williams, *Proc. Natl. Acad. Sci. USA*, 1983, **80**, 4325–4329.

116. J. Marra and J. N. Israelachvili, *Biochemistry*, 1985, **24**, 4608-4618.

117. V. Luzzati and F. Husson, *J. Cell. Biol.*, 1962, **12**, 207-219.

118. R. P. Rand, *Annu. Rev. Biophys. Bioeng.*, 1981, **10**, 277–314.

119. V. A. Parsegian, R. P. Rand and D. C. Rau, *Meth. Enzymol.*, 1995, **259**, 43–94.

120. K. J. Mallikarjunaiah, Ramesh, K. P., Damle, R., *Phys. Status Solidi-b*, 2007, **244**, 3809-3816.

121. M. F. Brown and S. I. Chan, in *Encyclopedia of Nuclear Magnetic Resonance*, eds. D. M. Grant and R. K. Harris, Wiley, New York, 1996, vol. 2, pp. 871-885.

122. F. H. Larsen, H. J. Jakobsen, P. D. Ellis and N. C. Nielsen, *Chem. Phys. Lett.*, 1998, **292**, 467-473.

123. A. T. Brunger, P. D. Adams, G. M. Clore, W. L. DeLano, P. Gros, R. W. Grosse-Kunstleve, J. S. Jiang, J. Kuszewski, M. Nilges, N. S. Pannu, R. J. Read, L. M. Rice, T. Simonson and G. L. Warren, *Acta Cryst. D*, 1998, **54**, 905-921.

124. K. J. Mallikarjunaiah, R. Damle and K. P. Ramesh, *Solid State Nucl. Magn. Reson.*, 2008, **34**, 180-185.

125. K. J. Mallikarjunaiah and R. Damle, *Solid-State NMR and Its Implications in Molecular Dynamics Study*, Lambert Academic Publishing, Saarbrücken, 2011.

126. K. P. Ramesh, in *Annual Reports on NMR Spectroscopy, Vol 71*, ed. G. A. Webb, 2010, vol. 71, pp. 139-175.

127. M. Manjunatha, G. S. Reddy, R. Damle, K. J. Mallikarjunaiah and K. P. Ramesh, *Ceramics International*, 2019, **in press**.

128. M. F. Brown, Miljanich, G.P., Dratz, E.A., *Proc. Natl. Acad. Sci. U. S. A.*, 1977, **74**, 1978-1982.

129. A. A. Nevzorov, S. Moltke and M. F. Brown, *J. Am. Chem. Soc.*, 1998, **120**, 4798-4805.

130. A. A. Nevzorov, S. Moltke, M. P. Heyn and M. F. Brown, *J. Am. Chem. Soc.*, 1999, **121**, 7636-7643.

131. Y. M. Miao, H. J. Qin, R. Q. Fu, M. Sharma, T. V. Can, I. Hung, S. Luca, P. L. Gor'kov, W. W. Brey and T. A. Cross, *Angew. Chem. Int. Ed.*, 2012, **51**, 8383–8386.

132. J. J. Kinnun, A. Leftin and M. F. Brown, *J. Chem. Educ.*, 2013, **90**, 123–128.

133. J. Cavanaugh, W. J. Fairbrother, A. G. Palmer III, N. J. Skelton and M. Rance, *Protein NMR Spectroscopy: Principles and Practice, Second Edition*, Academic Press, New York, 2006.

134. A. Leftin, C. Job, K. Beyer and M. F. Brown, *J. Mol. Biol.*, 2013, **425**, 2973-2987.

135. A. Leftin, T. R. Molugu, C. Job, K. Beyer and M. F. Brown, *Biophys. J.*, 2014, **107**, 2274-2286.

136. H. I. Petrache, D. Harries and V. A. Parsegian, in *Methods in Membrane Lipids*, ed. A. M. Dopico, Humana press, Totowa, 2007, vol. 400, pp. 405–420.

137. Z. Salamon, M. F. Brown and G. Tollin, *Trends Biochem. Sci.*, 1999, **24**, 213-219.

138. F. M. Linseisen, M. Hetzer, T. Brumm and T. M. Bayerl, *Biophys.J.*, 1997, **72**, 1659-1667.

139. O. Soubias, I. V. Polozov, W. E. Teague, A. A. Yeliseev and K. Gawrisch, *Biochemistry*, 2006, **45**, 15583-15590.

140. A. Vaish, V. Silin, M. L. Walker, K. L. Steffens, S. Krueger, A. A. Yeliseev, K. Gawrisch and D. J. Vanderah, *Chemical Communications*, 2013, **49**, 2685-2687.

141. T. Baumgart, B. R. Capraro, C. Zhu and S. L. Das, *Annu. Rev. Phys. Chem.*, 2011, **62**, 483–506.

142. T. P. Trouard, T. M. Alam and M. F. Brown, *J. Chem. Phys.*, 1994, **101**, 5229-5261.

143. T. P. Trouard, A. A. Nevzorov, T. M. Alam, C. Job, J. Zajicek and M. F. Brown, *J. Chem. Phys.*, 1999, **110**, 8802-8818.

144. T. M. Bayerl and M. Bloom, *Biophys. J.*, 1990, **58**, 357-362.

145. J. H. Davis, *Biophys. J.*, 1979, **27**, 339-358.

146. A. Blume, D. M. Rice, R. J. Wittebort and R. G. Griffin, *Biochemistry*, 1982, **21**, 6220-6230.

147. J. A. Barry, T. P. Trouard, A. Salmon and M. F. Brown, *Biochemistry*, 1991, **30**, 8386–8394.

148. M. R. Vist and J. H. Davis, *Biochemistry*, 1990, **29**, 451-464.

149. J. Henriksen, A. C. Rowat, E. Brief, Y. W. Hsueh, J. L. Thewalt, M. J. Zuckermann and J. H. Ipsen, *Biophys J*, 2006, **90**, 1639-1649.

150. M. C. Wiener and S. H. White, *Biophys. J.*, 1992, **61**, 434-447.

151. C. Ho, S. J. Slater and C. D. Stubbs, *Biochemistry*, 1995, **34**, 6188–6195.

152. H. I. Petrache, A. Salmon and M. F. Brown, *J. Am. Chem. Soc.*, 2001, **123**, 12611–12622.

153. K. M. Hallinen, S. Tristram-Nagle and J. F. Nagle, *Phys. Chem. Chem. Phys.*, 2012, **14**, 15452-15457.

154. H. I. Petrache, S. E. Feller and J. F. Nagle, *Biophys. J.*, 1997, **72**, 2237–2242.

155. M. Greferath, B. Blümich, W. M. Griffith and G. L. Hoatson, *J. Magn. Reson.*, 1993, **102**, 73–80.

156. T. M. Ferreira, B. Medronho, R. W. Martin and D. Topgaard, *Phys. Chem. Chem. Phys.*, 2008, **10**, 6033-6038.

157. M. F. Brown, in *Biological Membranes: A Molecular Perspective from Computation and Experiment*, eds. K. Merz Jr. and B. Roux, Birkhäuser, Basel, 1996, pp. 175–252.

158. H. I. Petrache, S. Tristram-Nagle and J. F. Nagle, *Chem. Phys. Lipids*, 1998, **95**, 83.

159. J. F. Nagle and S. Tristram-Nagle, *Curr. Opin. Struct. Biol.*, 2000, **10**, 474–480.

160. G. Zaccai, G. Büldt, A. Seelig and J. Seelig, *J. Molec. Biol.*, 1979, **134**, 693-706.

161. V. Luzzati, in *Biological Membranes*, ed. D. Chapman, Academic Press, New York, 1968, vol. 1, pp. 71–123.

162. M. C. Wiener, S. Tristram-Nagle, D. A. Wilkinson, L. E. Campbell and J. F. Nagle, *Biochim. Biophys. Acta*, 1988, **938**, 135-142.

163. L. J. Lis, M. McAlister, N. Fuller, R. P. Rand and V. A. Parsegian, *Biophys. J.*, 1982, **37**, 6677-6672.

164. D. C. Turner and S. M. Gruner, *Biochemistry*, 1992, **31**, 1340-1355.

165. J. M. Seddon, R. H. Templer, N. A. Warrender, Z. Huang, G. Cevc and D. Marsh, *Biochim. Biophys. Acta*, 1997, **1327**, 131-147.

166. H. I. Petrache, N. Gouliaev, S. Tristram-Nagle, R. T. Zhang, R. M. Suter and J. F. Nagle, *Phys. Rev. E*, 1998, **57**, 7014–7024.

167. M. A. McCabe, G. L. Griffith, W. D. Ehringer, W. Stillwell and S. R. Wassall, *Biochemistry*, 1994, **33**, 7203-7210.

168. D. M. Engelman, *Nature*, 2005, **438**, 578-580.

169. A. I. I. Tyler, R. V. Law and J. M. Seddon, in *Methods in Membrane Lipids, Second Edition*, ed. D. M. Owen, 2015, vol. 1232, pp. 199-225.

170. J. Seelig and A. Seelig, *Biochem. Biophys. Res. Commun.*, 1974, **57**, 406-411.

171. H. Schindler and J. Seelig, *Biochemistry*, 1975, **14**, 2283-2287.

172. M. Jansson, R. L. Thurmond, J. A. Barry and M. F. Brown, *J. Phys. Chem.*, 1992, **96**, 9532-9544.

173. D. M. Brink and G. R. Satchler, *Angular Momentum*, Oxford University Press, London, 1968.

174. A. Salmon, S. W. Dodd, G. D. Williams, J. M. Beach and M. F. Brown, *J. Am. Chem. Soc.*, 1987, **109**, 2600–2609.

175. M. F. Brown, J. Seelig and U. Häberlen, *J. Chem. Phys.*, 1979, **70**, 5045–5053.

176. K. A. Dill and P. J. Flory, *Proc. Natl. Acad. Sci. USA*, 1980, **77**, 3115–3119.

177. L. E. Reichl, *A Modern Course in Statistical Physics*, WILEY-VCH Verlag GmbH & Co. KGaA, 2016.

178. M. E. Rose, *Elementary Theory of Angular Momentum*, Wiley, New York, 1957.

179. H. W. G. Arfken, F. E. Harris, *Mathematical Methods for Physicists*, Academic Press, 2012.

180. C. Zannoni, in *Nuclear Magnetic Resonance of Liquid Crystals*, ed. J. W. Emsley, D. Reidel Publishing Company, Dordrecht, 1985, pp. 1-34.

181. U. Nilsson, B. Jönsson and H. Wennerström, *J. Phys. Chem.*, 1993, **97**, 5654-5660.

182. A. E. Blaurock and T. J. McIntosh, *Biochemistry*, 1986, **25**, 299-305.

183. C. J. Hogberg and A. P. Lyubartsev, *J. Phys. Chem. B*, 2006, **110**, 14326–14336.

184. K. A. Henzler Wildman, G. V. Martinez, M. F. Brown and A. Ramamoorthy, *Biochemistry*, 2004, **43**, 8459–8469.

185. T. R. Molugu and M. F. Brown, *Chem. Phys. Lipids*, 2016, **199**, 39-51.

186. W. Shinoda and S. Okazaki, *J. Chem. Phys.*, 1998, **109**, 1517-1521.

187. T. Huber, A. V. Botelho, K. Beyer and M. F. Brown, *Biophys. J.*, 2004, **86**, 2078-2100.

188. P. Jedlovszky, N. N. Medvedev and M. Mezei, *J. Phys. Chem. B*, 2004, **108**, 465-472.

189. S. A. Pandit, S. Vasudevan, S. W. Chiu, R. J. Mashl, E. Jakobsson and H. L. Scott, *Biophys. J.*, 2004, **87**, 1092-1100.

190. J. F. Nagle and D. A. Wilkinson, *Biophys. J.*, 1978, **23**, 159–175.

191. R. S. Armen, O. D. Uitto and S. E. Feller, *Biophys. J.*, 1998, **75**, 734–744.

192. G. W. Stockton and I. C. P. Smith, *Chem. Phys. Lipids*, 1976, **17**, 251-263.

193. H. I. Petrache, K. Tu and J. F. Nagle, *Biophys. J.*, 1999, **76**, 2479–2487.

194. T. Huber, A. V. Botelho and M. F. Brown, *Biophys. J.*, 2002, **82**, 225a.

195. S. H. White, R. E. Jacobs and G. I. King, *Biophys. J.*, 1987, **52**, 663–665.

196. T. J. McIntosh, S. Advani, R. E. Burton, D. V. Zhelev, D. Needham and S. A. Simon, *Biochemistry*, 1995, **34**, 8520–8532.

197. T. Baumgart, S. Das, W. W. Webb and J. T. Jenkins, *Biophys. J.*, 2005, **89**, 1067-1080.

198. J. Israelachvili, *Intermolecular and Surface Forces*, Academic Press, New York, 2nd edn., 1992.

199. H. Wennerström, *Pure & Appli. Chem.*, 1988, **60**, 1529-1534.

200. R. P. Rand and V. A. Parsegian, in *The Structure of Biological Membranes*, ed. P. L. Yeagle, 2004, pp. 201–241.

201. A. V. Botelho, N. J. Gibson, Y. Wang, R. L. Thurmond and M. F. Brown, *Biochemistry*, 2002, **41**, 6354–6368.

202. A. V. Botelho, T. Huber, T. P. Sakmar and M. F. Brown, *Biophys. J.*, 2006, **91**, 4464–4477.

203. R. Nygaard, Y. Zou, R. O. Dror, T. J. Mildorf, D. H. Arlow, A. Manglik, A. C. Pan, C. W. Liu, J. J. Fung, M. P. Bokoch, F. S. Thian, T. S. Kobilka, D. E. Shaw, L. Mueller, R. S. Prosser and B. K. Kobilka, *Cell*, 2013, **152**, 532–542.

204. W. Rawicz, K. C. Olbrich, T. McIntosh, D. Needham and E. Evans, *Biophys. J.*, 2000, **79**, 328–339.

205. D. Chandler, *Nature (London)*, 2005, **437**, 640–647.

206. T. J. McIntosh and S. A. Simon, *Annu. Rev. Biophys. Biomol. Struct.*, 2006, **35**, 177–198.

207. R. Munns, *Plant Cell Environ.*, 2002, **25**, 239–250.

208. L. Miao, B. Fourcade, M. Rao, M. Wortis and R. K. Zia, *Phys. Rev. A*, 1991, **43**, 6843-6856.

209. D. C. Mitchell, J. Kibelbek and B. J. Litman, *Biochemistry*, 1991, **30**, 37-42.

210. L. M. Crowe and J. H. Crowe, *Arch. Biochem. Biophys.*, 1982, **217**, 582-587.

211. J. H. Crowe, L. M. Crowe and D. Chapman, *Science (Washington D C)*, 1984, **223**, 701-703.

212. S. K. Balasubramanian, W. F. Wolkers and J. C. Bischof, *Biochim. Biophys. Acta*, 2009, **1788**, 945-953.

213. D. M. LeNeveu, R. P. Rand, D. Gingell and V. A. Parsegian, *Science*, 1976, **191**, 399–400.

214. T. J. McIntosh, A. D. Magid and S. A. Simon, *Biochemistry*, 1987, **26**, 7325–7332.

215. E. Sparr, L. Hallin, N. Markova and H. Wennerstrom, *Biophys. J.*, 2002, **83**, 2015-2025.

216. G. Pabst, J. Katsaras, V. A. Raghunathan and M. Rappolt, *Langmuir*, 2003, **19**, 1716-1722.

217. P. R. Rand, T. S. Reese and R. G. Miller, *Nature*, 1981, **293**, 237-238.

218. V. A. Parsegian, R. P. Rand, N. L. Fuller and D. C. Rau, *Meth. Enzymol.*, 1986, **127**, 400–416.

219. F. T. Wall, *Chemical Thermodynamics: A Course of Study*, W.H. Freeman, 1965.

220. R. Aveyard and D. A. Haydon, *An Introduction to the Principles of Surface Chemistry*, Cambridge University Press, London, 1973.

221. J. F. Nagle and M. C. Wiener, *Biochim. Biophys. Acta*, 1988, **942**, 1–10.

222. J. F. Nagle, R. T. Zhang, S. Tristram-Nagle, W. J. Sun, H. I. Petrache and R. M. Suter, *Biophys. J.*, 1996, **70**, 1419-1431.

223. Y. F. Liu, Y. Lyatskaya, S. Tristram-Nagle, J. Katsaras and J. F. Nagle, *Biophys. J.*, 2001, **80**, 14A-14A.

224. M. F. Brown, in *Lipid Polymorphism and Membrane Properties*, ed. R. M. Epand, 1997, vol. 44, pp. 285-356.

225. K. J. Mallikarjunaiah, J. J. Kinnun, H. I. Petrache and M. F. Brown, *Biophys. J.*, 2012, **102**, 505a.

226. E. Tajkhorshid, P. Nollert, M. O. Jensen, L. J. W. Miercke, J. O'Connell, R. M. Stroud and K. Schulten, *Science*, 2002, **296**, 525–530.

227. J. Gullingsrud and K. Schulten, *Biophys. J.*, 2004, **86**, 3496–3509.

228. S.-J. Marrink, M. Berkowitz and H. J. Berendsen, *Langmuir*, 1993, **9**, 3122–3131.

229. P. D. Blood and G. A. Voth, *Proc. Natl. Acad. Sci. U. S. A.*, 2006, **103**, 15068–15072.

230. J. F. Nagle, M. S. Jablin, S. Tristram-Nagle and K. Akabori, *Chem. Phys. Lipids*, 2015, **185**, 3-10.

231. T. J. McIntosh, *Curr. Opin. Struct. Biol.*, 2000, **10**, 481–485.

232. S. Tristram-Nagle, H. I. Petrache, R. M. Suter and J. F. Nagle, *Biophys. J.*, 1998, **74**, 1421–1427.

233. K. Gawrisch, D. Ruston, J. Zimmerberg, V. A. Parsegian, R. P. Rand and N. L. Fuller, *Biophys. J.*, 1992, **61**, 1213–1223.

234. N. J. Gibson and M. F. Brown, *Biochemistry*, 1993, **32**, 2438-2454.

235. A. A. Lamola, T. Yamane and A. Zipp, *Biochemistry*, 1974, **13**, 738-745.

236. J. J. Kinnun, K. J. Mallikarjunaiah, H. I. Petrache and M. F. Brown, *Biochim. Biophys. Acta*, 2015, **1848**, 246–259.

237. M. Heyden, J. A. Freites, M. B. Ulmschneider, S. H. White and D. J. Tobias, *Soft Matter*, 2012, **8**, 7742-7752.

238. I. D. Skanes, J. Steward, K. M. W. Keough and M. R. Morrow, *Phys. Rev. E.*, 2006, **74**, 051913.

239. T. Huber, A. V. Botelho and M. F. Brown, *Biophys. J.*, 2002, **82**, 27a.

240. F. M. Richards, *J. Mol. Biol.*, 1974, **82**, 1-14.

241. S. H. White, *Nature (London)*, 1976, **262**, 421-422.

242. J. McCoy and W. L. Hubbell, *Proc. Natl. Acad. Sci. U.S.A.*, 2011, **108**, 1331-1336.

243. R. P. Feynman, R. B. Leighton and M. Sands, *Lectures on Physics*, Addison-Wesley, 1963.

244. G. N. Greaves, A. L. Greer, R. S. Lakes and T. Rouxel, *Nat. Mater.*, 2011, **10**, 823-837.

245. G. N. Lewis and M. Randall, *Thermodynamics*, McGraw Hill, New York, Second edn., 1961.

246. R. Podgornik and V. A. Parsegian, *Biophys. J.*, 1997, **72**, 942–952.

247. J. F. Nagle and J. Katsaras, *Phys. Rev. E*, 1999, **59**, 7018–7024.

248. J. A. Cohen, R. Podgornik, P. L. Hansen and V. A. Parsegian, *J. Phys. Chem. B*, 2009, **113**, 3709–3714.

249. J. des Cloizeaux, *J. Phys. (Paris)*, 1975, **36**, 281-291.

250. P. G. de Gennes, *Scaling Concepts in Polymer Physics*, Cornell University Press, London, 1979.

251. S. Leikin, V. A. Parsegian, D. C. Rau and R. P. Rand, *Annu. Rev. Phys. Chem.*, 1993, **44**, 369-395.

252. D. Harries and J. Rosgen, in *Biophysical Tools for Biologists: Vol 1 in Vitro Techniques*, eds. J. J. Correia and H. W. Detrich, 2008, vol. 84, pp. 679-735.

253. H. M. McConnell and A. Radhakrishnan, *Biochim. Biophys. Acta*, 2003, **1610**, 159-173.

254. L. F. Braganza and D. L. Worcester, *Biochemistry*, 1986, **25**, 2591–2596.

255. J. T. Davies and E. K. Rideal, *Interfacial phenomena*, Academic Press, New York, 1961.

256. B. D. Annin and N. I. Ostrosablin, *J. Appl. Mech. Tech. Phys.*, 2008, **49**, 998-1014.

257. X. Wang and M. Deserno, *J. Chem. Phys.*, 2015, **143**.

258. K. Bertoldi, V. Vitelli, J. Christensen and M. van Hecke, *Nat. Rev. Mater.*, 2017, **2**.

259. L. A. Mihai and A. Goriely, *Proc. Royal Soc. Lond. A*, 2017, **473**.

260. X. L. Yu, J. Zhou, H. Y. Liang, Z. Y. Jiang and L. L. Wu, *Prog. Mater. Sci.*, 2018, **94**, 114-173.

261. D. Needham and E. Evans, *Biochemistry*, 1988, **27**, 8261-8269.

262. G. V. Martinez, E. M. Dykstra, S. Lope-Piedrafita, C. Job and M. F. Brown, *Phys. Rev. E*, 2002, **66**, 050902.

263. M. D. Sefcik, J. Schaefer, E. O. Stejskal, R. A. McKay, J. F. Ellena, S. W. Dodd and M. F. Brown, *Biochem. Biophys. Res. Commun.*, 1983, **114**, 1048-1055.

264. K. Hristova and S. H. White, *Biophys. J.*, 1998, **74**, 2419-2433.

265. W. Blokzijl and J. B. F. N. Engberts, *Angew.Chem.*, 1993, **105**, 1610-1648.

266. D. F. Evans and H. Wennerström, *The Colloidal Domain: Where Physics, Chemistry, Biology, and Technology Meet*, Wiley-VCH, New York, 2nd edn., 1999.

267. J. N. Israelachvili, *Interactions of Biological Membranes and Structures*, Elsevier, 2011.

268. M. F. Brown, R. L. Thurmond, S. W. Dodd, D. Otten and K. Beyer *Phys. Rev. E*, 2001, **64**, 010901-010904.

269. R. Kwok and E. Evans, *Biophys. J.*, 1981, **35**, 637-652.

270. E. Lindahl and O. Edholm, *J. Chem. Phys.*, 2001, **115**, 4938-4950.

271. J. G. Jeon and G. A. Voth, *Biophys. J.*, 2005, **88**, 1104-1119.

272. W. Helfrich, *Z. Naturforsch. A*, 1978, **33a**, 305-315.

273. W. Helfrich, *Eur. Phys. J. B*, 1998, **1**, 481-489.

274. J. N. Israelachvili and H. Wennerström, *J. Phys. Chem.*, 1992, **96**, 520-531.

275. D. Sornette and N. Ostrowsky, in *Micelles, Membranes, Microemulsions, and Monolayers*, eds. W. M. Gelbart, A. Ben-Shaul and D. Roux, Springer-Verlag, New York, Berlin, Heidelberg, 1994, pp. 251-346.

276. M. F. Brown and J. Seelig, *Nature (London)*, 1977, **269**, 721–723.

277. J. Israelachvili and H. Wennerström, *Nature (London)*, 1996, **379**, 219-225.

278. H. Binder, U. Dietrich, M. Schalke and H. Pfeiffer, *Langmuir*, 1999, **15**, 4857-4866.

279. I. Dierking, M. Mitov and M. A. Osipov, *Soft Matter*, 2015, **11**, 819-837.

280. P. G. de Gennes, *The Physics of Liquid Crystals*, Oxford University Press, London, 1974.

281. G. H. Brown and J. J. Wolken, *Liquid crystals and biological structures*, Academic Press, New York, 1979.

282. G. Lindblom and L. Rilfors, *Adv. Colloid Interface Sci.*, 1992, **41**, 101-125.

283. R. Winter, J. Erbes, R. H. Templer, J. M. Seddon, A. Syrykh, N. A. Warrender and G. Rapp, *Phys. Chem. Chem. Phys.*, 1999, **1**, 887-893.

284. L. Picas, F. Rico and S. Scheuring, *Biophys. J.*, 2012, **102**, L1–L3.

285. N. F. Morales-Penningston, J. Wu, E. R. Farkas, S. L. Goh, T. M. Konyakhina, J. Y. Zheng, W. W. Webb and G. W. Feigenson, *Biochim. Biophys. Acta*, 2010, **1798**, 1324-1332.

286. M. Winterhalter and W. Helfrich, *J. Phys. Chem.*, 1992, **96**, 327-330.

287. T. J. McIntosh and S. A. Simon, *Langmuir*, 1996, **12**, 1622-1630.

288. J. N. Israelachvili, *Intermolecular and Surface Forces*, Elsevier, 1992.

289. R. S. Cantor, *J. Phys. Chem. B*, 1997, **101**, 1723-1725.

290. D. Marsh, *Biophys. J.*, 1996, **70**, 2248-2255.

291. R. S. Cantor, *Chem. Phys. Lipids*, 1999, **101**, 45-56.

292. D. Marsh, *Biochim. Biophys. Acta.*, 1991, **1062**, 1-6.

293. D. F. Evans and B. W. Ninham, *J. Phys. Chem.*, 1986, **90**, 226-234.

294. H. T. McMahon and J. L. Gallop, *Nature (London)*, 2005, **438**, 590-596.

295. F. L. H. Brown, *Q. Rev. Biophys.*, 2011, **44**, 391-432.

296. M. Simunovic and G. A. Voth, *Nat. Commun.*, 2015, **6**, 7219.

297. D. C. Mitchell and B. J. Litman, *J. Biol. Chem.*, 2000, **275**, 5355–5360.

298. D. C. Mitchell and B. J. Litman, *Biochemistry*, 1999, **38**, 7617-7623.

299. B. Halle and P.-O. Quist, *J. Phys. II*, 1994, **4**, 1823-1842.

300. A. Grossfield, S. E. Feller and M. C. Pitman, *Proteins: Struct., Funct., Bioinf.*, 2007, **67**, 31-40.

301. J. B. Klauda, R. M. Venable, J. A. Freites, J. W. O'Connor, D. J. Tobias, C. Mondragon-Ramirez, I. Vorobyov, A. D. MacKerell and R. W. Pastor, *J. Phys. Chem. B*, 2010, **114**, 7830-7843.

302. K. A. Henzler-Wildman, G. V. Martinez, M. F. Brown and A. Ramamoorthy, *Biochemistry*, 2004, **43**, 8459-8469.

303. E. Perozo, A. Kloda, D. M. Cortes and B. Martinac, *Nat. Struct. Biol.*, 2002, **9**, 696-703.

304. K. Jacobson, O. G. Mouritsen and R. G. W. Anderson, *Nature Cell Biol.*, 2007, **9**, 7–14.

305. O. S. Andersen and R. E. Koeppe, II, *Annu. Rev. Biophys. Bioeng.*, 2007, **36**, 107–130.

306. R. R. Ketchem, W. Hu and T. A. Cross, *Science*, 1993, **261**, 1457-1460.

307. T. A. Cross and S. J. Opella, *J. Mol. Biol.*, 1985, **182**, 367-381.

308. M. Hong, Y. Zhang and F. Hu, *Annu. Rev. Phys. Chem.*, 2012, **63**, 1–24.

309. M. J. Bogusky, R. A. Schiksnis, G. C. Leo and S. J. Opella, *J. Magn. Reson.*, 1987, **72**, 186-190.

310. S. J. Singer and G. L. Nicolson, *Science*, 1972, **175**, 720-731.

311. R. Q. Fu and T. A. Cross, *Annu. Rev. Biophys. Biomol. Struct.*, 1999, **28**, 235-268.

312. S. D. Cady, K. Schmidt-Rohr, J. Wang, C. S. Soto, W. F. DeGrado and M. Hong, *Nature*, 2010, **463**, 689-692.

313. A. K. Kenworthy, B. J. Nichols, C. L. Remmert, G. M. Hendrix, M. Kumar, ., J. Zimmerberg and J. Lippincott-Schwartz, *J. Cell Biol.*, 2004, **165**, 735-746.

314. V. Kiessling, J. M. Crane and L. K. Tamm, *Biophys. J.*, 2006, **91**, 3313-3326.

315. K. Simons and M. J. Gerl, *Nat. Rev. Mol. Cell Biol.*, 2010, **11**, 688-699.

316. R. W. Pastor, R. M. Venable and S. E. Feller, *Acc. Chem. Res.*, 2002, **35**, 438–446.

317. M. Ø. Jensen and O. G. Mouritsen, *Biochim. Biophys. Acta*, 2004, **1666**, 205-226.

318. C. N. Chin, J. N. Sachs and D. M. Engelman, *Febs Letters*, 2005, **579**, 3855-3858.

319. T. Moriguchi, J. Loewke, M. Garrison, J. N. Catalan and N. Salem, *J. Lipid Res.*, 2001, **42**, 419-427.

320. M. F. Brown and N. J. Gibson, in *Essential Fatty Acids and Eicosanoids*, eds. A. Sinclair and R. Gibson, American Oil Chemists' Society Press, Champaign, 1992, pp. 134-138.

321. A. V. Botelho, N. J. Gibson, R. L. Thurmond, Y. Wang and M. F. Brown, *Biochemistry*, 2002, **41**, 6354-6368.

322. O. Soubias, W. E. Teague and K. Gawrisch, *J. Biol. Chem.*, 2006, **281**, 33233-33241.

323. S. Jaud, D. J. Tobias, J. J. Falke and S. H. White, *Biophys. J.*, 2007, **92**, 517–524.

324. C. Tanford, *The hydrophobic effect, 2nd Edition*, John Wiley and Sons, New York, 2nd edn., 1980.

325. M. F. Brown, *Curr. Top. Membr.*, 1997, **44**, 285-356.

326. K. Tu, D. J. Tobias and M. L. Klein, *Biophys. J.*, 1995, **69**, 2558-2562.

327. S. E. Feller, R. M. Venable and R. W. Pastor, *Langmuir*, 1997, **13**, 6555-6561.

328. A. V. Botelho, T. Huber and M. F. Brown, *Biophys. J.*, 2002, **82**, 515a.

329. J. Israelachvili and R. Pashley, *Nature*, 1982, **300**, 341-342.

330. B. Lindman, T. Tiberg, L. Piculell, U. Olsson, P. Alexandridis and H. Wennerström, in *Micelles, microemulsions, and monolayers: science and technology*, ed. D. O. Shah, Marcel Dekker, New York, 1998.

331. Y. Agzenai, B. Lindman, V. Alfredsson, D. Topgaard, C. S. Renamayor and I. E. Pacios, *J. Phys. Chem. B*, 2014, **118**, 1159-1167.

332. M. Baglioni, C. Montis, F. Brandi, T. Guaragnone, I. Meazzini, P. Baglioni and D. Berti, *Phys. Chem. Chem. Phys.*, 2017, **19**, 23723-23732.

333. F. T. Doole, A. Singharoy, M. F. Brown and M. Kim, *Biophys .J.*, 2019, **abstract**.

334. F. B. Bombelli, D. Berti, F. Pini, U. Keiderling and P. Baglioni, *J. Phys. Chem. B*, 2004, **108**, 16427-16434.

335. R. D. Usery, T. A. Enoki, S. P. Wickramasinghe, V. P. Nguyen, D. G. Ackerman, D. V. Greathouse, R. E. Koeppe, F. N. Barrera and G. W. Feigenson, *Biophys. J.*, 2018, **114**, 2152-2164.

336. B. Eicher, D. Marquardt, F. A. Heberle, I. Letofsky-Papst, G. N. Rechberger, M. S. Appavou, J. Katsaras and G. Pabst, *Biophys. J.*, 2018, **114**, 146-157.

337. T. Huber, K. Rajamoorthi, V. F. Kurze, K. Beyer and M. F. Brown, *J. Am. Chem. Soc.*, 2002, **124**, 298-309.

338. H. I. Ingolfsson, C. Arnarez, X. Periole and S. J. Marrink, *J. Cell Sci.*, 2016, **129**, 257-268.

339. Y. Guo, L. Yang, K. Haught and S. Scarlata, *J. Biol. Chem.*, 2015, **290**, 16698-16707.

340. T. Bartels, L. S. Ahlstrom, A. Leftin, F. Kamp, C. Haass, M. F. Brown and K. Beyer, *Biophys. J.*, 2010, **99**, 2116-2124.